Quantum chemical studies on selected topics of photocatalytic reactions using TD-CC2 linear response and the QM/MM scheme

Dissertation

zur Erlangung des Doktorgrades der Naturwissenschaften (Dr. rer. nat.)
der Fakultät für Chemie und Pharmazie
der Universität Regensburg

vorgelegt von

Thomas Merz

aus Neumarkt i.d.Opf.

im Jahr 2014

Promotionsgesuch eingereicht am:	24. Januar 2014
Tag des Kolloquiums:	7. März 2014
Diese Arbeit wurde angeleitet von:	Prof. Dr. Martin Schütz

Promotionsausschuss	
Vorsitzender:	Prof. Dr. Georg Schmeer
Erstgutachter:	Prof. Dr. Martin Schütz
Zweitgutachter:	Prof. Dr. Bernhard Dick
Drittprüfer:	Prof. Dr. Burkhard König

Teile dieser Arbeit sind bereits veröffentlicht worden:

Kapitel 1

T. Merz and M. Schütz (2013):

"Description of excited states in photocatalysis with theoretical methods" in: **B. König** (Ed.):*Chemical Photocatalysis*. Berlin, Boston: De Gruyter. p. 263 *et seqq.*

Kapitel 2

T. Merz, K. Sadeghian and M. Schütz

"Why BLUF photoreceptors with roseoflavin cofactor loose their biological functionality"

Physical Chemistry Chemical Physics, **13**, 14775 (2011), doi: 10.1039/C1CP21386E

Kapitel 3

T. Merz, M. Wenninger, M. Weinberger, E. Riedle, H.-A. Wagenknecht and M. Schütz

"Conformational control of benzophenone-sensitized charge transfer in dinucleotides"

Physical Chemistry Chemical Physics, **15**, 18607 (2013), doi: 10.1039/C3CP52344F

Danksagung

An dieser Stelle möchte ich mich bei all den Personen bedanken, die zum Gelingen dieser Dissertation beigetragen haben.

Herrn Prof. Dr. Martin Schütz danke ich herzlich für die interessante Themenstellung, Betreuung und die Möglichkeit im Rahmen des Graduiertenkollegs GRK 1626 meine Arbeit anzufertigen und für die finanzielle Unterstützung während dieser Dissertation.

Herrn Prof. Dr. Bernhard Dick für die freundliche Übernahme der Zweitbegutachtung.

Katrin Magerl als Studentensprecherin des GRK 1626 stellvertretend für alle, die in diesem Rahmen durch Diskussionsbereitschaft und Hilfestellung bei der Durchführung dieser Arbeit beteiligt waren. In diesem Zusammenhang möchte ich mich auch bei Herrn Prof. Dr. Hans-Achim Wagenknecht, Herrn Prof. Dr. Eberhard Riedle und Herrn Prof. Dr. Oliver Reiser bedanken, die eine Kooperation mit interessanten Projekten im Rahmen der chemischen Photokatalyse erst ermöglicht haben. Besonders danke ich auch dem Sprecher des Graduiertenkollegs, Herrn Prof. Dr. Burkhard König, für das stete Vertrauen.

Bei allen weiteren Angehörigen des Arbeitskreises möchte ich mich für das angenehme Arbeitsklima und die Hilfsbereitschaft bedanken: Katrin Ledermüller, David David, Matthias Hinreiner, Stefan Loibl, Oliver Masur, Gero Wälz, Dr. Denis Usvyat, Klaus Ziereis und ehemals Dr. Keyarash Sadeghian.

Außerdem bedanke ich mich bei all meinen Freunden, meiner Mutter und im Speziellen bei meiner Frau Caro, gerade auch in schwierigen Situationen, für die Unterstützung außerhalb der Universität.

Contents

1 Introduction

Using the sun for photochemistry is fascinating chemists for quite some time. The first experiment relating to a photo-chemical reaction scientifically described goes back to the year 1834.[1] Hermann Trommsdorff noticed, that crystals of the compound α-santonin, when exposed to sunlight, turned yellow and burst. This was the starting point of numerous discoveries in the field of photochemistry. In the year 1912 in a general lecture before the International Congress of Applied Chemistry in New York, doubtless the prime father of photochemistry, Giacomo Ciamican said the following: "In the desert regions [...] photochemistry will artificially put their solar energy to practical uses".[2]

This dream of a visionary is close to become true. Of course not in a chemical way but at least in using the sunlight for the production of electricity in the arid regions of the world by commercial available photovoltaic cells. Unfortunately, in order to use the energy of the sunlight as a driving force for chemical reaction had not that impact until now.

Doubtless there are a lot of advantages of photochemistry: selective activation of reactants, specific reactivity of the excited molecules, low thermal load on the reaction system and an exact control of the radiation. Combining these pros with catalysis, to come to photocatalysis, the headword sustainability is not far away. Possible closed reaction cycles using the power of the sun, as above mentioned, would certainly improve the concepts and the production of chemicals also in industry and change some production processes to greener chemistry. Therefore the general understanding of mechanistic and prediction of them becomes doubtless very important.

Application of theoretical chemistry to this issue is quite nearby. The theoretical

treatment of molecules in their electronic ground state near the equilibrium geometry is nowadays rather straightforward. Efficient and reliable methods are at hand to calculate energies and their derivatives *w.r.* to various external perturbations, including analytical gradients *w.r.* to displacements of the nuclear positions and are as usually used in geometry optimisations. The theoretical treatment of molecules in electronically excited states, however, is much more complicated and remains a challenge. In contrast to the ground state, electronically excited states can hardly be treated by a single determinant or configuration state function, not even near the equilibrium geometry. This calls for multi-reference methods, or, alternatively, for time-dependent response methods, such as time dependent density functional theory (TD-DFT), or time dependent coupled cluster response theory (TD-CC). This makes almost every carefully attempted theoretical study complicated and time consuming. But in the combination with spectroscopic measurements, it makes it a powerful tool for the investigation of the general theme.

Photochemical reactions occur naturally on potential energy surfaces (PES) related to excited states: after absorbing one or more photons the wave packet representing the ground state probability distribution of the nuclei, is energetically lifted onto an excited state surface. The ground state (GS, S_0) equilibrium geometry (Frank Condon point, FC-point) of course no longer corresponds to a minimum on the excited state surface. The wave packet, therefore, propagates on the excited state surface. On its way it may e.g. cross conical intersection seams (CI).

In Fig. 1.1 a one dimensional PES for a photochemical process is shown. Adiabatic and non-adiabatic processes are included in this picture. Without the direct knowledge of all the processes that are involved in a photochemical reaction, the topologies of the GS and the electronically excited states surfaces give already a lot of qualitative information about the photophysics of the investigated photosystem. Regions of interest are minimum energies and its associated geometries, transition states and conical intersections. As mentioned above, theoretical electronic structure methods and experimental techniques complement each other. This is particularly true for ab initio methods, which are entirely independent

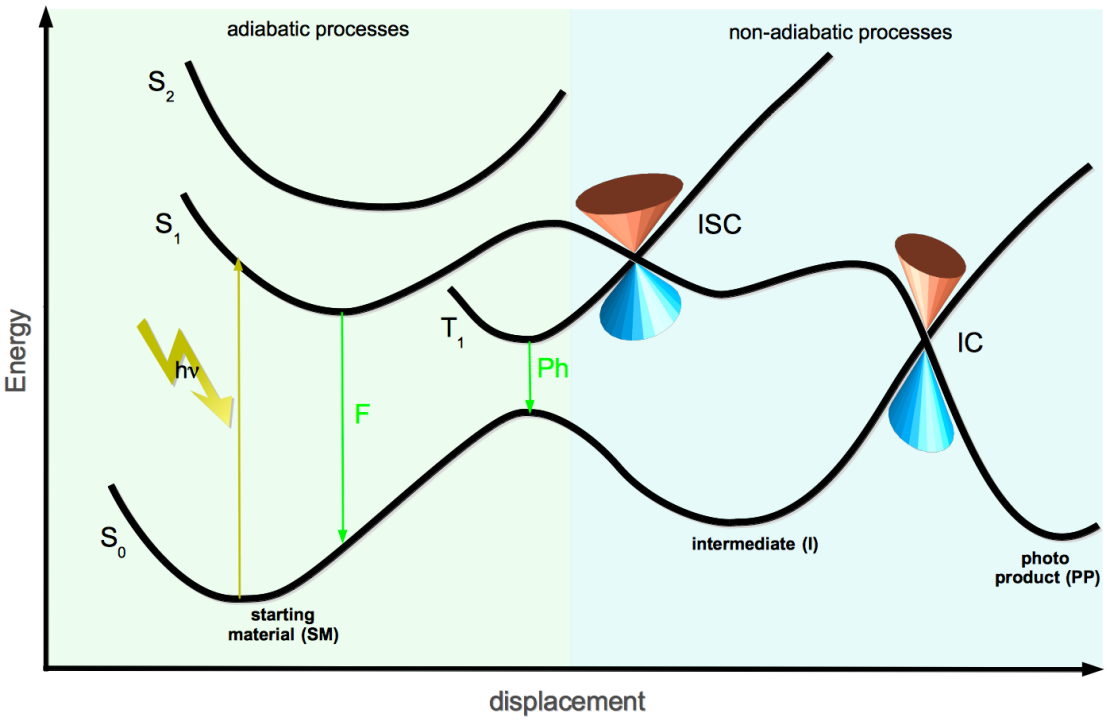

Figure 1.1: One dimensional PES for a possible photochemical processes. The green shaded area shows adiabatic processes and photophysics. **F** corresponds to fluorescence, **Ph** to phosphorescence. The blue shaded area summarises all non-adiabatic processes. The inter-system crossing (ISC) as well as the internal conversion (IC) occur in this example via a conical intersection (depicted by the typical double inverse cone shape, if plotted in a three dimensional PES).

from experimental input in contrast to empirical or semi empirical methods.

The introduction[a] of this work will therefore firstly focus on a short overview about the concept of potential energy surfaces (PES) and the theoretical methods on ab inito side used in this thesis as well as the combination of them with the molecular mechanic scheme (see Section 1.1). Afterwards, the general procedure for the investigation of the studied photocatalytical processes adopted in this work will be presented (see Section 1.2).

[a]This content was already published conceptually as book chapter in [3, Chapter 14, p. 263 *et seqq.*]. Parts of the text are identical to this chapter.

1.1 Excited states and computational methods

The understanding of photochemical reactions can be improved by using modern methods of computational or theoretical chemistry. Starting point for these methods is the Schrödinger equation. One has to introduce approximations to solve the Schrödinger equation with more than one particle. The very first approximation for this problem is the so called Born-Oppenheimer approximation[4] or adiabatic approximation. It allows the splitting of the molecular wave function into its nuclear and electronic components due to the relative mass of the nucleus against the electron. Out of this approximation the concept of potential energy surfaces is derived. It describes the nuclear motion determined by the motions of electrons. The understanding of the topology of the surfaces maps directly to properties of (photo-)chemical reactions. For the electronic part of the Schrödinger equation more approximations have to be introduced due to the electron-electron interaction and the high dimensionality. Here different approximations and methods can be used and are the starting point for the research field of quantum or theoretical chemistry. Since that in this thesis a lot of these principles have been used for the interpretation of the gained results, it is useful to highlight the above mentioned facts in a more extensive way. Of course, the subsections about potential energy surfaces and the computational methods make no claim to be complete. It is not the purpose of this part to give a detailed insight into these methods. Therefore the reader will find literature highlighting the topics much more detailed in the subsections.

1.1.1 Potential energy surfaces

The concept of potential energy surfaces (PES) directly results of the Born Oppenheimer approximation.[4] Because preparative chemists are reluctant to deal with complicated mathematical or physical equations, they use a much simpler argument or model to describe this general principle. It is called reaction coordinate diagram, which shows the energy changes taking place during some mechanism. The reactants are converted into the products by passing the reaction path through

a maximum energy state, the so called transition state. This diagram converts the potential energy surface of the molecules participating in the reactions into e.g. a one dimensional plot (see also Fig. 1.1). In principle, this is already a 1-dim PES. It describes the energy of the corresponding state of molecules as a function of the positions of the nuclei. Of course, the complete surface is 3N-6 dimensional (3N-5, if the molecule is linear), where N is the number of nuclei. As already mentioned, the topology of the PES directly maps onto chemical properties of the whole system. Minima represent stable structures and first order saddle points correspond to transition states. The connection of the potential energy surfaces and a reaction coordinate diagram is shown in Fig. 1.2.

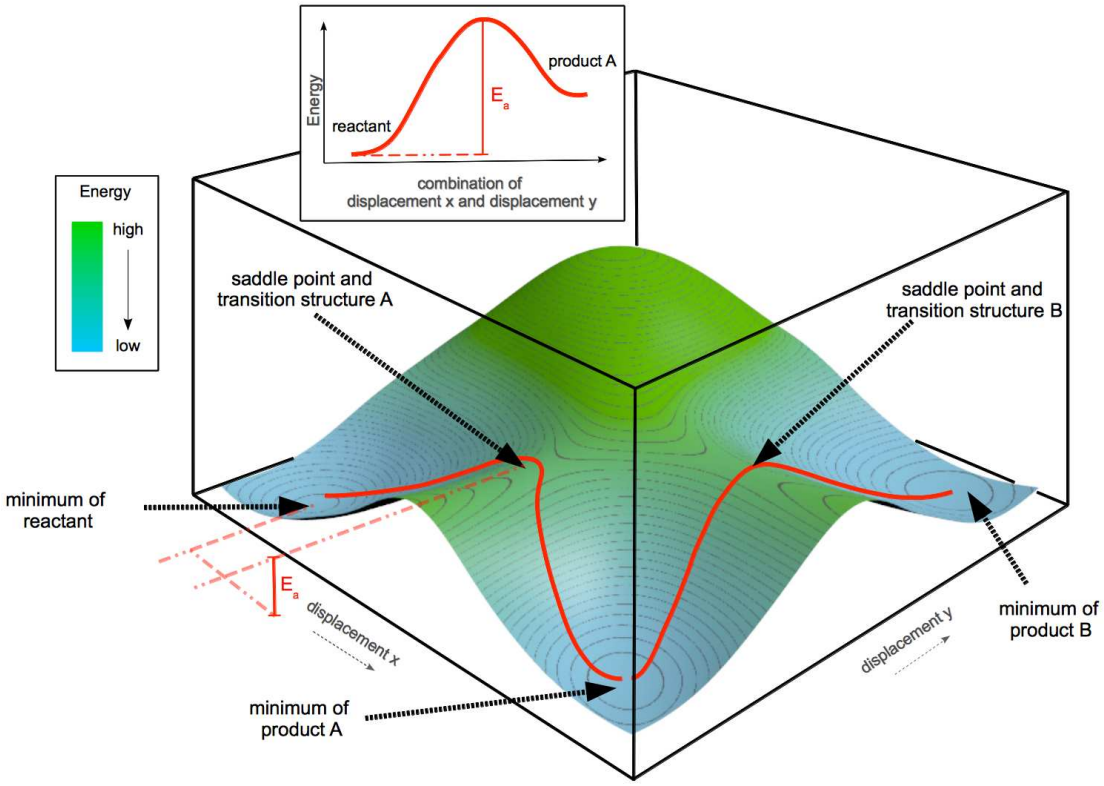

Figure 1.2: Two dimensional (2-dim) PES with two reaction pathways starting from the reactant to product B passing product A. Additional the reaction coordinate diagram for the reaction to Product A is given. In both cases, E_a corresponds to the reaction energy.

In this figure, one global minimum, which represents the reactant of the given

system, and two local minima, representing products A and B, are shown. The reaction paths, depicted as red lines, connecting these minima via the two saddle corresponding to transition states.

Of course this concept can also be applied for excited molecules. In this case one would have two surfaces, one for the ground state and one for the excited state, the latter lying above the GS PES. For the adiabatic regime, which means that the two PES are sufficiently separated, the Born Oppenheimer approximation works fine. Unfortunately, non-adiabatic coupling elements are neglected by this approximation. At points where two PES intersect, the energies of the two states are degenerate. At these points, small displacements in the nuclear coordinates change the character of the wave functions of the two states fundamentally. Consequently, the two related wave functions describing a molecule at a conical intersection are arbitrary mixtures of the wave functions of the separated pure states. The non-adiabatic coupling elements thus become large and the Born Oppenheimer approximation breaks down. At these very interesting points, the motion of the electrons and nuclei is coupled. Therefore the system can cross the two PES very easy, efficient and fast which can be used in several ways. One prominent example is the photostability of the DNA. Conical intersections between electronically excited states and the GS are used by nature to rapidly shed energy and to avoid photochemical reactions in photo-excited nucleobases.[5] Conical intersections, postulated already in the 1930s,[6,7] have become ubiquitous in photophysics during the past two decades. For a non-linear three-atom molecule like ozone[8] the PES of two states touch in a single point. Due to this topology, it is often illustrated as a double inverse cone.[9] For bigger molecules the space of degeneracy corresponds to a 3N-8 dimensional hypersurface (there are two additional conditions to be fulfilled such that the two by two CI matrix involving the two relevant states yields two degenerate eigenvalues).

The exemplary presented photochemical reaction in Fig. 1.1 shows the main adiabatic and non-adiabatic reactions that are possible after excitation and they are now in the centre of attention. The absorption from the GS (or S_0) to the first singlet state occurs in the time range of femtoseconds. After the relaxation to the

lowest vibrational level, the molecule can get back to the ground state by emitting a photon. This is called fluorescence (**F**), which is happening in nanoseconds range. The emission of a photon out of a triplet state is called phosphorescence (**Ph**). This process takes place in the milliseconds time range. All these are adiabatic processes. On the other hand, processes with no radiation of photons as well as the population of other spin states (e.g. triplet states), which are very important in photochemical reactions, are governed by non-adiabatic processes. Crossings of surfaces can occur between same or different spin symmetries. If the crossing involves states with different spin symmetry one speaks of inter-system crossing (ISC), otherwise of internal conversion (IC). If the IC is based on vibronic coupling, the process is also an adiabatic one. However, both cases decrease the fluorescent quantum yield. Ultra fast conversion, for instance to the photoproduct in Fig. 1.1, is often mediated by a CI between two surfaces.

The exemplary photoreaction from Fig. 1.1 can be reduced schematically to the following very simple overall reaction formula:

$$SM \xrightarrow{h\nu} I + PP\,.$$

In this overall reaction the reactant (SM) is converted to an intermediate (I) and the photoproduct (PP) after excitation. It does not play a role, whether the reaction is based on a monomer or a complex reaction of a lot of starting materials to a desired photoproduct. The reaction coordinate would be the displacement of the system e.g. along some internal coordinate in this example. Due to the knowledge of the shape of the PES (see Fig. 1.1) one can discuss this reaction more detailed. After the excitation of the starting material into the first singlet state one possible relaxation would be the fluorescence back to the GS. But also ISC into the first triplet state could occur to some extent. In this case, the process would be non-adiabatic, mediated by a conical intersection. A deactivation channel back to the starting material or to some intermediate is phosphorescence. The productive channel to the photoproduct would be the IC by a CI from the first singlet state. All these processes can now extent the simple reaction formula from the beginning to a valid "photocycle" and extended formulae, which are shown in Fig. 1.3.

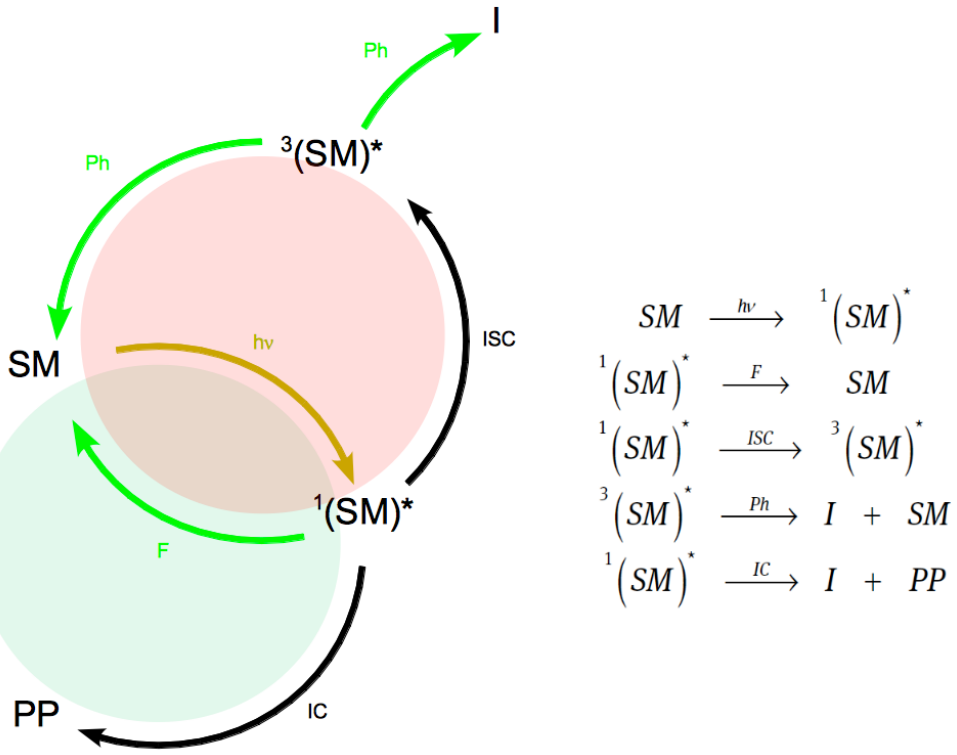

Figure 1.3: Corresponding photocyle to example reaction (see Fig. 1.1) and extended reaction formula. The green cycle is productive, the red one is destructive.

Of course, all reactions still depend on the one hand on the energetic barriers, which have to be passed during the reaction pathway and on the other hand on displacements which are necessary for the forthcoming of the reaction. Nevertheless, the knowledge of the character of the involved PES as well as the conditions for non-adiabatic processes in the photochemical reaction is of benefit for the tuning of reactions towards a desired photoproduct. Quantum chemical methods and theoretical chemistry can be part of the investigation of these problems and help for the description of reasons for unexpected intermediates or failed photoreactions. In the following, two classes of quantum chemical methods often used for such purposes are presented.

1.1.2 Computational methods

The description of electronically excited states with ab initio wave function methods can either be done by using time dependent density functional theory (TD-DFT), or single as well as multi-reference methods. The latter ones are difficult to use in the applications to extended molecular systems and will not be discussed here, as they were not used in the context of this thesis. However, detailed information about these methods can be found in the literature.[7,10] Single reference methods include methods like Configuration Interaction, e. g. the Configuration Interaction Singles CIS[11] method, propagator methods like RPA and ADC,[12,13] and time-dependent coupled cluster response TD-CC methods. TD-DFT and TD-CC both have in common, that they are response methods, which means, that excitation energies are calculated as the poles of the time- or frequency dependent polarizability by first-order perturbation theory (linear response). It is based on a time- or frequency-dependent external perturbation and thus excitation energies can be regarded as a time or frequency dependent ground state property of the studied molecule. In the following, the main focus is on TD-CC and TD-DFT, because these methods are inexpensive enough to describe issues in photocatalysis and were used extensively in this thesis. Additional to that, special attention will be given to potential pitfalls. For detailed information, the reader is referred to the references given during the next few lines.

Starting with TD-CC, one should begin with the equation for the coupled cluster wave function. It is specified by an exponential excitation operator acting on the Hartree-Fock reference wave function $|0\rangle$:

$$|CC\rangle = \exp(T)|0\rangle \tag{1.1}$$

$$T = \sum_i T_i \tag{1.2}$$

Approximations can be done by truncation of the sum of T (see Equation 1.2) , the cluster operator, e.g. for coupled cluster singles and doubles, where $i = 2$.

The two resulting cluster operators T_1 and T_2 each generate a linear combination of all possible singly and doubly substituted determinants, respectively, from $|0\rangle$. Singly substituted means that a certain molecular orbital occupied in the reference is replaced by a virtual molecular orbital and doubly that two certain molecular orbitals are being replaced by two virtual molecular orbitals, respectively. As one can see from Equation 1.1 there is an exponential ansatz for the wave function. Due to this fact, the wave function is always (at each truncation level) product separable and the energies are thus size extensive. Furthermore, all possible excitations of full configuration interaction are generated, even when the cluster operator is restricted to only singles and doubles as above. The coefficients of higher excitation levels, like quadruples, then factorise as products involving singles and doubles coefficients.

So far, the method is highly accurate to describe ground states and provides a large fraction of the correlation energy.[14] To describe excited states within the couple cluster framework commonly applied methods are the equation of motion couple cluster (EOM-CC) methods[15] and time dependent coupled cluster (TD-CC) linear response[16,17] based on the hierarchy of the coupled cluster models CC2,[18] CCSD, CC3,[19] and CCSDT. The TD linear response approaches aim at the frequency dependent polarizability of the system by first-order perturbation theory, which means that the excitation energies are calculated as the poles, and the transition strengths as the residues of this time-dependent ground state property, as mentioned above. TD-CC2 response is the cheapest method including dynamic correlation effects in the given hierarchy. The reason for the inexpensive character of this method is that similar to second order Møller–Plesset perturbation theory (MP2) doubles substitutions are just treated to first order *w.r.* to the fluctuation potential. Despite of this simplification, TD-CC2 is quite a robust method and provides a qualitatively correct picture of excited states with an accuracy of about 0.2–0.3 eV in the excitation energies compared to experimental values. But, this accuracy is limited to excited states that are dominated by singles substitutions, which is usually the case for low energy excitations as those considered here. In the vicinity of CI, the excitation energies may become complex, though there are correction schemes to cope with that problem.[20] However, any response

theory has this drawback and breaks down for conical intersections with the ground state, since at this point the ground state reference no longer is properly described by a configuration state function. On the other hand, the most important drawback of TD-CC response is the restriction to rather small molecules, especially for the description of electronically excited states. This is also true for the comparatively cheap TD-CC2 response method, particularly so for energy gradients *w.r.* to nuclear displacements, as needed for geometry optimisations on excited state surfaces. A practical approach, which was also applied in this thesis, is to utilise the cheap TD-DFT methods for geometry optimisations and TD-CC2 for excitation energies and other properties at these TD-DFT geometries.

This leads to Kohn–Sham density functional theory (DFT), which is one of the most frequently used theoretical approaches in almost every field of chemistry. According to the Hohenberg–Kohn theorem[21] there exists a functional $E[\rho(\mathrm{r})]$ mapping the exact electron density to the exact energy. That means, the energy can in principle be calculated using a much simpler object than a wave function, the so called (one-particle) density function $\rho(\mathrm{r})$, which depends only on three degrees of freedom. Unfortunately, nobody knows what this functional actually looks like, because the Hohenberg–Kohn theorem just proves the existence of it. The unknown part of $E[\rho(\mathrm{r})]$ can be condensed in the exchange correlation part $E_{xc}[\rho(\mathrm{r})]$. This part has to be modelled, which is why present DFT functionals are semi-empiric approaches. This approximation led to a plethora of different $E_{xc}[\rho(\mathrm{r})]$. They range from simple local density approximations (LDAs), over gradient corrected functionals (GGAs), hybrid functionals like the famous B3LYP,[22] to range-separated hybrids, orbital dependent functionals, and random-phase approximations for correlation. To describe electronically excited states, a linear response theory on the basis of DFT is mostly used in TD-DFT.[23] The famous Casida's equations are very similar to those of time-dependent Hartree–Fock theory and as for TD-CC response, the excitation energies correspond to the poles of the frequency dependent polarizability. The TD-DFT methods are very efficient methods for excited states, especially for extended systems. In comparison to ab initio wave function methods, the analytical gradients and thus geometry

optimisations are very inexpensive. This general simplicity in the usage and the availability in most ab initio electronic structure program packages, are probably the keys to its enormous success. On the other hand, both DFT and TD-DFT lack the possibility of a systematic improvement of the method, since there is no such hierarchy of methods as for ab initio wave function methods. Another drawback of the method are artifacts plaguing DFT, like a non-vanishing correlation energy of a single electron or the self-repulsion of electrons. The latter has severe consequences for TD-DFT. The excitation energies of charge transfer (CT) excited states are grossly underestimated[24–26] due to the absence of the excitonic hole-particle attraction in local or semi-local functionals.[27] Large separation of hole and particle in the excitation energies of CT excited states lead to an underestimation of the energies by several eV. Additionally, these states also mix eventually with other low-lying valence states and contaminate them. To some extent, hybrid functionals with a large fraction of non-local exchange or range-separated hybrids[28–30] shift CT states back to higher energies. Even the TD-DFT response method is unable to deal with conical intersections, just like the TD-CC methods. These drawbacks have to be in mind, when applying TD-DFT, foremost if low-lying CT states appear. Often those states are absurd and may even contaminate other valence states, which leads to a wrong picture of photophysics of the investigated system. Verification of the TD-DFT calculations with methods like TD-CC2 are crucial to avoid this issue.

1.1.3 QM/MM scheme

Although, TD-CC and TD-DFT methods are inexpensive enough to describe photochemical reactions, addition of solvents or large biologic systems make them inefficient. So, combination of QM-methods with the less expensive molecular mechanic (MM) method is desirable. In the 1970s of the last century, Warshel and Levitt first suggested to combine these two methodologies,[31] which has become famous as the QM/MM hybrid approach. Their trendsetting idea had already all in hand, which is still used nowadays. Field, Bash and Karplus were the first who combined the CHARMM force field, a widely used model potential for MM

calculations, with QM methods.[32] This idea was honoured with the Nobel Prize in chemistry in the year 2013.[33,34] For the QM/MM approach, the whole system ($\mathbb{S}$) is divided in two parts (regions). The first part (QM-region, $\mathbb{I}$) is in almost every case very tiny with respect to the rest and consequently can be treated with accurate and appropriate QM methods. It comprises the part of the system, in which the actual reaction takes place. The second and larger part (MM-region, $\mathbb{O}$) holds the rest of the studied system. In Fig. 1.4 this is shown schematically.

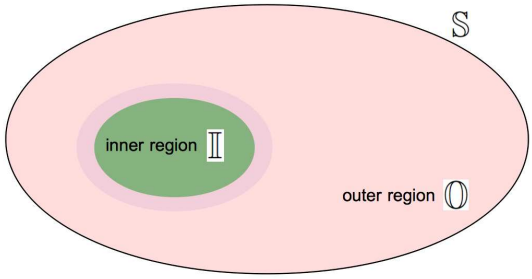

Figure 1.4: Complete system $\mathbb{S}$ divided into outer $\mathbb{O}$ (red) and inner part $\mathbb{I}$ (green); region between $\mathbb{O}$ and $\mathbb{I}$ is depicted in magenta and contains the possible link atoms $\mathbb{L}$.

Due to the fact that only a small part of the complete system is treated with an expensive QM method in contrast to the MM region, it is possible with the QM/MM approach to investigate truly large systems. Inclusion of only the interesting parts in the QM-region, e.g. the enzymatic active region of a protein, or, if the method is utilised for the description of solvation effects, one single solute molecule or alternatively, a cluster of the solute with its first solvation shell, reduces the computation time dramatically relative to a full QM treatment of the whole system, which would be entirely unfeasible. Since solvation severely affects reactions and, especially in photochemical reactions, photophysical properties of molecules, the QM/MM approach is an excellent tool to be employed to describe these effects and taking them into account for the investigations of reaction mechanisms. The MM methods, often simply called force field methods, can be used to mimic the natural environment, which in biological systems is water. There are a lot of different model potentials for water; the most prominent one is the TIP3P model.[35] It is a 3-site water molecule parametrised to reproduce

the behaviour of liquid water. This model has been improved by a lot of other approaches. Organic systems on the other hand are often non-polar and cannot be solved in water and therefore non-polar solvents have to be used for these systems. Yet, for the MM scheme in principle every solvent can be modelled and used in the QM/MM calculations. After this short motivation an overview of the model potentials or force fields, as employed in MM methods, is given. Subsequently, the coupling of the MM and QM methods and the resulting traps related to this coupling are discussed to some extent.

Major application of the MM methods is in the framework of biology. Calculations of the energy of such systems within this approach only depend on its atomic coordinates. The energy and the forces on the atoms are related to the gradient of the potential function. This function sums harmonic contributions originating from bond- and bond-angle-displacements, cosine terms reflecting displacement of dihedral angles (torsions), as well as electrostatics (modelled by partial charges or higher moments), van-der-Waals dispersion and exchange repulsion terms. In Equation 1.3 an example of a simple potential is given.

$$E_{\mathrm{MM}} = E_{\mathrm{bonded}} + E_{\mathrm{unbonded}} \tag{1.3}$$

$$E_{\mathrm{bonded}} = E_{\mathrm{bond}} + E_{\mathrm{angle}} + E_{\mathrm{torsion}} \tag{1.4}$$

$$E_{\mathrm{unbonded}} = E_{\text{van-der-Waals}} + E_{\mathrm{Coulomb}} \tag{1.5}$$

Splitting this up, the bonded energy terms E_{bond} describes the interaction between two atoms and is given by the following equation:

$$E_{\mathrm{bond}} = \sum_{\mathrm{bonds}} k_d (d - d_0)^2 \tag{1.6}$$

It sums up all existing bonds between two atoms, where k_d is the force constant, which describes the type of the bonds (e.g. single or double bond of two carbon atoms) and d_0 is the equilibrium distance.

The angle between three atoms is considered by E_{angle} and given in Equation 1.7. As before, a force constant k_θ and an equilibrium angle θ_0 are part of the energy term.

$$E_{\text{angle}} = \sum_{\text{angles}} k_\theta (\theta - \theta_0)^2 \tag{1.7}$$

In an analogous way, torsions between four atoms are described by

$$E_{\text{torsion}} = \sum_{\text{torsions}} k_\phi [1 + \cos(n\phi + \delta)] \tag{1.8}$$

Non bonding interactions are included by van-der-Waals and Coulomb terms (see Equation (1.9))

$$E_{\text{unbonded}} = \sum_{\substack{\text{unbonded} \\ \text{pairs AB}}} \left\{ \epsilon_{\text{AB}} \left[\left(\frac{\sigma_{\text{AB}}}{r_{\text{AB}}} \right)^{12} - \left(\frac{\sigma_{\text{AB}}}{r_{\text{AB}}} \right)^{6} \right] + \frac{1}{4\pi\epsilon_0} \frac{q_{\text{A}} q_{\text{B}}}{r_{\text{AB}}} \right\} \tag{1.9}$$

For the following discussions the description above should be sufficient and the reader should now have a feeling how this potentials are built. For a detailed review of force fields and all related issues the reader is referred to an excellent review article of Ponder and Case.[36] Outgoing from these equations it is evident that quite a lot of parameters affect such a model potential. They constitute the so called force field and different parametrisation certainly lead to different force fields. The development of the needed parameters is quite complicated and needs a lot of knowledge. This also results in a careful integration of new molecules, not covered so far to a specific force field. The combination with QM methods for the combined QM/MM approach allows for almost every force field to be used. The two established ones are AMBER[37] and CHARMM.[38,39] They can be attached to almost every problem and are optimised for biological systems like enzymes, proteins and DNA. However, it is possible to use them also for other chemical studies. The first mentioned AMBER force field also offers the possibility to parametrise organic molecules within its framework by using the GAFF (general AMBER force field) parameters,[40] which was used in the framework of this thesis.

The GAFF force field parameters are designed for compatibility with the original AMBER force field developed for biological systems. GAFF includes parameters for almost every organic or pharmaceutical molecule composed of hydrogen, carbon, nitrogen, oxygen, sulphur and phosphorus. A common procedure to import molecules is available and described by Bayly *et. al.*[41] Nevertheless, there are also force fields, that were developed especially for small organic molecules and are therefore more versatile because of a higher diversity. Specialised force fields like MMx,[42–44] UFF[45] should be mentioned in this context and are used quite extensively. Gromacs[46] also provides this alternative for the sake of completeness.

As already mentioned at the beginning of this section, the combination of the QM and MM methods leads to the QM/MM hybrid approach. MM methods are used for the surrounding, like solvents or larger parts of proteins, of the region of interest, which is treated by the QM methods. As one can see schematically in Fig. 1.4, the whole system $\mathbb{S}$ is divided into $\mathbb{I}$ (QM-region) and $\mathbb{O}$ (MM-region). Each atom of the system is assigned either to $\mathbb{O}$ or $\mathbb{I}$. The coupling of those two parts is an important step and determines also the accuracy of the QM/MM calculations, besides the method of choice. In principle this can be done in two different coupling schemes, (i) the subtractive (see also Equation (1.10)) and (ii) the additive (see Equation (1.11)) coupling. Both schemes are well developed in the meantime and discussed in detail in a lot of articles and reviews.[47–50]

For the subtractive coupling (i) the energy of the whole system $\mathbb{S}$ is calculated by the force field ($E_{MM}(\mathbb{S})$) at first, followed by separate MM and QM calculations for the energy of the subsystem $\mathbb{I}$ (resulting in $E_{QM}(\mathbb{I}+\mathbb{L})$ and $E_{MM}(\mathbb{I}+\mathbb{L})$. Subtracting $E_{MM}(\mathbb{I}+\mathbb{L})$ from the sum of $E_{MM}(\mathbb{S})$ and $E_{QM}(\mathbb{I}+\mathbb{L})$ leads to the QM/MM energy of the system.

$$E_{QM/MM}(\mathbb{S}) = E_{MM}(\mathbb{S}) + E_{QM}(\mathbb{I}+\mathbb{L}) - E_{MM}(\mathbb{I}+\mathbb{L}) \tag{1.10}$$

Implementation of this scheme is quite simple, but leads to some errors due to the fact that the polarisation of the QM part by the MM part is not taken into account. For the additive scheme (ii) the MM calculation is only performed for

the MM part ($E_{MM}(\mathbb{O})$), followed by a QM calculation for the energy of the inner region ($E_{QM}(\mathbb{I}+\mathbb{L})$). Now a special coupling term ($E_{QM-MM}(\mathbb{I},\mathbb{O})$) is needed to describe the interaction of the two subsystems. Addition of these three energies yields the QM/MM energy of the whole system.

$$E_{QM/MM}(\mathbb{S}) = E_{MM}(\mathbb{O}) + E_{QM}(\mathbb{I}+\mathbb{L}) + E_{QM-MM}(\mathbb{I},\mathbb{O}) \tag{1.11}$$

Before the coupling term $E_{QM-MM}(\mathbb{I},\mathbb{O})$ is briefly discussed, the reader may have recognised the abbreviation $\mathbb{L}$. For the case that $\mathbb{I}$ and $\mathbb{O}$ are not connected to each other via a chemical bond, no further challenges for the QM/MM calculations arise. In most cases, especially if the system comprises of proteins, it is not possible nor appropriate to divide $\mathbb{S}$ into subsystems without artificial bond breaking. That artificial bond break has to be capped with appropriate procedures otherwise homolytically or heterolytically cleaved molecules in the QM or MM region would lead to artificial radicals or charges, which have little relation to the original system. For this problematic issue different solutions were developed. One variant is to introduce additional atoms to the QM region, covalently bound to the last QM atom. This scheme is called the link-atom scheme and is achieved by capping the atoms with hydrogen or fluorine atoms.[51] Another possibility is to add localised orbitals at the boundary, which are kept frozen in the QM calculations.[52] There are further methods to handle this problem, which are not discussed here; the reader is therefore referred to the excellent review of Senn and Thiel about the QM/MM scheme in general.[53] In particular for the link-atom scheme one has to be careful to prevent over-polarisation of the QM density.[54] However, throughout this thesis, the link-atom approach was used with care, knowing its drawback, due to its simplicity.

Coming back to the $E_{QM-MM}(\mathbb{I},\mathbb{O})$ term, once again, different solutions were developed:[55] (i) the mechanical and (ii) the electrostatic embedding should be mentioned here. The mechanical embedding is based on MM-MM electrostatics, while electrostatic embedding implies inclusion of MM charges in the QM calculation: the MM point charges are included in the one-electron Hamiltonian of the QM region as sources of an external electrostatic field. With this procedure the

polarisation of the QM part through the MM part is taken care of.

1.2 General Procedure

After this short elemental introduction, the procedure, which was used for the investigation of photochemical systems and photocatalysis, is presented. One should mention that it is quite difficult to give a general recipe for QM or QM/MM investigations dealing with these tasks. However, the used procedure covers the most important aspects for the description of such investigations, but it is essential to have the discussed pitfalls and drawbacks in mind: it starts with the proper choice of the QM method and ends with the final interpretation of the results. During the study of different systems and aspects in this thesis, in principle two steps must be considered to get reasonable results. These two steps showed to be quite robust. If one is interested in the conical intersection seam, further and not straightforward calculations have to be done. These further procedures are not discussed here and were not part of the investigations made in this thesis. To make this procedure more clearly, the example of a photochemical reaction shown in Fig. 1.1, which is used almost throughout this introduction, was taken to visualise the important aspects. The original reaction is shaded while the actual steps are coloured red. Black depicts already gained information.

1. The starting point of every theoretical investigation of an arbitrary system is the vertical excitation spectrum for the ground state minimum (FC-point). This is only one first jigsaw piece for the complete investigation. At that point the types of all electronically excited states have to be determined. Different methods should be compared and calibrated at that stage, e. g. TD-DFT with different functionals should be compared to TD-CC2 reference calculations. This provides the needed information, which method or functional can be applied for the target system (this is strongly recommended for QM/MM investigations in order to use the affordable TD-DFT methods).

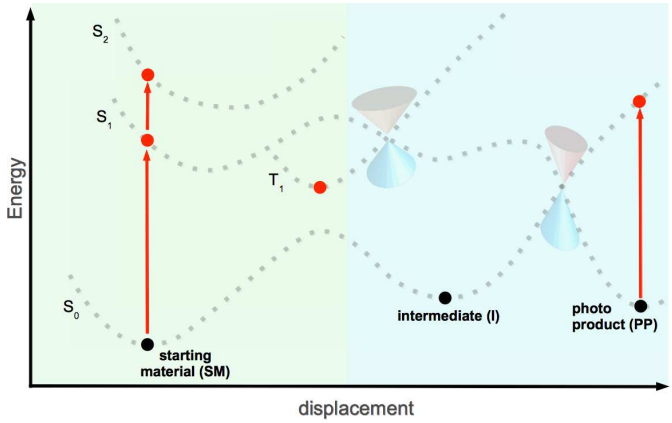

Figure 1.5: Step 1.1: Vertical excitation spectrum for the ground state minimum, assignment of the types of the electronically excited states and validation of methods (not shown schematically).

Next, the relevant low-energy minima on the PES of the excited states have to be determined. With the geometries related to the reactants, intermediates and products of a photochemical reaction at hand, one already has a qualitative picture of the mechanism at work. A practical approach as mentioned before, is to utilise the cheap validated TD-DFT methods for geometry optimisations and TD-CC2 for excitation energies and other properties at these TD-DFT geometries.

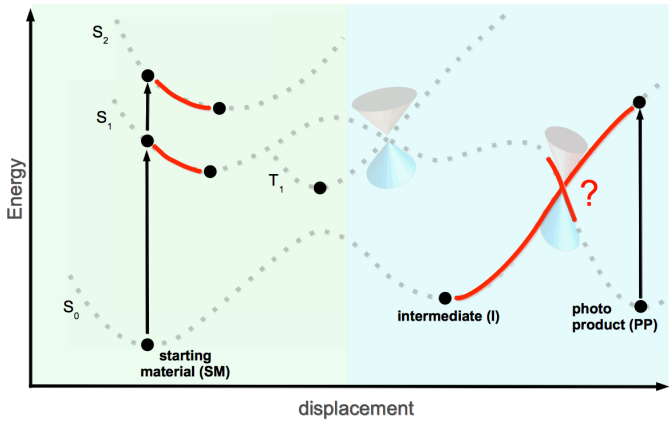

Figure 1.6: Step 1.2: Geometry optimisations of low-energy minima on PES of excited states for SM, I and/or PP.

2. In order to determine the minimum energy path between reactants and products is more intricate: Provided that the reaction coordinate is a priori known, i. e., reflected in one or just a few internal coordinates, geometries along the reaction coordinate can be generated by hand. Otherwise more general and costly approaches must be utilised. For example, the NEB (nudged elastic band) method[56] could be used. For a detailed discussion about optimisation methods to determine minimum energy paths the reader is referred to the literature.[57]

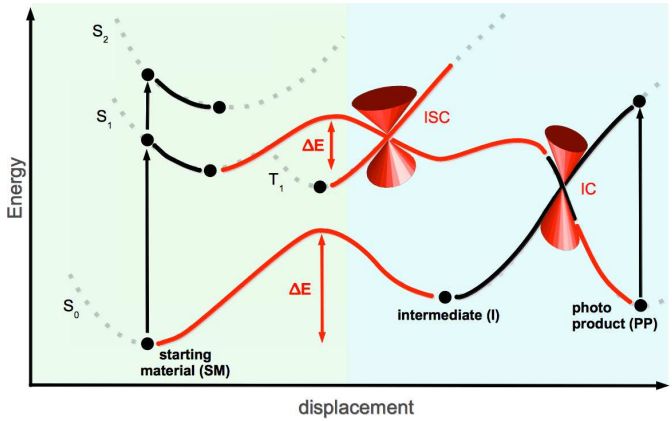

Figure 1.7: Step 2: Determination of minimum energy paths of involved species.

1.3 Outline

After this introduction, three examples for the investigation of photochemical/photocatalytical issues with the above shown scheme are presented. The first one deals with roseoflavin, a photocatalyst, which is suitable to replace the well known flavin as photochromophore in biological systems as well as in chemical photocatalysis. This study shows the general applicability of the used scheme by comparing them to available photophysical investigations (see Chapter 2). The second example deals with two artificial dinucleotides consisting of a nucleoside with benzophenone as chromophore and of one of the two natural nulceosides guanosine and thymidine, respectively. The objective was to investigate a possi-

ble photo-induced intramolecular charge transfer in detail (see Chapter 3). The third and last investigation covers a step in a proposed reaction mechanism of visible light mediated photochemical decarboxylations (see Chapter 4).

In the presented examples, TD-DFT was used for geometry optimisations of electronically excited states in most cases. In order to identify potential problems, like contamination of relevant valence states by low-lying charge transfer states, TD-CC2 single point calculations were always performed to be aware of this pitfall. The two methods were compared with each other by comparing the singles substitution vectors, as well as dipole moments and transition strengths. If the time saving TD-DFT methods were insufficient for the solution of the given systems, the more robust and qualitative correct TD-CC2 method was used.

For some of the presented examples, solvent effects were taken into account by using the described QM/MM scheme. Parametrisation for the molecular force field was done very carefully. Solvated geometries for the QM/MM calculations were generated on the basis of minimum energy structures of isolated solute (optimised by using QM methods) embedded in a large enough solvent shell and by performing MD simulations after an initial equilibration phase. The typical MD trajectories range between 500 *ps* and 10 *ns*, depending on the size of the system. Subsequently, different snap shots representative for the relevant geometries encountered during the MD simulation were chosen as starting points for following QM/MM investigations on the ground and excited state surfaces.

2 Roseoflavin as photocatalyst?

The content of this chapter has been published in Physical Chemistry Chemical Physics.[58] Parts of the text are identical to the publication. Besides some changes in formulations the publication was revised concerning the context given in this thesis, i.e. basic principles, which were discussed in Chapter 1, and the appendix of the publication was integrated into the text to some extent.

2.1 Introduction

To use flavin (see Fig. 2.1) as photocatalyst in organic chemistry is an obvious idea. Riboflavin or vitamin B_2 (see Fig. 2.1, R= ribityl group) is an important biological redox cofactor and is involved in a large number of processes as photoreceptor to perceive light at a strong absorption up to 500 nm. Riboflavin is the central component of the flavin mononucleotide (FMN or riboflavin-5'-phodsphate) or flavin adenine dinucleotide (FAD) used in bacteria, plants and mammals as photoreceptor. If these photoreceptors are incorporated in proteins, they are called BLUF (blue light using FAD)[59] proteins. The first discovered BLUF protein containing such a domain was AppA from Rhodobacter sphaeroides.[60–66]

Since the first discovered BLUF-domain containing flavoprotein several other BLUF signalling domains have been found in prokaryotic and eukaryotic microorganisms.[67] These include BlrB,[68,69] Slr1694[70–74] and Tll0078.[75–77] Most of them have different physiological functions, but share a common feature, namely the change in their UV/Vis-, as well as in their IR-spectra upon signalling state formation. It is therefore widely accepted that different BLUF domains should have

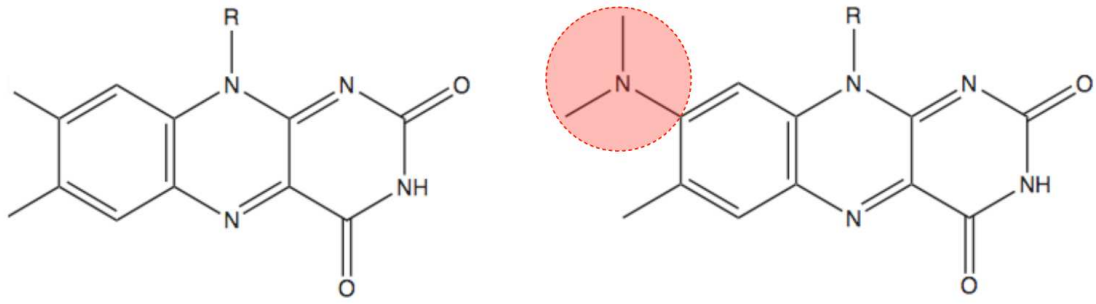

Figure 2.1: Chemical structure of flavin (left side) and roseoflavin (RoF; right side; dimethylamino group (DMA) depicted in red). R depicts possible side chain of molecules.

the same or similar mechanism for the signalling state formation. The lack of unique crystal structures for both the dark- and light-adapted forms of BLUF-domains however has made the search for a conclusive mechanism of signalling state formation a challenge. A lot of proposals for this were made so far. Many different mechanisms were postulated,[78–83] which all have in common the very first step, *i.e.*, an electron transfer process from the nearby tyrosine residue to the flavin chromophore, which explains the observed fluorescence quenching of the latter. Sadeghian *et. al.* presented a plausible mechanism for the formation of the signalling state based on a systematic investigation of the potential energy surface.[84,85] There is strong evidence that after photo-excitation of the locally excited (LE) state of flavin, the tyrosine → flavin charge transfer (CT) state is populated via a conical intersection.

This conical intersection seam has been investigated in detail by Udvarhelyi and Domratcheva.[86] At the level of the complete active space self consistent field (CASSCF) method the authors located the minimum energy point on the seam along the relevant proton transfer reaction coordinate. Moreover, they also calculated pathways for the entire photo reaction leading to the final signalling state structure. The steps of this reaction cascade include tautomerization of the highly conserved glutamine residue and are in principle in agreement with the ones postulated by Sadeghian *et. al.* .

However, as mentioned before, flavin itself can also be used successfully in organic photochemical reactions as photocatalyst for redox reactions. One example for such a photocatalytic reaction is the oxidation of methoxybenzyl alcohol to an aldehyde.[87] In Fig. 2.2 the scheme of the oxidation mechanism is depicted, which was proposed utilising transient absorption spectroscopy among other techniques [3, Chapter 15, p. 295 et seqq.].

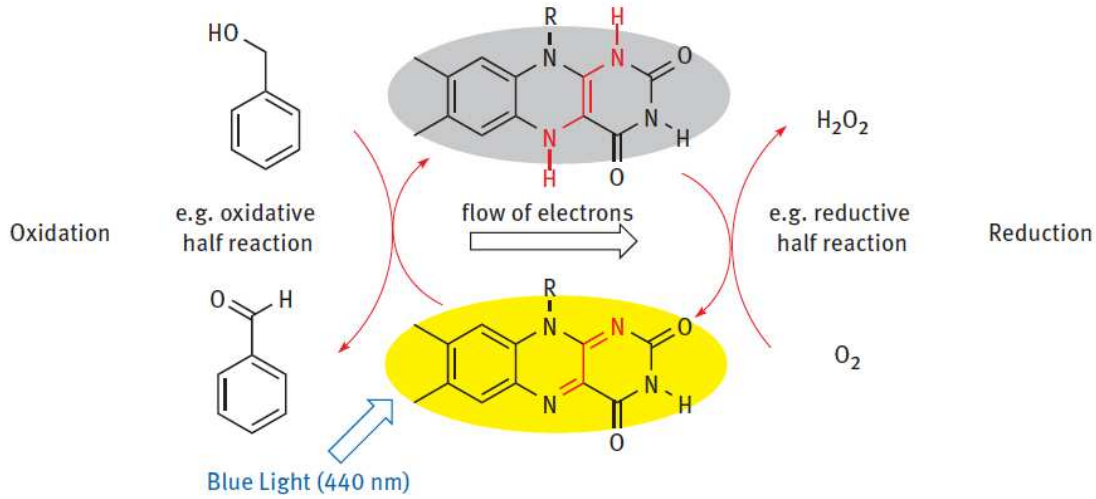

Figure 2.2: Catalytic cycle of flavin redox reactions. Benzyl alcohol oxidation and reoxidation of the catalyst by air [3, Chapter 4, p. 47].

It was shown that after the excited state of flavin is quenched by an electron transfer step, the reaction proceeds via the triplet states of the occurring species of methoxybenzyl alcohol and its intermediates generating the desired aldehyd. Furthermore, electron transfer on the singlet excited state side is a loss channel for the desired reaction.[88]

In order to diversify the catalyst, interest came to roseoflavin (RoF). RoF has in addition to the flavin skeleton a dimethylamino group (DMA) as modification (see also Fig. 2.1). This leads to a possible new chemical photocatalyst with different properties.

Coming back to proteins, replacing the FAD moiety by a roseoflavin-analog, the understanding of the wide and controversial discussed proposals, briefly discussed

before, about the mechanism for the signalling state formation in BLUF proteins could be verified. And indeed, Mathes *et. al.*[89] replaced the FAD chromophore of wild type Slr1694 BLUF domain with a domain in the protein containing RoF to get a deeper general insight in the formation of the signalling state. The main observation from these experiments is the lack of the photocycle and with that the loss of the biological function of the protein by the flavin → RoF exchange.[90] Additionally to that, the behaviour of RoF in different aqueous and organic solvents was also investigated by Zirak *et. al.*[91] There is evidence that RoF might not work as a potential new photocatalyst.

2.2 Motivation and Results

Since there are many experimental studies, reliable results and proposed mechanisms for a photophysical deactivation by intramolecular charge transfer processes for RoF, the general procedure described in the introduction was used to investigate the photophysical properties more detailed on basis of theoretical calculations. For the isolated RoF as well as for RoF solvated in water, the general usability as photocatalyst can be answered by theoretical methods using also the QM/MM scheme. Possible deactivation processes discussed in the literature can be confirmed or rejected and give a new insight into this interesting theme. Also the loss of the biological function of the protein was studied by using QM/MM techniques. Therefore this section is divided in three parts: (i) the study of RoF as isolated molecule, (ii) RoF surrounded by a water environment and (iii) RoF incorporated in the BlrB protein. Throughout this investigation, all QM calculations were done using the TURBOMOLE[92] program package.

2.2.1 Isolated roseoflavin

The first important point to begin with was the determination of the GS geometry of the RoF molecule in gas phase. The orientation of the DMA group relative to the isoalloxzine ring system is crucial, since this is the main difference between

RoF and flavin and could also have some influence inserting this moiety in a protein environment. Therefore a relaxed energy path along the dihedral angle τ (illustrated in Fig. 2.5) was calculated. For the QM calculations of an isolated molecule DFT (using the BHLYP[93] functional) and def-SVP basis[94] was applied.

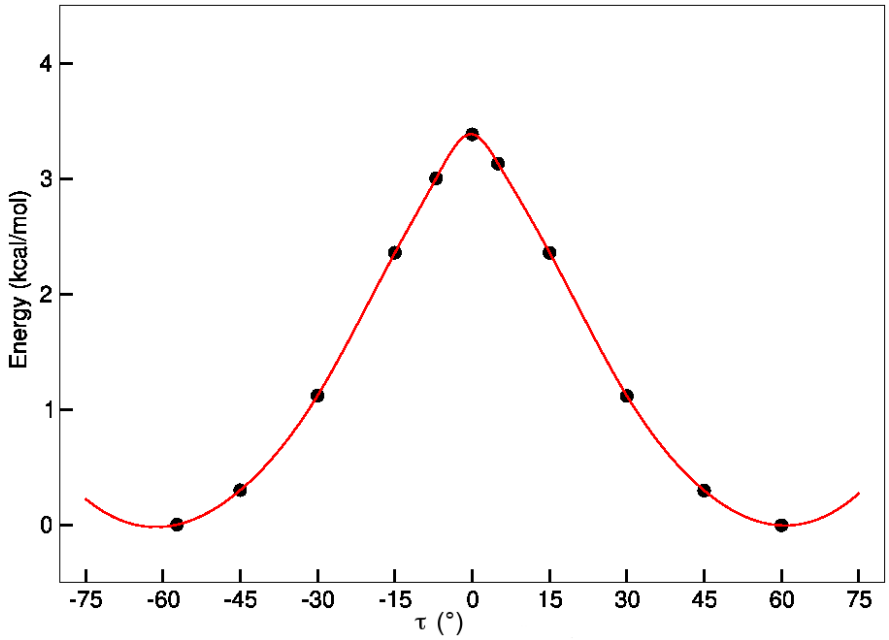

Figure 2.3: RoF in the gas phase : relaxed energy path along the dihedral coordinate τ (see Fig. 2.5) at the level of DFT (BHLYP functional/def-SVP basis)

As one can see in Fig. 2.3, a minimum energy is reached with a dihedral angle of $\tau \approx \pm 60°$ between the DMA group and the isoalloxazine ring system. For the RoF molecule in gas phase the DMA group is kind of electronically decoupled to the ring system, because the DMA group is not in plane with the ring system.

For the gained minimum geometry in the ground state for $\tau \approx -60°$, vertical excitation energies were calculated with different TD-DFT functionals (BP86,[95] B3LYP[22] and BHLYP) with def-SVP basis as well as TD-CC2[18,96,97] with standard auxiliary basis sets,[98] RI approximation[99] and the def-SVP and aug-cc-pVDZ basis sets.[100] The calculations did not aim only for the excitation properties of the molecule, but also for the quality of the different TD-DFT functionals and their applicability for further investigations, especially for the BLUF protein. The

electronic density difference plots and the corresponding oscillator strengths for the first three states were also obtained by the calculations with TD-CC2/aug-cc-pVDZ. They are shown in Fig. 2.4, together with a schematic picture of the excitation energies for the different methods.

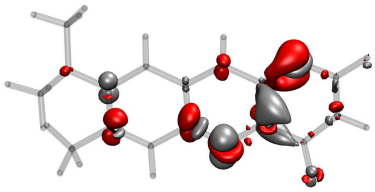

(a) S_1; $\pi_1\pi^*$; ω=2.51 eV; f=0.36; $\Delta\mu$=1.88 D

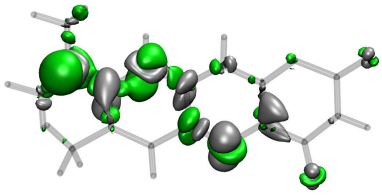

(b) S_2; $\pi_2\pi^*$; ω=3.22 eV; f=0.20; $\Delta\mu$=9.63 D

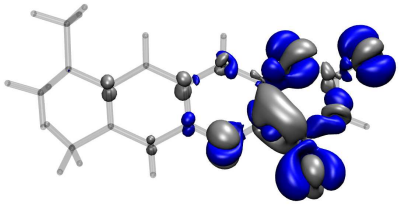

(c) S_3; $n \rightarrow \pi^*$; ω=3.36 eV; f=0.00; $\Delta\mu$=6.18 D

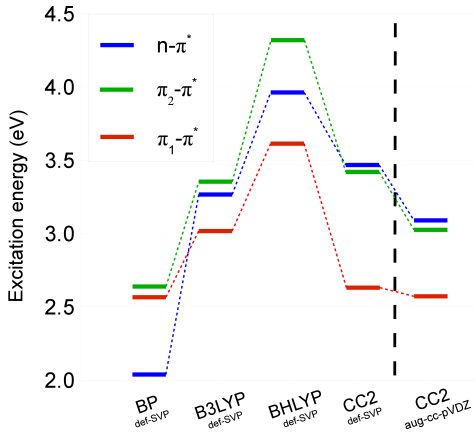

(d) Excitation energies in eV

Figure 2.4: (a)-(c) TD-CC2 density differences (w.r. to the ground state, aug-cc-pVDZ basis) of the first three excited states of RoF. The blue, red, and green isosurfaces at -0.004 show the regions with loss, the grey ones at $+0.004$ the regions with gain of electron density upon photo-excitation. The corresponding oscillator strengths f (on length representation) and the change of the dipole moment $\Delta\mu$ are denoted as well. (d) Vertical excitation energies of RoF in the gas phase calculated with TD-DFT and TD-CC2 response, respectively.

With the corresponding electronic density difference plots and oscillator strengths,

calculated with TD-CC2, the character of the first three excited states were determined (see Fig. 2.4(a) to Fig. 2.4(b)). The S_1 state is of $(\pi_1\pi^*)$ type, the S_2 state of $(\pi_2\pi^*)$ type and the S_3 state is a $(n\pi^*)$ state.

The methods *per se* predict different energetic orders for the $(\pi\pi^*)$ and $(n\pi^*)$ excitations, as is evident from Fig. 2.4(d). With the exception of the BP86 functional, the $(\pi_1\pi^*)$ state is the lowest state. The position of the $(\pi_2\pi^*)$ and $(n\pi^*)$ states differs from TD-DFT to TD-CC2. This is in dept to the inherent self interaction error[26,27] of TD-DFT's local and semi-local functionals. From the dipole moment changes relative to the ground state ($\Delta\mu$) it is obvious, that these states have a little charge transfer character.

The $(\pi_1\pi^*)$ state, which is the HOMO $\rightarrow$LUMO excitation, features the highest oscillator strength and therefore is most likely populated after photo-excitation. Further investigation of this state was done by optimising the geometry at TD-CC2 level. At the fully relaxed geometry, the $S_0 \rightarrow S_1$ transition maintains its $(\pi\pi^*)$ character. The second and third excited states, with $(\pi_2\pi^*)$ and $(n\pi^*)$ characters respectively, switch their energetic order. The energy difference between the $(\pi_1\pi^*)$ and $(n\pi^*)$ state drops from 0.85 eV to 0.52 eV at the $(\pi_1\pi^*)$ minimum. The major geometrical changes during the optimisation at the S_1 PES correspond to particular bond distances in the RoF ring system. The orientation of the DMA group on the other hand is not affected by this relaxation process. The changes in the bond distances were starting point for a more accurate study of this issue. An appropriate linear combination of these bond distances was constructed as a reaction coordinate Q_R for this purpose (see Fig. 2.5 $Q_R = \alpha\times$b(O2-C2)$-\alpha\times$d(C2-N1)$+\alpha\times$d(N1-10a)$-\alpha\times$d(10a-4a)$+\alpha\times$d(4a-N5), whereas $\alpha = 0.4472$). For simplicity the bond distances were not wighted at all. A free geometry optimisation with the constructed linear combination of the bond distances has shown that the global minimum of the S_1 state corresponds to $Q_R = 0.46$ and the minimum geometry along the Q_R path, with $Q_R = 0.45$, are energetically 0.0001 eV and geometrically 0.01 a.u. (RMSD) apart.

A relaxed energy path on the PES of the lowest state was calculated at the TD-CC2 level with def-SVP basis along the reaction coordinate Q_R, starting at the

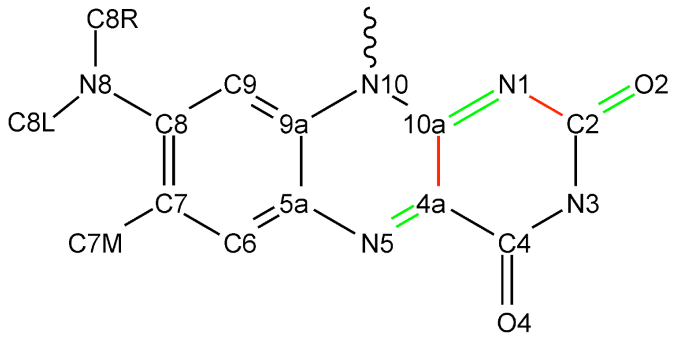

Figure 2.5: Reaction coordinate Q_R. Elongation of bond is denoted in green, contraction in red. The used dihedral angles τ and τ' correspond to (C7,C8,N8,C8L) and (C7,C8,N8,C8R), respectively.

FC-point. This path is displayed in Fig. 2.6.

One can see that the path along Q_R leads to a CI between the $(\pi_1\pi^*)$ and the $(n\pi^*)$ state. After the CI the $(n\pi^*)$ state becomes the lowest state. The step in the energies after this CI between $(\pi_1\pi^*)$ and the $(n\pi^*)$ state is due to the change in geometry of the optimised structure, since the restrained optimisation refers to the lowest state. Continuing the path along Q_R now on the $(n\pi^*)$ state surface, one can observe even a second CI with the ground state. The switching of the energetic order of the $(\pi_2\pi^*)$ and $(n\pi^*)$ states, noted at the S_1-minimum, seems to derive from a third CI between theses states.

The conclusion of the investigation so far is (i) a twisted structure of RoF for the ground state minimum and (ii) a fast deactivation channel from the photo-excited $(\pi_1\pi^*)$ state to the ground state via two CIs in the gas phase occurring via changes in bond distances of the RoF ring system. The DMA group is not affected in the observed CI. This study of RoF also showed that the BHLYP functional seems to be feasible for geometry optimisations of excited states, if using the cheap TD-DFT method. However, energies and corresponding properties should at least be verified by application of the TD-CC2 method.

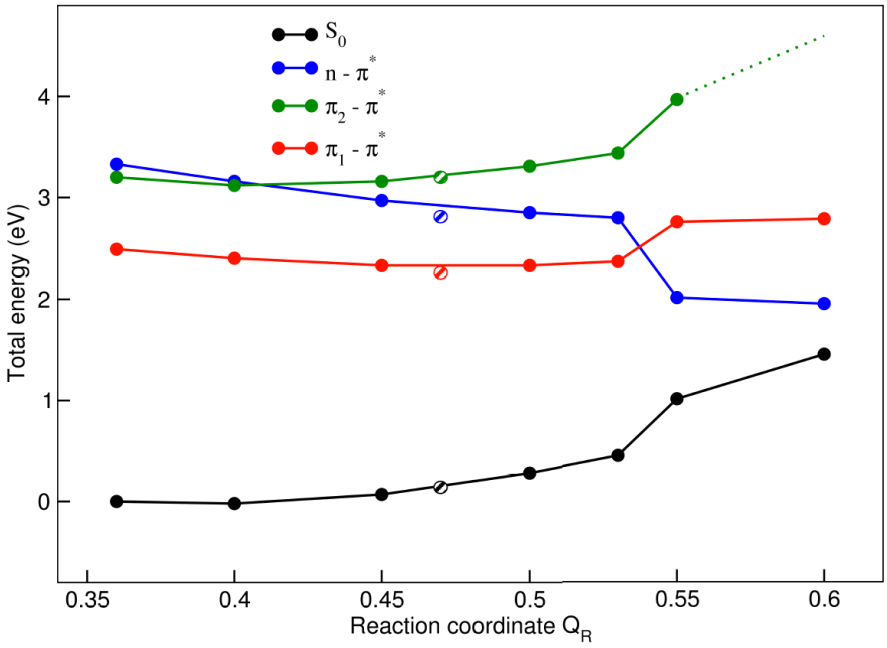

Figure 2.6: Energies (in eV) of the relevant excited states relative to the ground state minimum energy at the relaxed structures along Q_R. The restrained geometry optimisations were performed with TD-CC2 response in the def-SVP basis on the energy surface of the lowest state, *i.e.*, on the $(\pi_1\pi^*)$ surface and on the $(n\pi^*)$ after the conical intersection. The plotted energies correspond to TD-CC2 response single point calculations at these relaxed structures in the bigger aug-cc-pVDZ basis. The shaded points denote the S_1-minimum.

2.2.2 Roseoflavin in water

To solvate the RoF in water a pre-equilibrated water droplet of 25 Å diameter containing 2142 water molecules was used. An extensive MD simulation was not carried out. This part of the study served as an investigation of the influence of the water molecules, represented by "partial" charges in the one-electron part of the QM-Hamiltonian. A MM-minimised structure was used as starting point for the subsequent QM/MM geometry optimisations. A boundary of 2.5 Å thickness to the outer limit of the droplet was restraint by a quartic force of 24 kcal/mol/Å^2 using the miscellaneous mean-field potential (MMFP) implemented in CHARMM.[39]

The potential parameters for the RoF chromophore were taken over from the flavin chromophore.[84] Missing parameters were adopted from the CHARMM27 force field parameters for nucleic and amino acids.[38,101] The list of additional force field parameters and a figure with the corresponding atom numbers and types are given in the appendix (see Fig. A.1, Table A.1, Table A.2 and Table A.3). The parameter for the water molecules were also taken over from the CHARMM27 force field parameters. The QM region was restricted to RoF, while the MM region contained the surrounding water molecules. For the QM/MM calculations, employed by using the ChemShell interface,[102] the coupling between QM and MM was done via the charge shift scheme. The DL-POLY molecular dynamics package[103] incorporated in ChemShell with CHARMM force field parameters was used for the MM part. The implemented HDLCopt-optimiser[104] in ChemShell was chosen for the geometry optimisations. DFT with the BHLYP functional with def-SVP basis set was used combined with the CHARMM force field parameters (BHLYP/CHARMM).

With the QM/MM technique a relaxed energy path (shown in Fig. 2.7) along the dihedral angle τ was calculated. As for the molecule in gas phase, the orientation of the DMA group of RoF embedded in the water environment is an important task to find out.

The stable conformation corresponds to two minima at $\tau \approx \pm 35°$, which shows that the twisting is not that pronounced as in the free molecule. The asymmetry

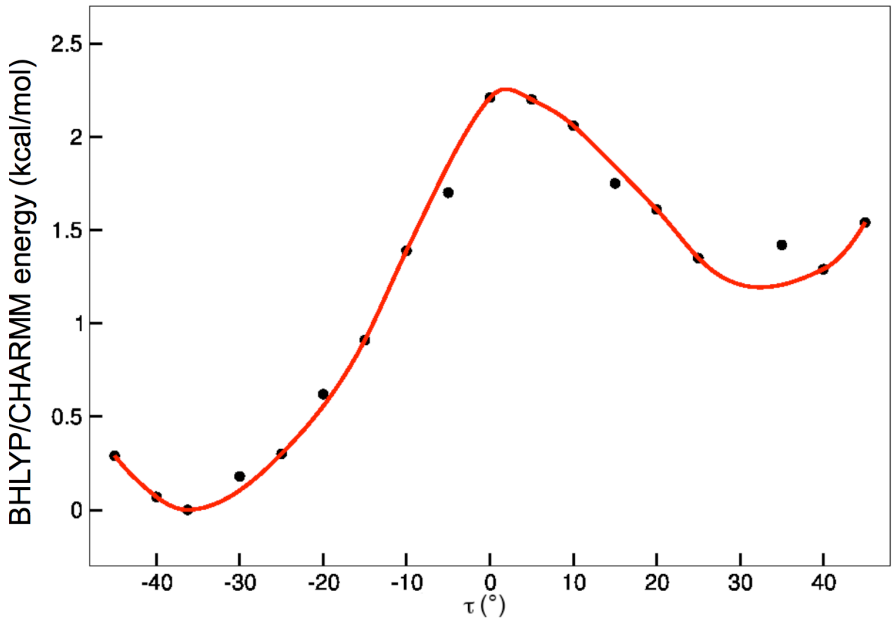

Figure 2.7: BHLYP/CHARMM energies of RoF in water along the dihedral angle τ (defined in Fig. 2.1).

of the QM/MM energies with respect to τ for the two minima in Fig. 2.7 is due to a not fully relaxed solvent environment at the dihedral angle $\tau = +35°$. A symmetric PES with respect to the dihedral angle τ would be obtained once the water environment is fully adapted to the restrained RoF residue. However, this extensive QM/MM MD simulations was avoided, due to the fact, that only the question about the general orientation of the DMA group should be answered qualitatively. Fig. 2.7 clearly shows that the planar conformation has the highest possible energy and thus is not stable in the chosen environment. Therefore it was useful to take the structure with τ = -35° for further investigations of the photophysics of RoF in water. The next step was the calculation of the electronically excited states and their properties for the obtained minimum with TD-CC2/CHARMM and aug-cc-pVDZ basis.

In Tab. 2.8(c) the vertical excitation energies of the two lowest excited states are compiled. The related density difference plots in Fig. 2.8(a) and Fig. 2.8(b) show in comparison with the electron density difference plots of the gas phase (see Fig. 2.4(b)), that the S_1-state corresponds to the ($\pi_2\pi^*$) state in the gas

phase which now is stabilised by the polar water environment. The S_2 state with $(\pi_3\pi^*)$ character corresponds to yet another, higher lying state in gas phase, and is irrelevant for the deactivation of photo excited RoF in water (*vide infra*).

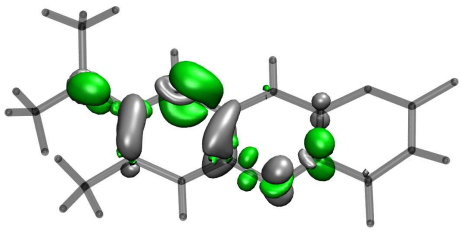

(a) Electron density difference plots of RoF in water for S_1

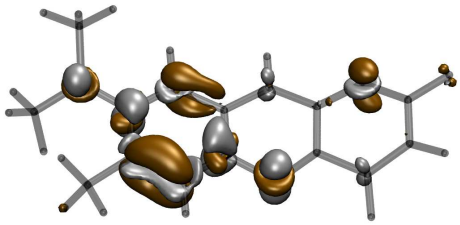

(b) Electron density difference plots of RoF in water for S_2

		S_0-minimum		$S_1^{\Delta Q=0.5}$	
state	type	$\omega[eV]$	f [a.u.]	$\omega[eV]$	f [a.u.]
S_1	$\pi_2\pi^*$	2.49	0.613	0.31	0.091
S_2	$\pi_3\pi^*$	3.08	0.132	2.20	0.016

(c)

Figure 2.8: TD-CC2/CHARMM (aug-cc-pVDZ basis) electron density difference plots for (a) S_1 state ($(\pi_2\pi^*)$ type), (b) S_2 state ($(\pi_3\pi^*)$ type) and (c) a table of the vertical excitation energies ω (in eV) for the S_0-minimum and $S_1^{\Delta Q=0.5}$ structures. The corresponding oscillator strengths, f (in length representation), are also tabulated. Gray and green/brown areas show the regions with gain and loss of electron density relative to the ground state, respectively. The isosurfaces correspond to values of ± 0.004.

Attempts were made to find the minimum on the S_1 state surface. A preliminary restraint-free geometry optimisation at the TD-CC2/CHARMM level leads to two interesting observations. Firstly, the main degree of freedom involved in the relaxation on the S_1 surface is the rotation of the DMA group with respect to the ring system of the RoF moiety. Secondly, there is a large decrease in the S_1-S_0 energy gap along such a rotation, leading to a CI with the ground state for $\tau = -\tau' = 90°$, where the response theory breaks down due to the degeneracy of the reference wave function. One can conjecture that relaxation along this very coordinate is responsible for the deactivation of the first excited state.

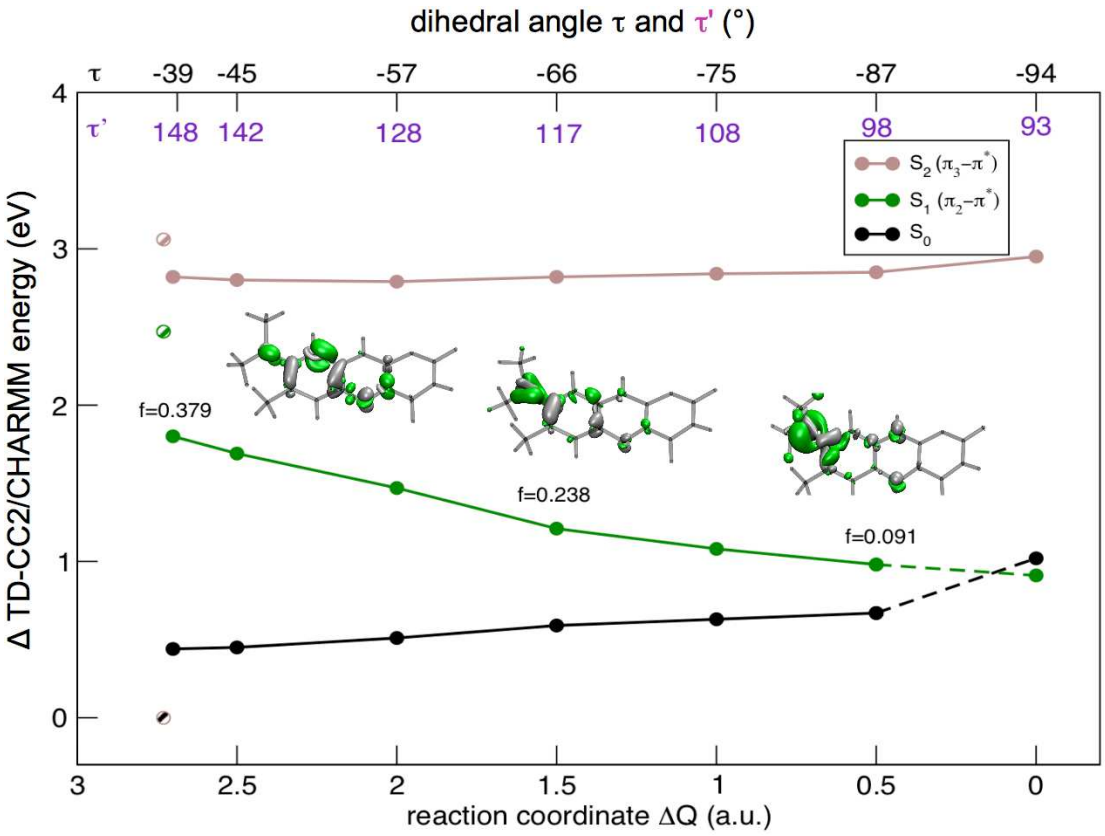

Figure 2.9: TD-CC2/CHARMM energy (in eV) of the ground (S_0) and first exited state (S_1) plotted along the path obtained via constrained geometry optimisation on the S_1 state. The dihedral angles τ and τ' for both, the oscillator strength (f) and the electron density difference plots of some restrained optimised geometries, are shown.

To verify this, a relaxed energy path along τ on the excited state surface for the ($\pi_3\pi^*$) state was computed. Unfortunately, taking the dihedral angle directly leads to a unstable path with metastable restrained geometries, caused by the out of plane angle of the DMA group. Instead, a bond difference coordinate, defined as ΔQ:= d(C8R-C7M) - d(C8L-C7M) was employed (for labels see Fig. 2.5). Such a forced rotation of the DMA group leads downhill from the FC-point on the S_1 surface towards a CI with the ground state at perpendicular orientation of the DMA group ($\tau = -\tau' = 90°$). This rotation represents a fast deactivation channel for the S_1 state of RoF solvated in water. The resulted relaxed energy path along the rotation is shown in Fig. 2.9.

The conclusion of the investigation of RoF embedded in a water droplet is that comparable to the isolated molecule, RoF exists as a twisted structure in the ground state minimum in the water environment and that a fast deactivation channel from the ($\pi_2\pi^*$) state to the ground state via a CI, now the rotation of the DMA group, is observed.

2.2.3 Roseoflavin in protein environment

Due to the fact that there was no crystal structure available in the literature with RoF bound to a BLUF-domain protein, a monomer of a BLUF-domain protein containing FAD was used to get a starting point for the study. Linked to the study of Sadeghian *et. al.*[84] a monomer of the BlrB protein (PDB code: 1BYC)[69] was selected. The flavin moiety artificially was exchanged by a RoF manually, replacing the methyl group at the C8 position of flavin with the DMA group.

This artificial initial structure of the protein containing the RoF moiety was solvated in a pre-equilibrated water droplet with a radius of 20 Å containing 5187 water molecules. During the MD procedure done with the CHARMM program package, the boundary of the droplet (2.5Å) was constrained with a quartic force of 24 kcal/mol/A^2 using the Miscellaneous Mean-Field Potential (MMFP). All bonds to hydrogen atoms were held by SHAKE.[105] For RoF the parameters used before were applied. Before the actual MD simulation the system was heated from 50K to 300K, using a 1 fs time step and 10 K temperature increase for every 25th time step. During this procedure the backbone was constrained in a harmonic potential. This constraint was then lifted gradually and the system was thereafter allowed to relax at 300K over 500000 time steps (≡500ps). The same procedure Sadeghian *et. al.*[84] employed very successfully. The trajectory of the MD simulation along τ is depicted in Fig. 2.10. The structure can be denoted as *planar*, if $\tau \approx 0°$, otherwise as *non-planar*.

As one can see from the obtained MD simulation, the dihedral angle of the DMA group remains more or less planar. As is evident, the two dihedral angles fluctuate around -10° and 170° respectively. Due to the fact that the force field parameters

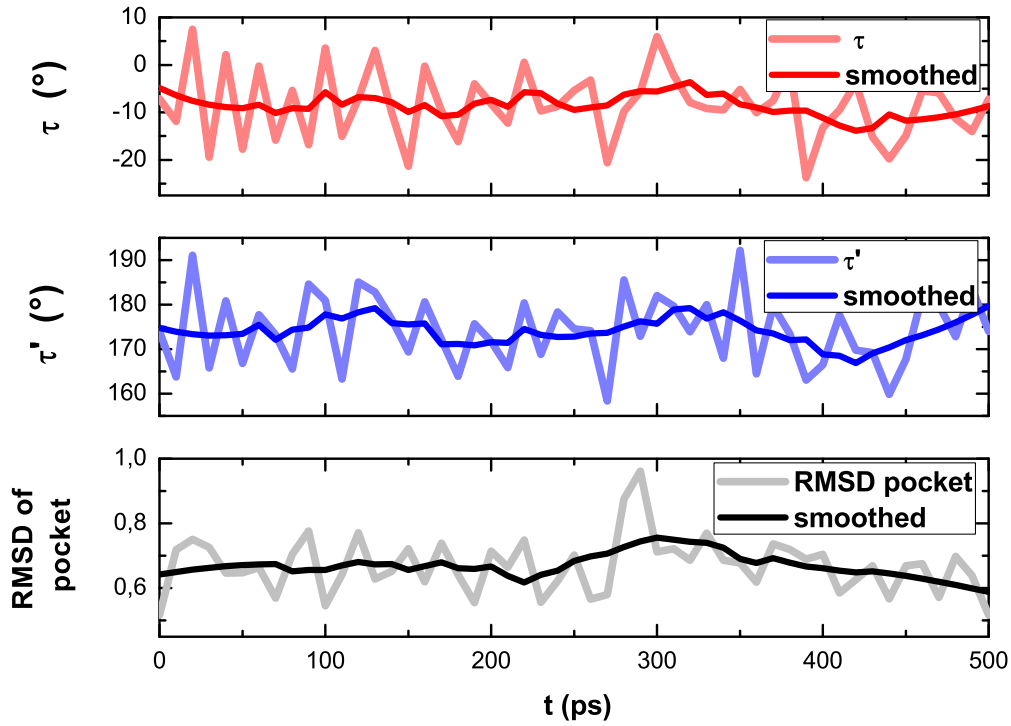

Figure 2.10: Analysis of the MD-trajectory; Values of dihedral angles τ and τ' and RMSD of RoF and adjacent residues along the MD trajectory.

used for RoF are designed only for a planar orientation of the DMA group with respect to the RoF ring system an unbiased QM/MM investigation is required for a more reliable answer. The MD simulation alone is not sufficient to answer this question correctly. Nevertheless, the trajectory can answer the question of the stability of the binding pocket with the RoF ring system inside of it. Since the structure was artificially generated, this question is not negligible. Here, one can see that the binding pocket keeps its general structure (RMSD ≈ 0.6). Considering the stability of the residues within the RoF binding pocket in the production run within the last 100 ps (*cf.* Fig. 2.10) a representative snap shot (at 420 ps) from the MD simulation was chosen for the further QM/MM investigations.

The QM region (shown in Fig. 2.11) includes the RoF moiety (electron acceptor),

consisting of the 8-dimethyl-isoalloxazine with additional methyl group at the N10 position, the Tyr-9 residue (electron donor), the Gln-51 and His-73 residues, a water molecule WAT, as well as the Ser-11 and Asn-33 residues, which are in direct contact with the RoF chromophore. His-73 was protonated at the nitrogen position denoted as NE in the crystal structure.

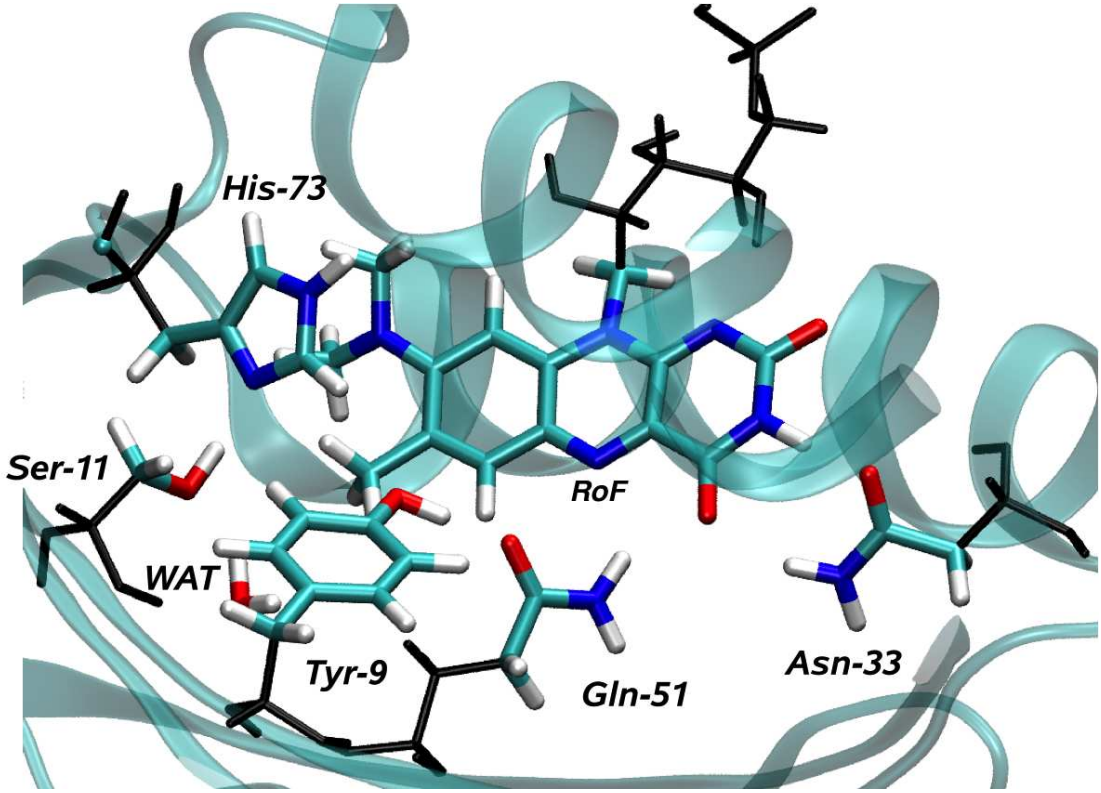

Figure 2.11: QM region of RoF in protein.

The QM/MM coupling was calculated using the charge shift scheme and link atoms were applied to cut bonds. On the MM side, the available CHARMM force field parameters were processed by the DL-POLY molecular dynamics package. Again, for QM/MM geometry optimisations the HDLCopt-optimiser was employed.

The chosen snap shot at 420 ps was then optimised using the DFT/CHARMM method (BP86 functional), which leads to a non-planar orientation of the DMA group (τ = -40°). The obtained geometry, denoted for further reference as $RoF_p^{(np)}$, is depicted in Fig. 2.12(a).

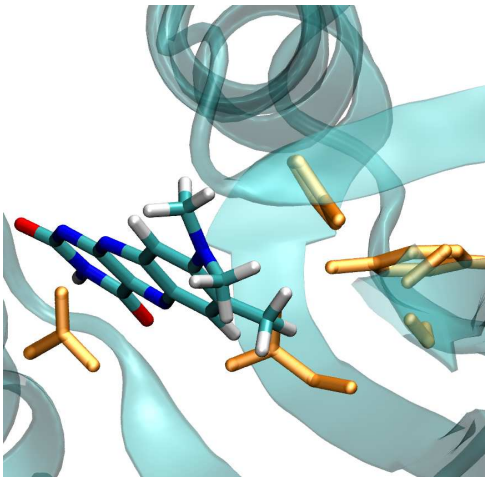

(a) DFT/CHARMM (BP86 functional) optimised $RoF_p^{(np)}$ structure; DMA group with non-planar orientation.

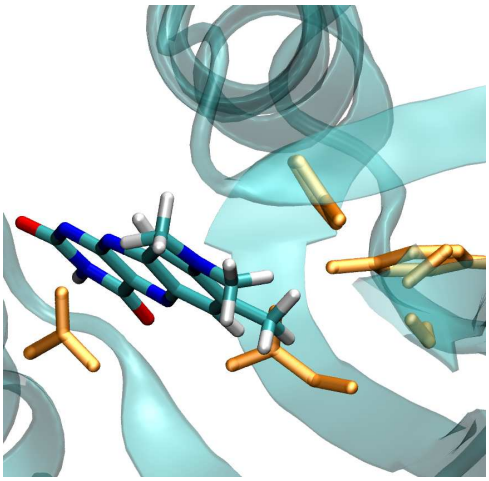

(b) DFT/CHARMM (BP86 functional) optimised $RoF_p^{(pl)}$ structure; DMA group with planar orientation.

Figure 2.12: BP86/CHARMM optimised structures of RoF in the BlrB flavin binding pocket where the non-planar $RoF_p^{(np)}$ (a) and planar $RoF_p^{(pl)}$ (b) conformations are shown.

In order to avoid any bias arising from the choice of the initial geometry a further QM/MM geometry optimisation was performed with the DMA group, first restrained to a planar orientation (by setting τ and τ' to 0 and 180°, respectively) and fully relaxed thereafter in a second step. The resulting geometry (with τ = -170°), denoted in the following as $RoF_p^{(pl)}$, is shown in Fig. 2.12(b).

The $RoF_p^{(pl)}$ structure is energetically more stable (by about 4 kcal/mol) than the *non-planar* $RoF_p^{(np)}$ conformer. Single point MP2/CHARMM calculations (employing the aug-cc-pVDZ basis set) carried out for both structures confirm the DFT/CHARMM (BP86 functional) result. Here, the planar $RoF_p^{(pl)}$ structure is about 3 kcal/mol more stable than its non-planar $RoF_p^{(np)}$ counterpart.

The planarity of the DMA group of RoF is expected to be influenced by the protonation state and orientation of adjacent residues. Here, two possible conformations for the RoF cofactor within the binding pocket of the BlrB BLUF domain were identified. A definite answer to the question of DMA orientation

with respect to the ring system requires further experimental information about the structure and protonation of the amino acids in the close neighbourhood of the RoF chromophore. In the following, based on the two stable conformations $RoF_p^{(pl)}$ and $RoF_p^{(np)}$, the excited states relevant for the photocycle of the wild-type BLUF domains are explored, *i.e.*, the locally excited (LE) state (localised on the chromophore) and the CT state, shifting electron density from the tyrosine to the chromophore. The vertical excitation energies for these two states at $RoF_p^{(pl)}$ and $RoF_p^{(np)}$ geometries, calculated with TD-DFT/CHARMM (BHLYP functional, def-TZVP basis) and TD-CC2/CHARMM with aug-cc-pVDZ basis, are shown schematically in Fig. 2.13 and the results are summarised in Table 2.1. The corresponding electron density difference plots (relative to the ground state density), calculated with TD-CC2/CHARMM (cc-pVDZ basis), are given in Fig. 2.14.

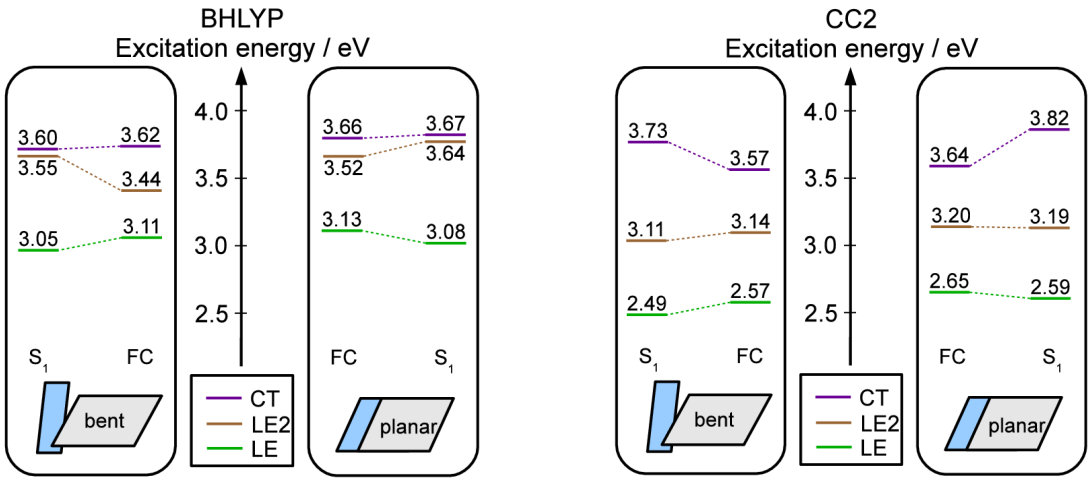

Figure 2.13: QM/MM vertical excitation energies of planar and non-planar RoF conformation at the Frank-Condon (FC) point and at S_1 (LE) optimised structures, calculated (a) with TD-DFT/CHARMM (BHLYP functional) in the def-TZVP basis and (b) with TD-CC2/CHARMM in aug-cc-pVDZ basis.

The LE state with its high oscillator strength ($f \approx 0.6$ a.u. for both, the planar and non-planar RoF conformation) is the state initially populated by the

photo-excitation. In order to initiate a photocycle similar to that observed in the native BLUF domains, population transfer from the LE state to the tyrosine → RoF CT state via a CI then has to take place. TD-DFT is known to underestimate long range charge transfer states. Here, this underestimation is alleviated by employing the BHLYP functional containing 50% exact HF-exchange. In fact, in the planar, as well as in the non-planar structure, the CT state lies energetically above the LE state for TD-DFT/CHARMM (BHLYP functional) as well as for TD-CC2/CHARMM. However, TD-DFT/CHARMM overestimates the excitation energies of the LE state in comparison to TD-CC2/CHARMM. The TD-CC2/CHARMM excitation energies themselves are rather stable *w.r.* to the basis set size and do not show any dramatic changes when the basis set is augmented by diffuse functions (see also Table 2.1).

Table 2.1: QM/MM excitation energies ω in eV for the optimised ground state (GS) structure and for the LE-state structure of $RoF_p^{(pl)}$ and $RoF_p^{(np)}$ conformations. $\Delta\omega$ depicts the gap between the LE and CT state.

optimised state	method	basis set	geometry	ω(LE)	ω(LE2)	ω(CT)	$\Delta\omega$
S_0	BHLYP	def-TZVP	$RoF_p^{(np)}$	3.11	3.44	3.62	0.51
			$RoF_p^{(pl)}$	3.13	3.52	3.66	0.53
	CC2	cc-pVDZ	$RoF_p^{(np)}$	2.68	3.22	3.78	1.10
			$RoF_p^{(pl)}$	2.75	3.31	3.85	1.10
		aug-cc-pVDZ	$RoF_p^{(np)}$	2.57	3.14	3.57	1.00
			$RoF_p^{(pl)}$	2.65	3.20	3.64	0.99
(LE)	BHLYP	def-TZVP	$RoF_p^{(np)}$	3.05	3.55	3.60	0.55
			$RoF_p^{(pl)}$	3.08	3.64	3.67	0.59
	CC2	cc-pVDZ	$RoF_p^{(np)}$	2.60	3.24	3.95	1.35
			$RoF_p^{(pl)}$	2.69	3.31	4.03	1.34
		aug-cc-pVDZ	$RoF_p^{(np)}$	2.49	3.11	3.73	1.24
			$RoF_p^{(pl)}$	2.59	3.19	3.82	1.23

The excitation energy of the LE state is rather insensitive *w.r.* to the orientation of the DMA group and remains at about 2.6 eV for both, the planar and the non-planar conformation. In contrast to the native BLUF domain, the tyrosine → RoF

CT state at about 3.6 eV, which is relevant for the biological functionality of the protein, corresponds not to the second, but to the third excited state. Between the LE and the CT state there is another excited state, located on the RoF subunit, with very low oscillator strength, denoted as LE2 in the following. LE and LE2 appear to correspond to the S_1 and S_2 states of RoF in water, respectively, as can be seen by comparing the electron density difference plots of Fig. 2.14 for RoF in protein and Fig. 2.8 for RoF in water.

Starting from the FC-points QM/MM geometry optimisations were carried out with TD-DFT/CHARMM (BHLYP, def-TZVP basis) on the LE state surfaces of both conformations. Subsequently, vertical excitation energies at the respective LE-minimum structures were calculated with TD-DFT/CHARMM (BHLYP, def-TZVP basis) and TD-CC2/CHARMM in the aug-cc-pVDZ basis. The resulting excitation energies at the respective LE minimum structures are shown in Fig. 2.13 and Table 2.1. Evidently, for both, the planar and non-planar RoF conformation, the CT state not only remains above the LE state, but the LE-CT gap even *increases* going from the FC-points to the LE minima. The LE2 state in between, on the other hand, hardly changes energetically. In particular, no crossing of states is observed. This implies that no CI exists close to the LE minimum for RoF substituted BLUF domains and the tyrosine → RoF CT state thus *cannot* be populated efficiently after photo-excitation. This is in strong contrast to the case of native BLUF domains, where the LE-CT gap closes towards the LE-minimum,[84–86] and explains the lack of a photocycle and the loss of the biological function of RoF substituted BLUF domains in experimental observations.[90]

However, additional calculations with an artificially increased dihedral angle τ for the DMA group of RoF in the protein environment were carried out, to have an indication for a possible deactivation channel for the LE state, comparable to the investigations for the isolated RoF and RoF in water, respectively. The new upright structure was not further optimised. For calculations of electronically excited states TD-CC2/CHARMM with the cc-pVDZ basis set was used and compared to optimised geometries of planar and non-planar RoF conformation (QM/MM excitation energies for $RoF_p^{(np)}$ and $RoF_p^{(pl)}$ at the FC-point were recomputed with

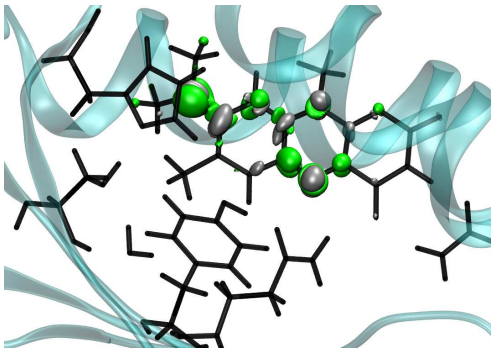

(a) S_1 LE state; ω=2.57 eV; f=0.67; $\Delta\mu$=3.71 D

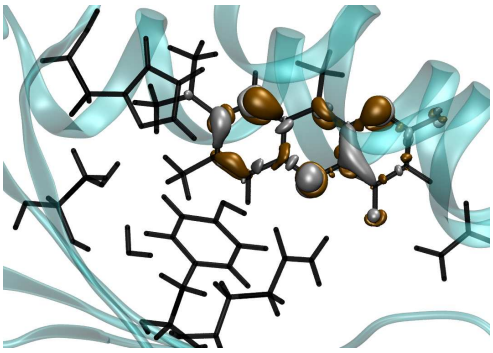

(b) S_2 LE2 state; ω=3.14 eV; f=0.03; $\Delta\mu$=1.66 D

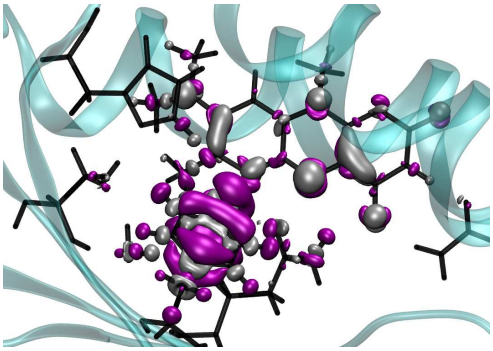

(c) S_3 CT state; ω=3.57 eV; f=0.00; $\Delta\mu$=18.70 D

Figure 2.14: TD-CC2/CHARMM (with cc-pVDZ basis) electron density difference plots for (a) the LE, (b) the LE2 and (c) the CT state at $RoF_p^{(np)}$ geometry. Gray and green/brown/purple areas show the regions with gain and loss of electron density relative to the ground state, respectively. The isosurfaces correspond to values of ±0.003. The corresponding oscillator strengths f (on length representation, calculated with aug-cc-pVDZ basis) and the change of the dipole moment ($\Delta\mu$) are denoted as well.

TD-CC2/CHARMM and the cc-pVDZ basis set for a comparison). The results are shown schematically in Fig. 2.15.

As one can see, there might be an indication for a mechanism analogous to that of RoF in water and could be responsible for the fluorescence quenching of RoF in the BLUF domain also observed in experiment.[90] Since the main aspect of the investigation of RoF in the protein was, to see if the CT state can be populated

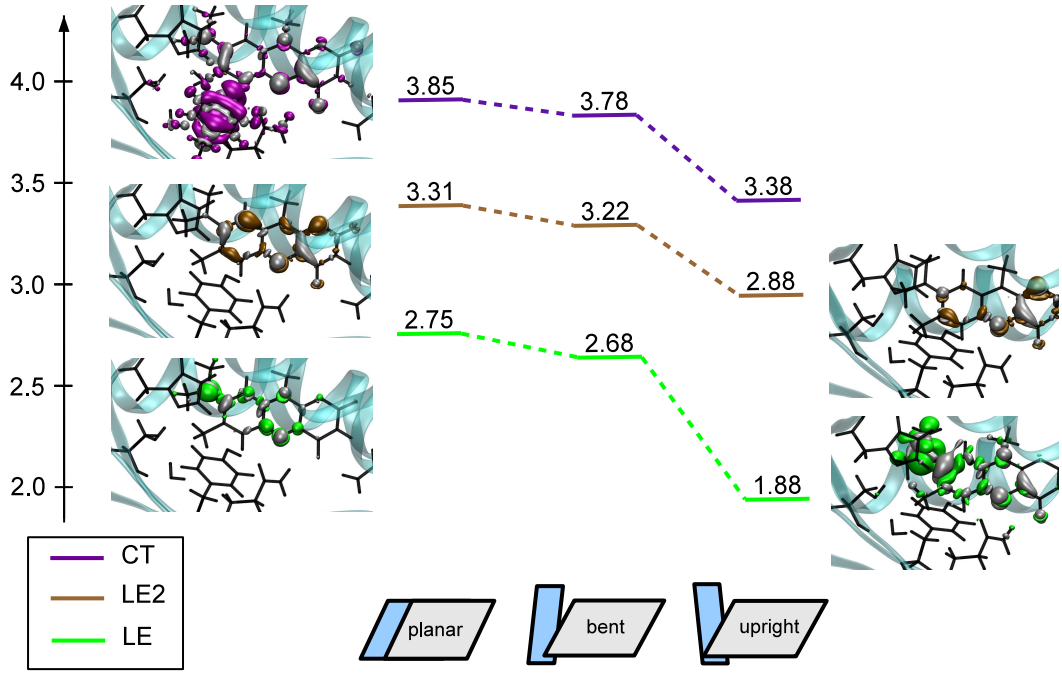

Figure 2.15: QM/MM excitation energies of planar, non-planar or bent (both optimised with BP86/CHARMM at the FC-point) and upright (not optimised) RoF conformation calculated with TD-CC2/CHARMM in cc-pVDZ basis.

efficiently after photo-excitation, no further steps were done to verify a concrete deactivation channel.

The conclusion of the investigation of the modified BLUF protein is that there is **no** CI close to the LE minimum for this kind of proteins, which is in contrast to the native BLUF proteins. This is an interesting point, because this study supports the very first steps of the proposed mechanism by Sadeghian *et. al.* . Additionally, there is at least an indication for an additional deactivation channel for the LE comparable to RoF in water environment.

2.3 Discussion

Based on all results obtained in this study, the photophysics of RoF in gas phase, in water and embedded in BlrB BLUF domain are shown schematically in Fig. 2.16. Even though the individual conical intersections were not mapped out in detail here, the following hypotheses can be put up.

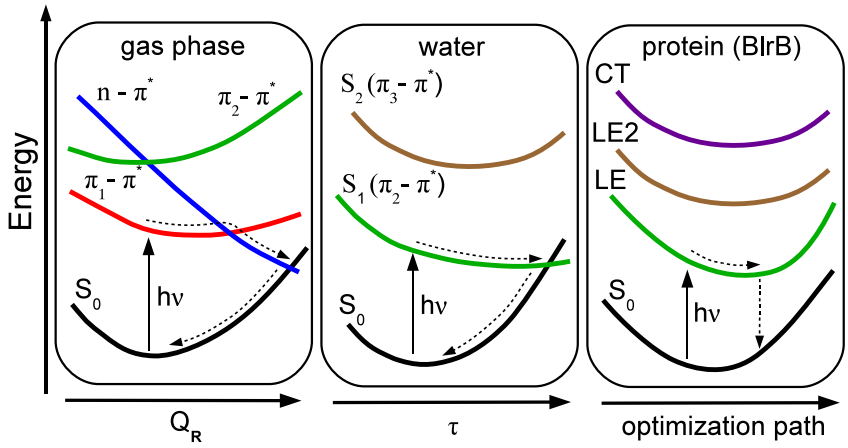

Figure 2.16: Qualitative picture of the different excited state characteristics of RoF in different environments. In gas phase a quasi-PICT mechanism via intramolecular charge-shifting is observed, whereas in water a quasi-TICT mechanism via an intramolecular charge-shifting between the π-system and the DMA-group is found. In protein environment no CI between CT- and LE-state is found, in contrast to the wild type BLUF domain.

In gas phase the bright locally excited ($\pi_1\pi^*$) state is deactivated via a CI with the dark ($n\pi^*$) state. The latter is deactivated further via a second CI with the ground state. In water, on the other hand, the initially populated ($\pi_2\pi^*$) state is deactivated directly via a CI with the ground state. The ($n\pi^*$) state does not seem to play any role here. Of further interest are the modes which are mainly responsible for deactivating the excited states. In gas phase an in-plane ring mode

appears, driving the deactivation process, which would fit to the picture of a planar intramolecular charge transfer (PICT)[106] model also proposed by Zirak *et. al.*[91]

In water, on the other hand, the rotation of the DMA group with respect to the ring system is of prime importance for deactivation, which in turn would fit to the picture of a twisted intramolecular charge transfer (TICT)[107] model. Actually, the significant fluorescence quenching of RoF in water, observed by Zirak *et. al.*,[90,91] was also assigned to a TICT model (on the basis of low temperature measurements) by these authors.

The situation is quite different for RoF embedded in the BlrB BLUF domain. TD-CC2/CHARMM calculations showed that the ($n\pi^*$) state does not exist among the six lowest states. Instead, the locally excited (LE) state of RoF, and the tyrosine →RoF charge transfer (CT) state do occur, which are already known from previous work on the native BlrB BLUF domain. A QM/MM geometry optimisation of the LE state however shows that in strong contrast to the native BLUF domain, no low lying conical intersection near the LE minimum exists, which would be beneficial for population transfer from the LE to the CT state. The CT state thus is not populated after photo-excitation and, as a consequence, the whole reaction cascade leading via proton transfer and tautomerization of the glutamine residue to the signalling state in the native BLUF case, cannot take place. This explains the experimental observations such as the absence of a photocycle and the loss of the biological functionality of RoF substituted BLUF domains. Thus, in contrast to the conjecture derived from experimental results,[90] a TICT deactivation of RoF is not the prime reason for their dysfunctionality.

3 Benzophenone in dinucleotides as photocatalyst

The content of this chapter has been published in Physical Chemistry Chemical Physics.[108] Parts of the text are identical to the publication. Besides some changes in formulations the publication was revised concerning the context given in this thesis, i.e. basic principles, which were discussed in Chapter 1 and the appendix of the publication was integrated into the text. The investigation was supported by spectroscopical measurements, done by Riedle *et. al.* , which are presented in Section 3.2, and organic synthesis, done by Wagenknecht *et. al.* .

3.1 Introduction

Benzophenone (*BP*) is one of the best studied organic chromophores for biological photochemistry and chemical photocatalysis due to the very efficient inter-system crossing (ISC) to the triplet state (T_1).[109–119] With respect to photoaffinity labelling in chemical biology there are several other advantages[110] why the triplet photochemistry of *BP* is useful:[109] (i) Benzophenone behaves chemically more stable than azides and diazirines, especially under harsh conditions of chemical peptide and nucleic acid synthesis. (ii) The T_1 state of *BP* is able to abstract hydrogen atoms from unreactive C-H bonds in biopolymers, e.g. α-hydrogen from amino acids.[111] (iii) The absorption of *BP* in the UV-A region allows selective excitation outside the typical absorption range of biopolymers (including tryptophane in proteins and DNA/RNA bases). On the other hand, *BP* plays an increasingly important role as an excitation antenna collecting the light and thereby initiating

substrate conversion in photochemical reactions.[112,113] Molecular benzophenone architectures can be considered as chemical photocatalysts if they bear a substrate binding site. With such a structure a substrate conversion occurs initiated by energy or electron transfer.[114] In fact, both processes have been applied successfully for the development of *BP*- and xanthone-based photoorganocatalysts.[115] Template-assisted triplet energy transfer yields enantioselective [2+2] cycloaddition[116–118] and, more importantly, templated photo-induced electron transfer can be applied for enantioselective aminocyclizations.[119] Stable C-C bonds are formed in these reactions and therefore both types of photocatalytic reactions are synthetically highly valuable.

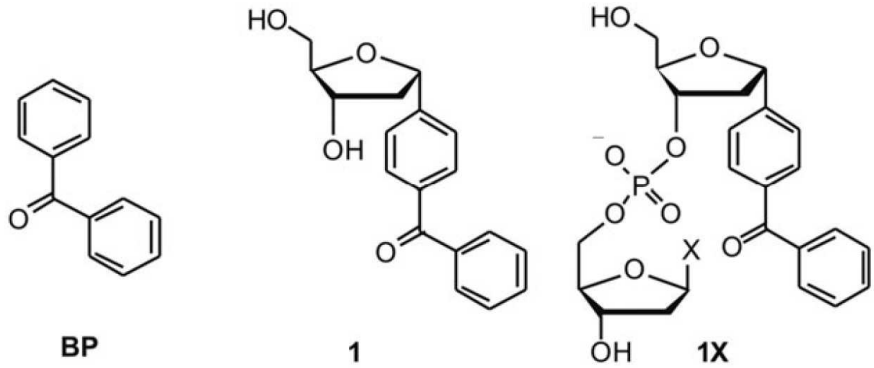

Figure 3.1: BP nucleoside **1** and dinucleotides **1X** with BP as an artificial DNA base (X = G, T, A, C).

With respect to the mentioned properties of BP and its derivatives, covalent conjugates with nucleosides and nucleic acids could be of significant interest for both photocatalysis and chemical photobiology.[120–124] In the latter case, new photoaffinity labels based on nucleic acids help to identify DNA- and RNA-binding proteins. More importantly, *BP* as an artificial nucleoside provides the molecular basis to develop photocatalytically active DNAzymes. Among the few examples found in literature, benzophenone-substituted nucleosides have been prepared as models for ribonucleotide reductases[120] and as photoreactive dyads.[122] *BP* has been attached to phosphorothioates in RNA[123] and to 2'-desoxyuridine in DNA[124] to form interstrand crosslinks. 4-Cyanobenzophenone-substituted 2'-desoxyuridines have been extensively used for photoinduced electron transfer studies with DNA.[125]

Recently, the synthesis of a novel C-nucleoside consisting of *BP* directly attached to the anomeric centre of 2'-desoxyribofuranoside was presented.[126] Thereby, the chromophore is placed as an artificial DNA base and can be incorporated synthetically into oligonucleotides by automated phosphoramidite chemistry (see Fig. 3.1).

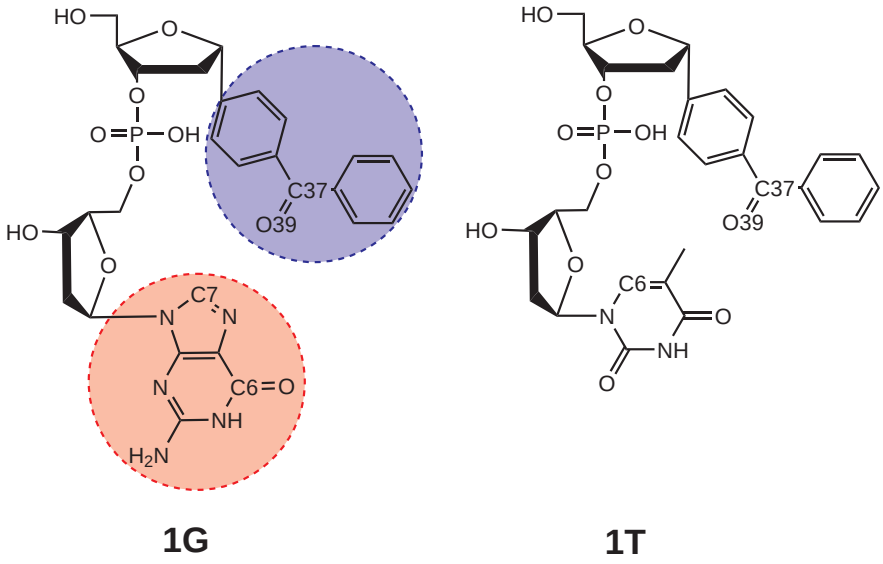

Figure 3.2: Dinucleotides **1G** and **1T** with labels; in molecular structure of the **1G** dinucleotide benzophenone (*BP*) is highlighted in light blue and the guanidine (*G*) in light red. These parts were also used as QM-region (*vide infra*).

These newly synthesised molecules were the staring point for an extensive theoretical investigation, using the general procedure presented earlier, to describe the photochemical properties of **1G** and **1T** (see Fig. 3.2) in the two solvent environments water and methanol.

3.2 Motivation and Results

Special interest in this topic of dinucleotides lies in the influence of each of the four different DNA bases on the photophysical behaviour of BP. Thereby this approach provides the best chance to get a profound understanding of *BP* interactions in nucleic acids. BP as an artificial nucleoside allows selective excitation of its photo-

chemically important ($n\pi^*$) transition outside the typical nucleic acid absorption range (>300 nm), which is an important prerequisite for using the chromophore in photochemistry and photobiology. Using QM/MM methods highlights this topic together with spectroscopic investigations. It was shown that the steady-state phosphorescence of both, nucleoside **1** and dinucleotides **1X** in methanol, show similar maxima at ≈440 nm, whereas **1** dissolved in H_2O exhibits red-shifted phosphorescence at ≈470 nm, because the chromophore is exposed to water. On the other hand, the phosphorescence of the dinucleotides **1X** in H_2O is shifted back (=hypsochromically) and shows similarity to MeOH. These steady-state results imply already the basic idea of different geometries in H_2O vs. MeOH and the conformational control of BP interactions, provided by the two different solvents. The results show that the DNA base adjacent to the *BP* in the dinucleotides is able to shield the chromophore from water. By employing ultra fast transient absorption spectroscopy it was found that the life time of the excited ($n\pi^*$) singlet state at 329 nm is primarily determined by fast inter system crossing (ISC) to the lowest triplet state. In MeOH, **1** features a somewhat reduced ($n\pi^*$) singlet lifetime of 9.4 ps relative to the BP monomer (12.5 ps). The life times of the dinucleotides **1X** (≈9 ps) are slightly decreased relative to **1**. This effect is most pronounced for **1G** (7.6±0.5 ps). These observations indicate an electron transfer from the DNA base (especially guanine) to the S_1 state of the *BP* chromophore, which competes with the ISC process. Changing the solvent from MeOH to H_2O has quite a dramatic effect: The ($n\pi^*$) state life time of **1G** now drops to 4.6 ps, while the life times of the other dinucleotides **1X** with $\mathbf{X} = T$, A or C are much less affected. This can be attributed to an additional decay channel (apart from ISC), which transfers population from the ($n\pi^*$) singlet to a charge transfer (CT) singlet state. The population transfer to the CT state is not very efficient, but competitive to ISC for the **1G** dinucleotide in H_2O.

In order to further explore this peculiar behaviour of the **1G** dinucleotide, this system was studied with the steps of the general procedure described in Chapter 1. For a first overview, pure QM investigations (using TD-DFT with B3LYP functional and (TD-)CC2) for the isolated molecules **1G** and **1T** were carried out (see Section 3.2.1), followed by MD simulations of these two molecules (results are

presented in Section 3.2.2) and ending with extensive hybrid quantum mechanics/molecular mechanics (QM/MM) calculations (for details *vide infra*) for **1G** solvated in methanol and water, respectively (see Section 3.2.3). Throughout, the TURBOMOLE program package was used for the QM calculations.

3.2.1 Isolated 1G and 1T

Starting point for this study was a geometry optimisation of the GS for isolated **1G** and **1T** systems. DFT (BP86 functional, def-SVP basis set) and CC2 (same basis set) geometry optimisations were performed to find a global minimum. For the DFT geometry optimisations two competitive basic geometries were found for either, **1G** and **1T**: (i) a compact, folded structure and (ii) a stretched, unfolded structure. The latter constitutes a local minimum in both cases on the PES. For the optimisations at CC2 level, the unfolded structure is found to be not stable and it folds to the compact geometry. The reason for this is the absence of long range van-der-Waals dispersion in the pure DFT/BP86 description. This can be repaired to some extent, e.g., by inclusion of Grimme's -D2 correction,[127,128] which is employed in the subsequent DFT QM/MM calculations. For the isolated **1G** and **1T** the obtained geometries are displayed in Fig. 3.3 and Fig. 3.4, respectively.

As one can see, the natural DNA base and one of the phenyl rings undergo π-stacking. Two distances were chosen in this case to compare both structures, namely d(C6-O39) and d(C6-C37) (labels see Fig. 3.2). For the unfolded **1G** the distances amount to round about 15 Å and for the folded to 6 Å. This is comparable to **1T**.

Here the distances are about 14 Å for the unfolded and 5 Å for the folded case (see Fig. 3.4). This is about 1 Å shorter than in the **1G** case, but still in the same range. Nevertheless, for both systems the folded as well as the unfolded geometries were investigated further, although the global minimum corresponds to the folded molecule, because the unfolded structure reappears again in the methanol environment (*vide infra*).

The next step was the calculation of excitation energies and electron density dif-

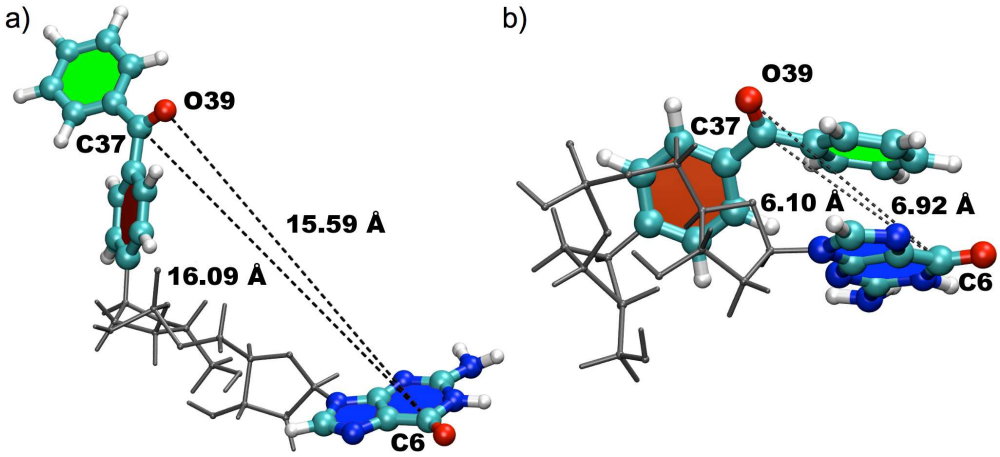

Figure 3.3: Optimised structures of **1G** in the gas phase. The five and six-membered rings are coloured in red/green and blue for better recognition. Also the distances d(C6-O39) and d(C6-C37) are given (see Fig. 3.2). (a) Unfolded structure computed with DFT/BP in the def-SVP basis; d(C6-O39)=15.59 Å and d(C6- C3)=16.09 Å. (b) Folded structure computed with CC2/def-SVP; d(C6-O39)=6.92 Å and d(C6-C37)=6.10 Å

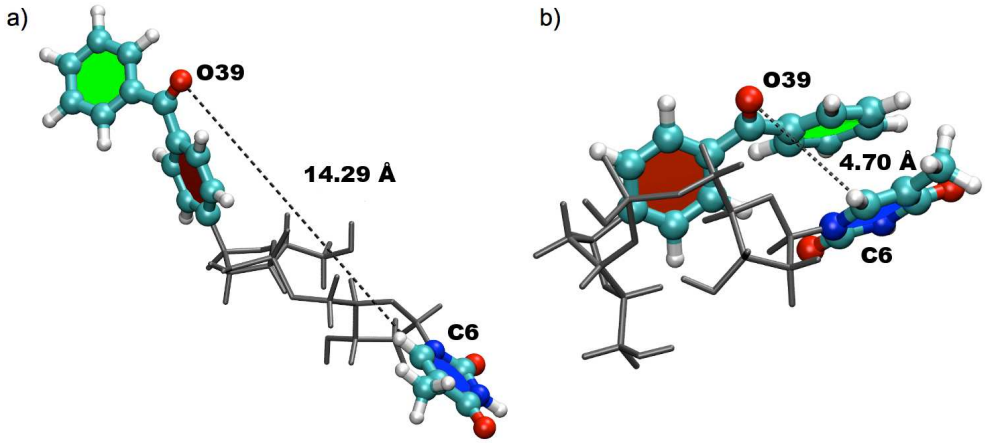

Figure 3.4: Optimised structures of **1T** in the gas phase. The five and six-membered rings are coloured in red/green and blue for better recognition. Also the distance d(C6-O39). (a) Unfolded structure computed with DFT/BP in the def-SVP basis; d(C6-O39)=14.29 Å (b) Folded structure computed with CC2/def-SVP; d(C6-O39)=4.70 Å

ferences between the excited and the GS and related dipole moment differences of the three lowest singlet states at the respective ground state minima for the

isolated dinucleotides, following the general procedure. To see the applicability of TD-DFT the B3LYP functional was chosen and compared to TD-CC2 results. For these calculations the def-SVP basis set was used. To see the influence of the basis set, also the aug-cc-pVDZ was applied to TD-CC2, but only for the calculation of excitation energies. The excitation energies for all discussed cases are compiled in Table 3.1.

Table 3.1: Excitation energies and type of the corresponding states for folded and unfolded **1G** and **1T** in the optimised ground state; results were obtained through TD-B3LYP/def-SVP, TD-CC2/def-SVP and TD-CC2/ aug-cc-pVDZ calculations.

method		folded geometry				unfolded geometry			
		1G		**1T**		**1G**		**1T**	
	state	type	ω [eV]	type	ω [eV]	type	ω [eV]	type	ω [eV]
B3LYP	S_1	$(n\pi^*)$	3.36	$(n\pi^*)$	3.53	$(n\pi^*)$	3.50	$(n\pi^*)$	3.50
	S_2	CT	3.54	CT	4.16	CT	3.56	CT	4.42
	S_3	$(\pi\pi^*)$	4.42	$(\pi\pi^*)$	4.46	$(\pi\pi^*)$	4.45	$(\pi\pi^*)$	4.46
CC2 def-SVP	S_1	$(n\pi^*)$	3.74	$(n\pi^*)$	3.74	$(n\pi^*)$	3.82	$(n\pi^*)$	3.76
	S_2	CT	4.59	$(\pi\pi^*)$	4.79	$(\pi\pi^*)$	4.88	$(\pi\pi^*)$	4.82
	S_3	$(\pi\pi^*)$	4.78	$(\pi\pi^*)$	4.83	$(\pi\pi^*)$	4.96	$(\pi\pi^*)$	4.9
CC2	S_1	$(n\pi^*)$	3.63	$(n\pi^*)$	3.61	$(n\pi^*)$	3.63	$(n\pi^*)$	3.63
aug-cc-	S_2	CT	4.33	$(\pi\pi^*)$	4.65	$(\pi\pi^*)$	4.69	$(\pi\pi^*)$	4.69
pVDZ	S_3	$(\pi\pi^*)$	4.66	$(\pi\pi^*)$	4.68	$(\pi\pi^*)$	4.78	$(\pi\pi^*)$	4.76

Fig. 3.5 depicts the related electron density differences of the folded **1G** and **1T** geometries. From these plots, the characters for the first three singlet excitations were assigned. For the folded geometry of **1G** the S_1, S_2, and S_3 states are of $(n\pi^*)$, charge transfer (CT), and $(\pi\pi^*)$ type. These information were obtained through the reliable calculations at the TD-CC2 level. The CT state features depletion of electron density on *G*, and increase of electron density on the *BP* part. The change of the dipole moment ($\Delta\mu$) is about 10 D, which is reasonable for such states. Comparison of the energy gap between the $(n\pi^*)$ and CT state illustrate a substantial increase from TD-DFT/B3LYP (0.18 eV, def-SVP) to TD-CC2 (0.85 eV, def-SVP or 0.70 eV, aug-cc-PVDZ). Once again, another example

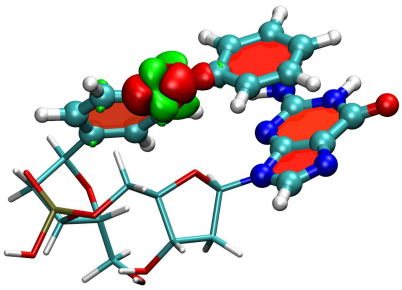

(a) S_1; ($n\pi^*$) state; $\Delta\mu$=1.72 D

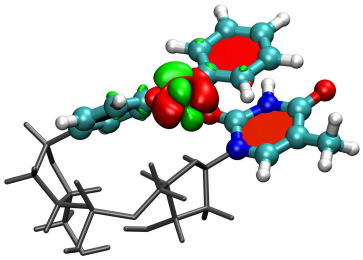

(b) S_1; ($n\pi^*$) state; $\Delta\mu$=1.31 D

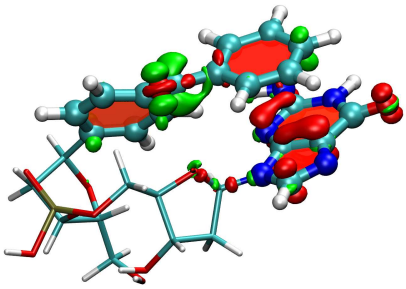

(c) S_2; CT state; $\Delta\mu$=10.58 D

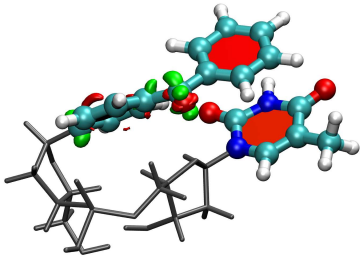

(d) S_1; ($\pi\pi^*$) state; $\Delta\mu$=1.15 D

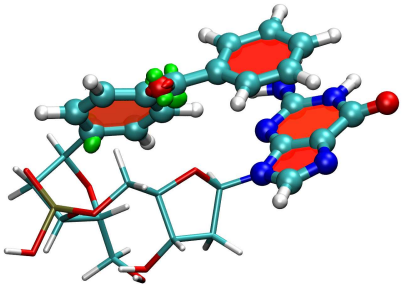

(e) S_3; ($\pi\pi^*$) type state; $\Delta\mu$=1.32 D

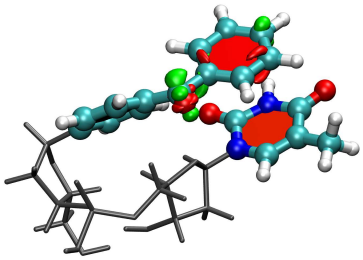

(f) S_1; ($\pi\pi^*$) state; $\Delta\mu$=1.92 D

Figure 3.5: Electron density difference plots for the first three excited states of folded **1G** (left hand side) and **1T** (right hand side) geometries, calculated with TD-CC2 in def-SVP basis. Isosurfaces are plotted for ±0.005 a.u., red refers to a decrease, green to an increase in the density upon excitation.

for the electronic self-interaction problem inherent in TD-DFT for CT states, which leads to an underestimation of the excitation energies by TD-DFT with local as well as semi-local functionals.

The excitation characters of isolated **1T** on the other hand, features a CT state among the three lowest states for the TD-DFT calculations only for the folded molecule. The order and type of characters is similar to **1G**. Looking at the gap between the ($n\pi^*$) and CT state shows a significant increase to 0.63 eV, which is about 0.45 eV higher compared to **1G**. Hence, the CT state in the TD-DFT calculation for **1T** is just an artifact, caused by the aforementioned electronic self-interaction problem, since the CT state disappears for folded **1T** in a TD-CC2 calculation. The S_1, S_2, and S_3 correspond to a ($n\pi^*$), ($\pi\pi^*$) and ($\pi\pi^*$) type, respectively.

For both unfolded geometries (**1G** as well as **1T**) the S_1, S_2, and S_3 calculated by TD-CC2 are of ($n\pi^*$), ($\pi\pi^*$), and ($\pi\pi^*$) type. A CT state of **1G** is absent, which is not too surprising, since the distance between donor (*G*) and acceptor (*BP*) is much larger than in the folded geometry.

On the other hand, a CT state (S_2) for the unfolded **1G** and **1T** is observed with a TD-DFT calculation and features about the same excitation energy as in the folded geometry. This is the typical irregular behaviour of TD-DFT, since CT states described by that method do not reflect the proper distance dependence between donor and acceptor (according to the Coulomb law).

Based on the gas phase results presented so far one can conclude that (i) the distance between the *BP* and the *G* subsystems intimately affects the character of the three lowest excited states. In particular there is a low-lying CT state present for the folded geometry, which is absent for the unfolded one. (ii) All excitations are either localised on *G*, *BP*, or both (for the CT state, as is evident from Fig. 3.5. The sugar and phosphate groups linking these two subunits do not play a role and can therefore be safely omitted from the QM part in the subsequent QM/MM studies of the system in solvent environments. (iii) A CT state in **1T** cannot be observed, neither in the unfolded nor in the folded geometry.

3.2.2 MD simulations of 1G and 1T

To investigate the behaviour of **1G** and **1T** in the solvents water and methanol as well as to generate proper starting structures for a subsequent QM/MM treatment of **1G**, classical molecular dynamics (MD) simulations were carried out. MD simulations in water and methanol were performed by starting from either the folded or the unfolded structures of the isolated molecules. This leads to four MD simulations for **1G** and four for **1T**.

In contrast to the investigations of RoF, the MM simulations are based on the AMBER force field.[129] In order to get the needed charges for the molecule, a restrained electrostatic potential (RESP) fit on top of a HF gas phase calculation in the 6-31G* basis[41] was carried out. The folded GS reference structures of **1G** and **1T** were used (obtained through gas phase calculations with CC2, *vide infra*) The appropriate parameter were created by using the GAFF parameter set,[40] valid for standard chemical molecules and usable with the AMBER force field. The atom types were assigned with AMBER-tools[130] implemented in the AMBER program package. The lists of force field parameters are given in the appendix (see Fig. A.2, Table A.4, Table A.5 and Table A.6). The parameters for the two solvents investigated in this work, i.e. water (TIP3P model was used) and methanol, are also available in the AMBER force field.

For solvation of the unfolded and the folded geometries of **1G** and **1T**, rectangular boxes of size 54x48x48 $Å^3$ (folded case) and 54x58x55 $Å^3$ (unfolded case), were used. These boxes contain 3146 (folded) and 4583 (unfolded) TIP3P water molecules and 1408 (folded) and 2009 (unfolded) MeOH molecules, respectively. The whole MD simulation procedure was done according to the general recommendations. Therefore the initial structures were minimised in two steps. The first step only considered the minimisation of the solvent. Therefore a restraint of 500 $kcalmol^{-1}Å^{-2}$ for the solute was chosen. As second step the whole system was minimised. For both minimisation 10000 steps were applied, starting with the steepest descent algorithm[131] for the first 5000 steps and switching thereafter to the conjugate gradient algorithm[132] for the remaining 5000 steps. The so minimised solvated structure was used for the classical MD investigation, which began with

a 20 *ps* constant volume MD simulation (canonical ensemble), where the temperature was increased from 0 to 300 *K*. During this procedure, a small restraint of 10 $kcalmol^{-1}$Å^{-2} was adopted to the solute. The Langevin thermostat[133,134] with a collusion frequency γ=10 ps^{-1} (propagated by a simple Leapfrog integrator[135]) was chosen. The simulation was continued by taking the last configuration and performing unrestrained constant pressure (1 *atm*) MD with periodic boundary conditions and Langevin thermostat for 100 *ps* to equilibrate the system at 300 *K*. Finally the simulation was continued under the same conditions for 10 *ns* to gather the data for the subsequent analysis. For the whole procedure the SHAKE algorithm[105] and a cutoff of 8 Å was used.

The gained trajectories of **1G** are shown in Fig. 3.6(a) for methanol (starting from the folded geometry) and in Fig. 3.6(b) for water (starting from the unfolded geometry). The trajectories of the two other MD simulations with converse starting geometries are displayed in Fig. 3.7(a) for methanol (starting from the unfolded geometry) and Fig. 3.7(b) for water (starting from the folded geometry).

It turns out that the resulting trajectories are rather independent of the starting geometry: **1G** solvated in water primarily exists in the folded form, while **1G** solvated in methanol primarily exists in the unfolded form. The degree of folding for **1G** is measured by the distances d(C6-C37) and d(C6-O39), which reflect the spatial separation of the *BP* and *G* subunits and were used before (see Fig. 3.2). In the gas phase structures these distances amount to about 5-6 Å for the folded, and 15 Å for the unfolded form. Thus, one can consider geometries with distances above 10 Å as unfolded, which is also depicted in the trajectories with a grey shaded area, and geometries below that as unfolded forms. From Fig. 3.6 one can see that the starting structures of the MD run (folded in methanol and unfolded in water) change during the simulation and stay most of the time in the unfolded geometry (MeOH) respectively in the folded geometry (water). Obviously, the two hydrophobic ring systems *BP* and *G* stick together and undergo π-stacking in the polar water solvent. In the less polar methanol, the two ring systems are solvated individually by the solvent molecules, especially in Fig. 3.7(a), this is quite clear. However, there are some regions, in which the molecules in the methanol

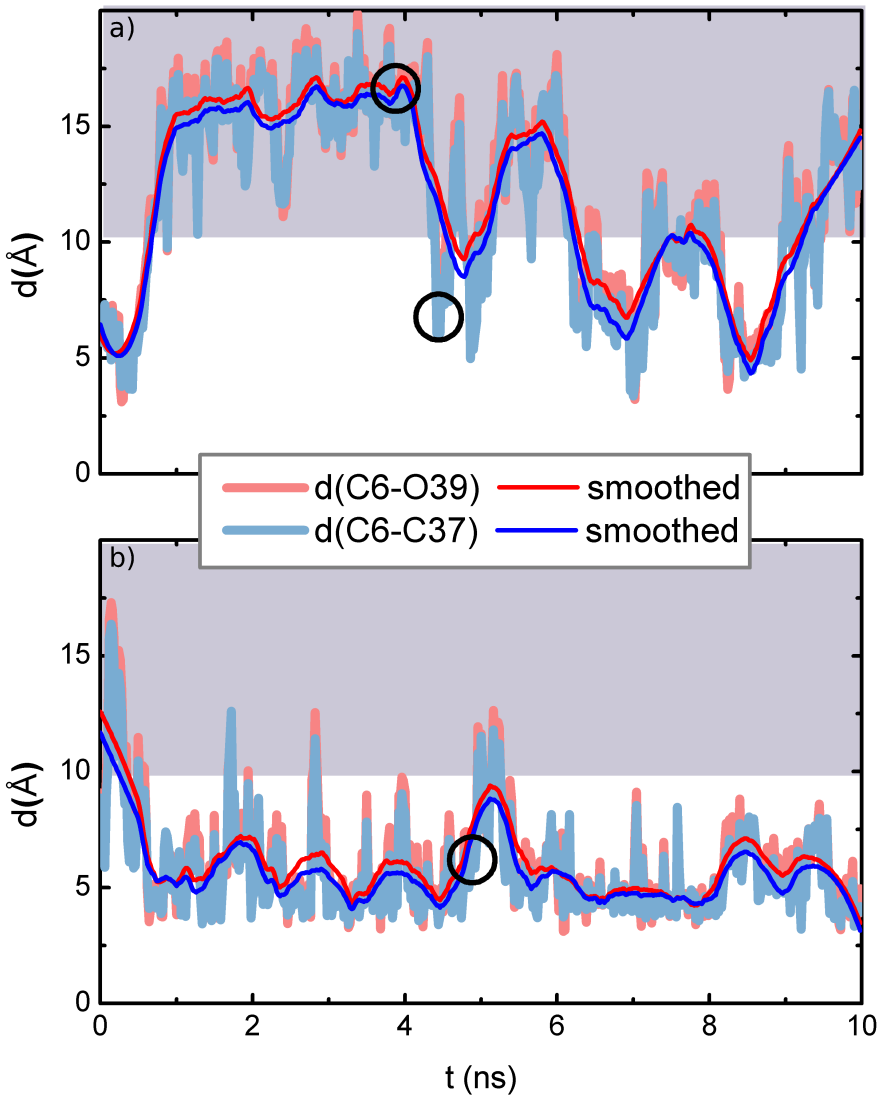

Figure 3.6: Trajectories of MD simulation; (a) **1G** in methanol environment and (b) **1G** solvated in water; the distances d(C6-C37) and d(C6-O39) in Å are plotted against the simulation time in ns. The grey area is the region, in which the molecule is unfolded. The cycles depict the chosen snapshots. (a) MD of **1G** MeOH, folded (4.2 ns; $\mathbf{1G}^{\mathrm{C}}_{\mathrm{MeOH}}$) and unfolded (4.0 ns; $\mathbf{1G}^{\mathrm{A}}_{\mathrm{MeOH}}$) starting geometry (b) MD of **1G** water, folded (4.5 ns; $\mathbf{1G}^{\mathrm{A}}_{\mathrm{H_2O}}$) starting geometry.

environment represent a folded form.

The gained trajectories of **1T** are shown in Fig. 3.8(a) for methanol (starting from

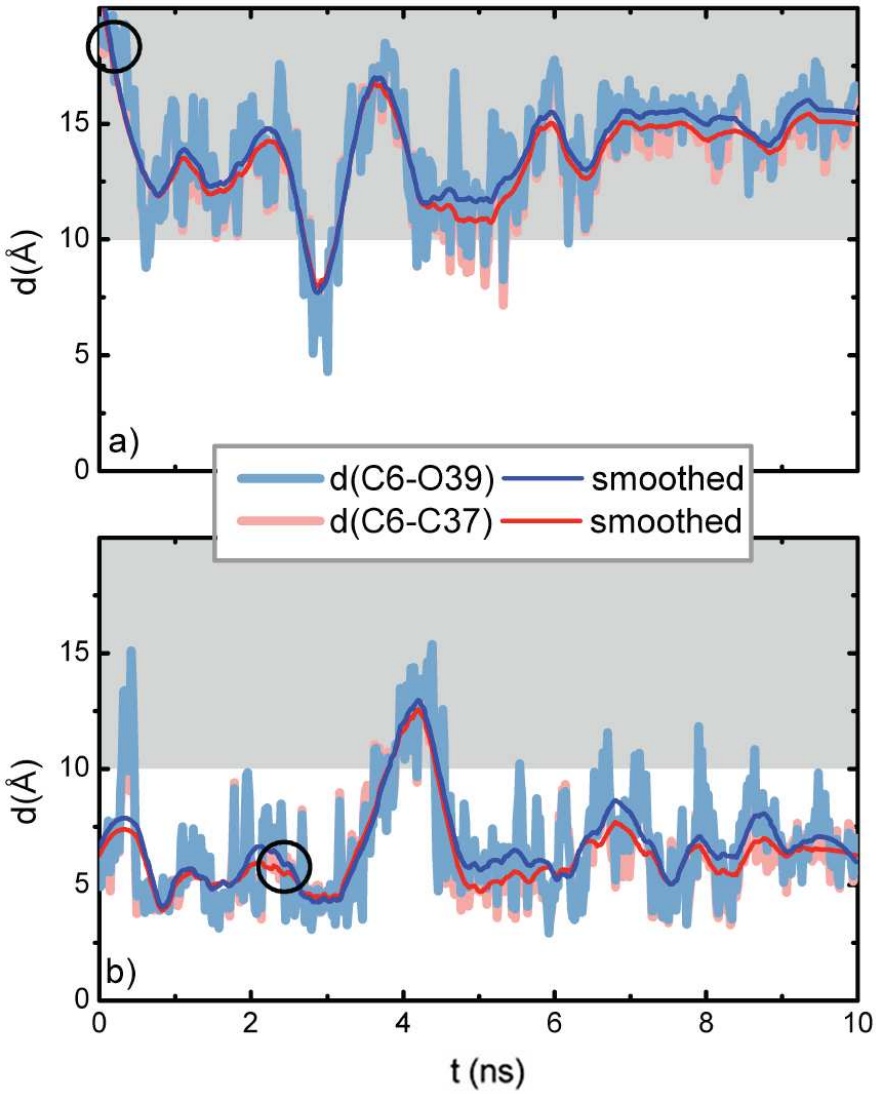

Figure 3.7: Trajectories of MD run; (a) shows **1G** in methanol environment and (b) **1G** in water; the distances d(C6-C37) and d(C6-O39) in Å are plotted against the simulation time in ns. The grey area is the region, in which the molecule is unfolded. The cycles depict the chosen snapshots. (a) MD of **1G** MeOH, unfolded (0.2 ns; $\mathbf{1G}^{\mathrm{B}}_{\mathrm{MeOH}}$) starting geometry (b) MD of **1G** water, folded (2.4 ns; $\mathbf{1G}^{\mathrm{A}}_{\mathrm{H_2O}}$) starting geometry.

the folded geometry) and Fig. 3.8(b) for water (starting from the unfolded geometry). The trajectories of the two other MD simulations with converse starting geometries are displayed in Fig. 3.9(a) for methanol (starting from the unfolded

geometry) and Fig. 3.9(b) for water (starting from the folded geometry).

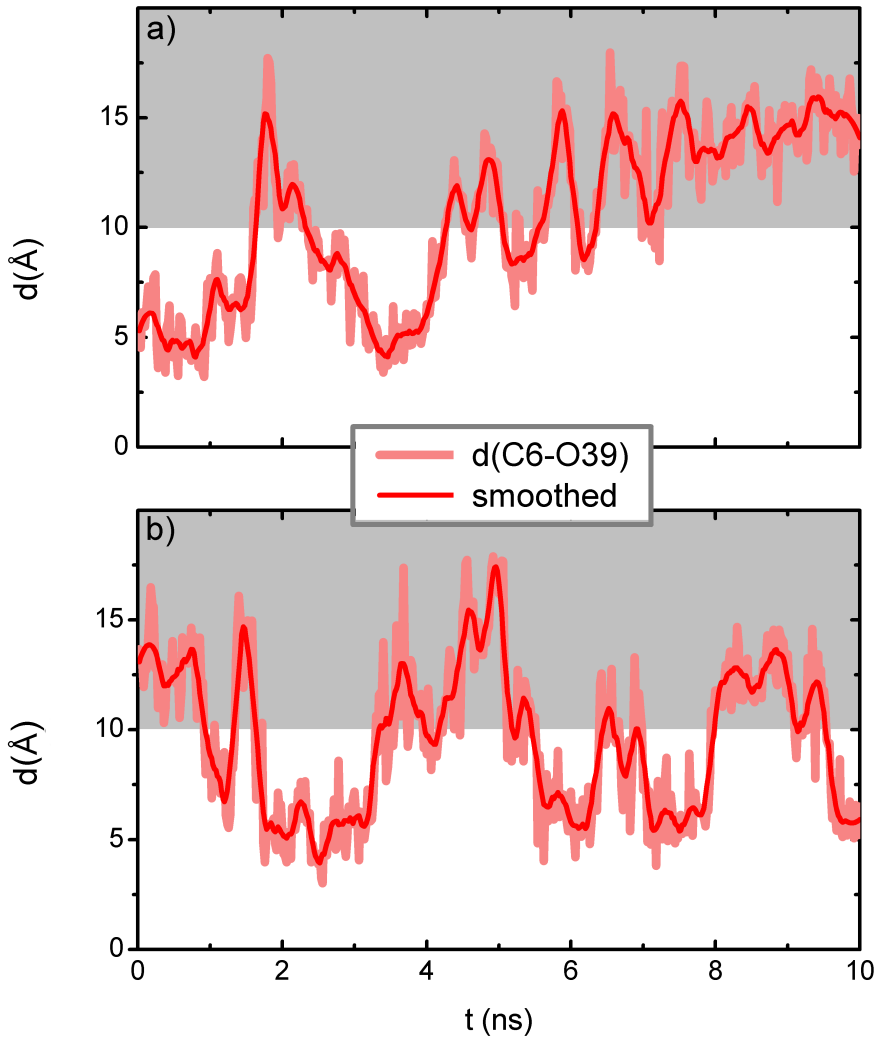

Figure 3.8: Trajectories of MD run; (a) shows **1T** in methanol environment and folded starting geometry (b) **1T** in water with unfolded staring geometry; the distance d(C6-O39) in Å are plotted against the simulation time in ns. The grey area is the region, in which the molecule is unfolded.

In general, the results are comparable to **1G**. **1T** in water is most of the time folded, whereas it is unfolded in methanol. However, the system is a bit more flexible. The degree of the folding of **1T** is measured only by the distance d(C6-O39), which is sufficient to show the separation of the two subunits *BP* and *T*

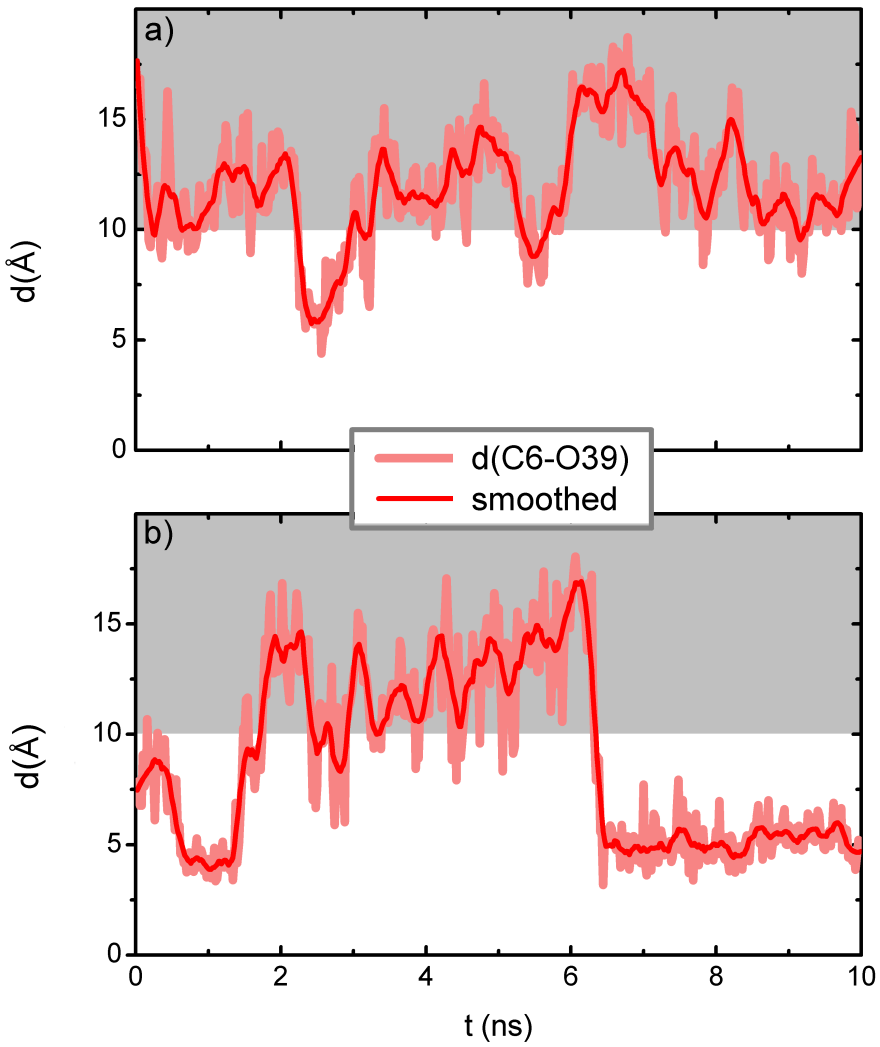

Figure 3.9: Trajectories of MD run; (a) shows **1T** in methanol environment and unfolded starting geometry (b) **1T** in water with folded staring geometry; the distance d(C6-O39) in Å are plotted against the simulation time in ns. The grey area is the region, in which the molecule is unfolded.

(see Fig. 3.2). In the gas phase structures, similar to **1G**, the same criteria for the spatial separation can be used. So, distances above 10 Å also belong to unfolded forms. One can see, that the π-stacking between the *BP* and *T* is not that pronounced, compared to **1G**. This is not that surprising due to the fact that the purines are much more hydrophobic than the pyrimidines. In the less

polar methanol solvent, *BP* and *T* undergo almost no π-stacking and can mostly be found as unfolded molecules during the simulation time.

One can conclude from these results that, independent of the DNA subunit of the dinucleotides **1G** or **1T**, the two different molecules predominately exist in the folded form in water and solvated in methanol, they primarily exist in unfolded form. Though, one can observe the folded form in methanol.

3.2.3 1G in water and methanol - a QM/MM study

Due to the results of the MD simulations, to the fact that there is no CT state in **1T** (see Section 3.2.1) and, which is most important, to the observation of the additional decay channel apart form ISC by spectroscopy in both solvents, five representative snapshots for a subsequent QM/MM study were selected from the trajectories of **1G**. These are indicated in Fig. 3.6 and Fig. 3.7 with black cycles. Two snapshots related to the water environment, $\mathbf{1G}^{\mathrm{A}}_{\mathrm{H_2O}}$ and $\mathbf{1G}^{\mathrm{B}}_{\mathrm{H_2O}}$, which correspond to a folded form and two related to a unfolded from in the methanol environment, $\mathbf{1G}^{\mathrm{A}}_{\mathrm{MeOH}}$, and $\mathbf{1G}^{\mathrm{B}}_{\mathrm{MeOH}}$. Additionally, a folded geometry in the methanol environment was taken, to represent the rather rare event of a folded form in the methanol environment ($\mathbf{1G}^{\mathrm{C}}_{\mathrm{MeOH}}$).

For the QM/MM calculations, the molecule was divided in two subunits. The benzophenone (*BP*), acting as electron acceptor, and the guanidine (*G*), the electron donor, were treated at the MM level. For the linking sugar and the phosphate group the MM level was sufficient (*cf.* discussion in Section 3.2.1). This is also schematically depicted in Fig. 3.2. The electrostatic interaction of the MM with the QM part was described by including all MM point charges in the one electron part of the QM Hamiltonian. For the separation of the MM from the QM part the link-atom approach and the charge shift scheme were employed. For the QM/MM calculations the ChemShell interface was used. Once again, the DL-POLY molecular dynamics module was used for the MM part. The DL-FIND[136] optimiser, also integrated in ChemShell, was driving the QM/MM geometry optimisations.

On the QM side, geometry optimisations for the FC-point were performed with

DFT (B3LYP functional). In order to get a better description of the poorly described long-range van-der-Waals dispersion in DFT/B3LYP, Grimme's dispersion correction was added, as already discussed (*vide supra*). The optimisations of the excited state structures were performed using TD-DFT and the BHLYP functional. The def-SVP basis set was used for all geometry optimisations. Excitation energies and corresponding properties were obtained by TD-CC2 single point calculations upon the optimised (TD)-DFT structures with aug-cc-pVDZ basis set. The RI approximation with standard auxiliary basis set was utilised.

It is convenient, to divide the discussion of the QM/MM results into two parts. The first one focuses on **1G** solvated in water with the two chosen snap shots $\mathbf{1G}^{\mathrm{A}}_{\mathrm{H_2O}}$ and $\mathbf{1G}^{\mathrm{B}}_{\mathrm{H_2O}}$. The second one concentrates on **1G** solvated in methanol with the three snap shots $\mathbf{1G}^{\mathrm{A}}_{\mathrm{MeOH}}$, $\mathbf{1G}^{\mathrm{B}}_{\mathrm{MeOH}}$ and $\mathbf{1G}^{\mathrm{C}}_{\mathrm{MeOH}}$, respectively.

Because the MD simulations showed that **1G** in water almost exclusively exists in folded form, this situation is represented by the two snap shots $\mathbf{1G}^{\mathrm{A}}_{\mathrm{H_2O}}$, and $\mathbf{1G}^{\mathrm{B}}_{\mathrm{H_2O}}$. Excitation energies for the optimised geometries (at FC-point, optimised $(n\pi^*)$ state $(n\pi^*)_{opt}$ and optimised CT state CT_{opt})of $\mathbf{1G}^{\mathrm{A}}_{\mathrm{H_2O}}$ and $\mathbf{1G}^{\mathrm{B}}_{\mathrm{H_2O}}$ are compiled in Table 3.2. The results of the QM/MM single point calculations with TD-CC2/AMBER and aug-cc-pVDZ basis will be discussed in the following.

The optimised ground state geometries of these two folded snapshots feature a distance between C7 and O39 of about 3.3 Å . As is evident from Table 3.2, the excitation energies of the three lowest excited states are very similar for both obtained geometries. For both snap shots the S_1, S_2 and S_3 states are of $(n\pi^*)$, $(\pi\pi^*)$ and $(\pi\pi^*)$ type. In contrast to the results of the isolated molecule, there is no low-lying CT state in the FC region for folded **1G** in water. Apparently, the solvent shell relaxed for the ground state destabilises the CT state. Presumably, the *BP* subunit is primary responsible for this effect (*BP* is not soluble in water). The density difference plots and dipole differences (relative to the ground state) corresponding to $\mathbf{1G}^{\mathrm{A}}_{\mathrm{H_2O}}$ are displayed in Fig. 3.10, which are quite similar to those of $\mathbf{1G}^{\mathrm{B}}_{\mathrm{H_2O}}$ (not displayed).

However, the density difference of the S_1 state for both snap shots looks similar to that of the S_1 state of the isolated system (Fig. 3.5(a)). It has also the character

Table 3.2: TD-CC2/AMBER QM/MM excitation energies ω at the respective TD-DFT minima, calculated in aug-cc-pVDZ basis. ΔE corresponds to the total energy difference of the optimised ($n\pi^*$) state (($n\pi^*)_{opt}$) and the ($n\pi^*$) state at the Frank Condon point geometry ([a] $\Delta E = E_{tot}(n\pi^*)_{opt} - E_{tot}(n\pi^*)_{FC}$) or of the optimised CT state and the ($n\pi^*$) state at the FC-point ([b] $\Delta E = E_{tot}(CT)_{opt} - E_{tot}(n\pi^*)_{FC}$); solvent H_2O.

structure	state	FC-point		$(n\pi^*)_{opt}$		CT_{opt}		ΔE [eV]
		type	ω [eV]	type	ω [eV]	type	ω [eV]	
$\mathbf{1G}^{A}_{H_2O}$	S_1	($n\pi^*$)	3.85	($n\pi^*$)	3.02	CT	2.83	-0.08[a]
	S_2	($\pi\pi^*$)	4.62	($\pi\pi^*$)	4.57	($n\pi^*$)	3.38	
	S_3	($\pi\pi^*$)	4.75	($\pi\pi^*$)	4.71	($\pi\pi^*$)	4.18	-0.36[b]
	S_4	-	-	CT	4.74	-	-	
$\mathbf{1G}^{B}_{H_2O}$	S_1	($n\pi^*$)	3.8	($n\pi^*$)	3.12	CT	2.58	-0.18[a]
	S_2	($\pi\pi^*$)	4.57	($\pi\pi^*$)	4.51	($n\pi^*$)	3.34	
	S_3	($\pi\pi^*$)	4.61	($\pi\pi^*$)	4.57	($\pi\pi^*$)	4.14	-0.2[b]
	S_4	-	-	CT	4.76	-	-	

of a ($n\pi^*$) transition with a dipole moment difference of about 1.9 D, which is comparable to the S_1 state of the isolated system ($\Delta\mu$=1.72 D). The $S_0 \rightarrow S_1$ excitation energies of the two snap shots amount to 330 nm, which fits the experimental value of 329 nm quite well. Relative to the gas phase values, they appear to be blue shifted by 10-20 nm. The S_2 and S_3 states can be considered as ($\pi\pi^*$) states with dipole differences of about 2 D and are quite well separated from S_1. The gap between S_2, and S_3 is very small ($\approx$0.1 eV).

To check, if a CT state occurs on the route downhill to the S_1 state minimum, the ($n\pi^*$) state was optimised. The above mentioned distance of d(C7-O39) does not alter much compared to the FC-point during this optimisation. The energy of the optimised state drops slightly by 0.1 eV for $\mathbf{1G}^{A}_{H_2O}$ and 0.2 eV for $\mathbf{1G}^{B}_{H_2O}$. The characters of the S_1, S_2 and S_3 states at the optimised ($n\pi^*$) state geometry can be considered as ($n\pi^*$), ($\pi\pi^*$), and ($\pi\pi^*$) type, respectively. But a CT state is now found as S_4, looking quite similar as in the isolated molecule (see Fig. 3.5(c)).

The optimisation of this CT state followed. The relevant density difference plots

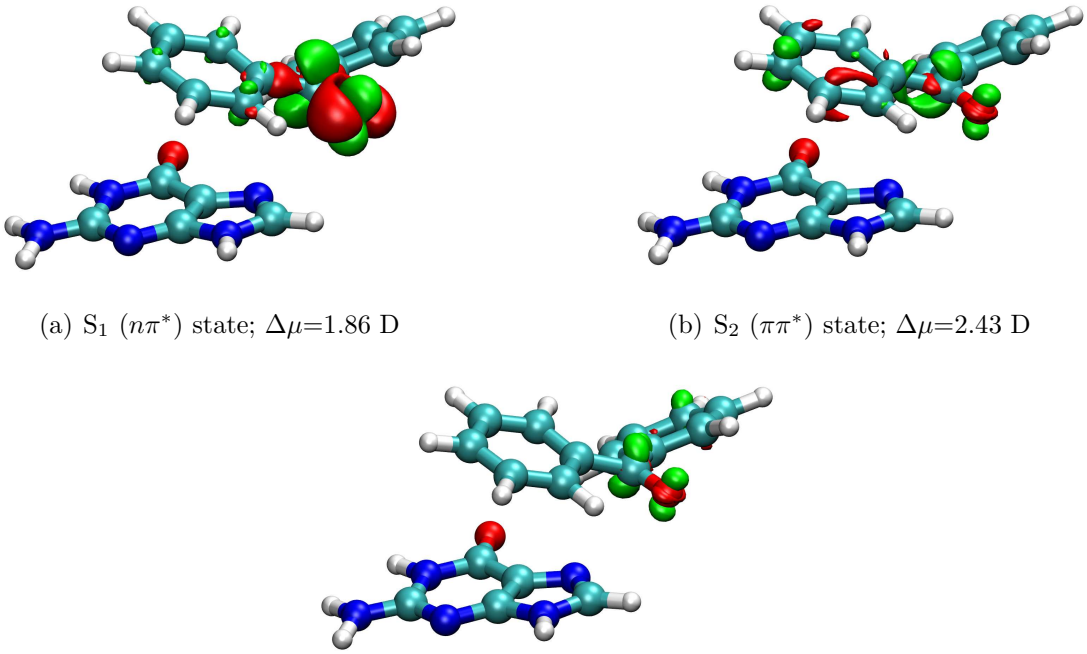

(a) S_1 ($n\pi^*$) state; $\Delta\mu$=1.86 D

(b) S_2 ($\pi\pi^*$) state; $\Delta\mu$=2.43 D

(c) S_3 ($\pi\pi^*$) state; $\Delta\mu$=2.46 D

Figure 3.10: Electron density difference plots for the first three excited singlet states of $\mathbf{1G}^{\mathrm{A}}_{\mathrm{H_2O}}$, calculated with TD-CC2/AMBER in aug-cc-pVDZ basis in the QM/MM framework at the Franck Condon point. Isosurfaces are plotted for ±0.005 a.u., red refers to a decrease, green to an increase in the density upon excitation.

and dipole moment differences related to $\mathbf{1G}^{\mathrm{A}}_{\mathrm{H_2O}}$ (values and electron density difference plots of $\mathbf{1G}^{\mathrm{B}}_{\mathrm{H_2O}}$ are once again quite similar and not shown) are given in Fig. 3.11.

The CT minimum for both snap shots is below the energy of the S_1 at the FC-point (cf. Table 3.2 ΔE=0.36 eV and ΔE=0.2 eV), hence at about the same energy as compared to the S_1 state minimum ($\mathbf{1G}^{\mathrm{B}}_{\mathrm{H_2O}}$), or slightly below ($\mathbf{1G}^{\mathrm{A}}_{\mathrm{H_2O}}$). This allows population transfer from the excited S_1 state to the dark CT state with reasonable efficiency. The CT state (S_1) features a dipole moment difference of about ≈16 D, which is larger than the comparable CT state of the solvated molecule (*vide supra*). The S_2 corresponds to a ($n\pi^*$) state and the S_3 to a ($\pi\pi^*$) state on the *G* subunit with a relatively large dipole moment difference (relative

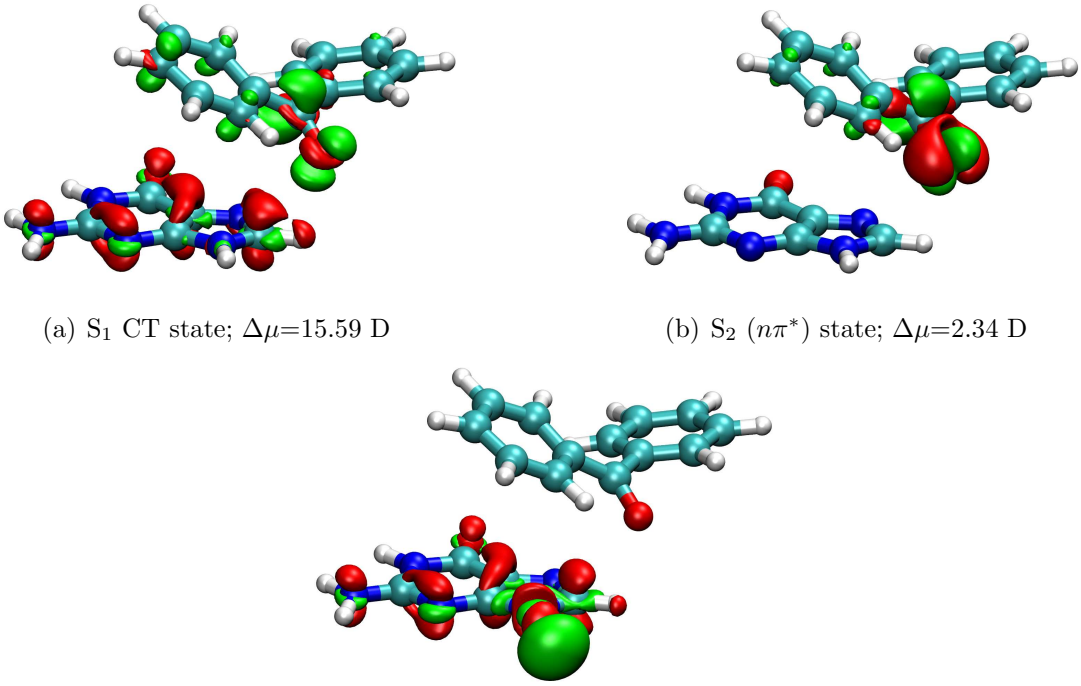

(a) S_1 CT state; $\Delta\mu$=15.59 D

(b) S_2 ($n\pi^*$) state; $\Delta\mu$=2.34 D

(c) S_3 ($\pi\pi^*$) state; $\Delta\mu$=14.24 D

Figure 3.11: Electron density difference plots for the first three excited singlet states of $\mathbf{1G}^{\mathrm{A}}_{\mathrm{H_2O}}$, calculated with TD-CC2/AMBER in aug-cc-pVDZ basis in the QM/MM framework, at the TD-DFT/ BHLYP CT minimum. Isosurfaces are plotted for ±0.005 a.u., red refers to a decrease, green to an increase in the density upon excitation.

to the ground state at that geometry) of more than 10 D. During the optimisation on the CT-PES the distance between oxygen O39 of the *BP* carbonyl group and C7 atom of the *G* subunit decreases substantially from 3.22 Å (FC-point) to 2.73 Å ($\mathbf{1G}^{\mathrm{A}}_{\mathrm{H_2O}}$) and from 3.39 Å (FC-point) to 2.93 Å ($\mathbf{1G}^{\mathrm{B}}_{\mathrm{H_2O}}$) for the optimised CT state. This might indicate a subsequent proton transfer, equalising the charge separation induced by the preceding electron transfer (*cf.* Fig. 3.11). Additionally, the solvent shell around *BP* changes considerably when optimising the geometry on the PES of the CT state, due to the fact that the *BP* subunit now gets polarised by the charge separation.

Lets have a look at the results for the QM/MM investigation of the three individual snap shots from the MD trajectory in methanol for **1G**. As already discussed, **1G**

exists in the methanol environment predominantly in the unfolded conformation. Due to the fact that one can also observe folded configurations in the methanol environment, also one folded snap shot is considered. $\mathbf{1G}^{\mathrm{A}}_{\mathrm{MeOH}}$, and $\mathbf{1G}^{\mathrm{B}}_{\mathrm{MeOH}}$ represent the characteristic unfolded conformation whereas $\mathbf{1G}^{\mathrm{C}}_{\mathrm{MeOH}}$ corresponds to a folded one. This folded conformer was taken into account to check, whether such a geometry provides a CT state or not. The excitation energies of the three lowest excited states obtained by the QM/MM calculations are compiled in Table 3.3.

Table 3.3: TD-CC2/AMBER QM/MM excitation energies ω at the respective TD-DFT minima, calculated in aug-cc-pVDZ basis. ΔE corresponds to the total energy difference of the optimised CT state (CT_{opt}) and the ($n\pi^*$) state at the FC-point ($\Delta\mathrm{E}=\mathrm{E}_{tot}(\mathrm{CT})_{opt}-\mathrm{E}_{tot}(n\pi^*)_{FC}$); solvent methanol.

structure	state	FC-point		$(n\pi^*)_{opt}$		CT_{opt}		ΔE[eV]
		type	ω [eV]	type	ω [eV]	type	ω [eV]	
	S_1	($n\pi^*$)	3.78	($n\pi^*$)	3.15	-		-
$\mathbf{1G}^{\mathrm{A}}_{\mathrm{MeOH}}$	S_2	($\pi\pi^*$)	4.7	($\pi\pi^*$)	4.66			
	S_3	($\pi\pi^*$)	4.82	($\pi\pi^*$)	4.71			
	S_1	($n\pi^*$)	3.84	($n\pi^*$)	3.13	-		-
$\mathbf{1G}^{\mathrm{B}}_{\mathrm{MeOH}}$	S_2	($\pi\pi^*$)	4.58	($\pi\pi^*$)	4.43			
	S_3	($\pi\pi^*$)	4.65	($\pi\pi^*$)	4.61			
	S_1	($n\pi^*$)	3.96	-		CT	2.28	-0.84
$\mathbf{1G}^{\mathrm{C}}_{\mathrm{MeOH}}$	S_2	CT	4.28			($n\pi^*$)	3.48	
	S_3	($\pi\pi^*$)	4.61			($\pi\pi^*$)	3.75	

Optimisations on the S_0 PES yielded distances of d(C7-O39) of 14 and 17 Å for the unfolded geometries ($\mathbf{1G}^{\mathrm{A}}_{\mathrm{MeOH}}$, and $\mathbf{1G}^{\mathrm{B}}_{\mathrm{MeOH}}$), respectively. Compared to the isolated molecule these distances are quite similar. For the folded structure ($\mathbf{1G}^{\mathrm{C}}_{\mathrm{MeOH}}$) the distance amounts to 3.1 Å, which is also similar to the previous observed distances in the water environment.

Calculation of excitation energies for both of the unfolded snap shots ($\mathbf{1G}^{\mathrm{A}}_{\mathrm{MeOH}}$, and $\mathbf{1G}^{\mathrm{B}}_{\mathrm{MeOH}}$) yielded comparable results. The S_1 state corresponds to a ($n\pi^*$) state with excitation energies fitting quite well to the experimental value (as in

the water environment). Again, similar to the spectrum in water, the ($n\pi^*$) state is well separated from the S_2 and the S_3 states, which in turn, are rather close together. The S_2 and S_3 states correspond to ($\pi\pi^*$) states, but in contrast to **1G** in the water environment, the S_3 state is a local excitation on *G*, rather than on the *BP* subunit.

For the folded snap shot $\mathbf{1G}^{\mathrm{C}}_{\mathrm{MeOH}}$ the S_1 has also ($n\pi^*$) character with a similar excitation energy compared to the unfolded geometries. Form this one can conclude that the S_1 ($n\pi^*$) state is hardly affected by the different solvent environments and the dynamics of folding and unfolding. The S_2 on the other hand features a CT character for the folded snap shot. In contrast to the water environment and similar to the case of the isolated system a low-lying CT state already appears at the FC-point. It is only 0.32 eV above the S_1 state. Here, in contrast to the water environment, the solvent shell, relaxed for the electronic ground state, also stabilises the CT state (note that *BP* is soluble in MeOH, but not in water). For the S_3 one can find a ($\pi\pi^*$) state localised on the *BP* subunit with a dipole moment difference ($\Delta\mu$) of about 2 D, which is comparable to the excitations of all other snap shots with the same character. The density difference plots and dipole differences related to $\mathbf{1G}^{\mathrm{A}}_{\mathrm{MeOH}}$ (values and density difference plots of $\mathbf{1G}^{\mathrm{B}}_{\mathrm{MeOH}}$ are quite similar to $\mathbf{1G}^{\mathrm{A}}_{\mathrm{MeOH}}$ and therefore not shown) and $\mathbf{1G}^{\mathrm{C}}_{\mathrm{MeOH}}$ are given in Fig. 3.12 and Fig. 3.13, respectively.

As for **1G** in water, geometry optimisations on the S_1 PES were performed. The unfolded geometries do not alter much compared to the optimised GS. The excitation energy of the S_1 state decreases about 0.7 eV, going from the GS to the S_1 minimum. This is also comparable to the situation of **1G** solvated in water. The characters of the three lowest excited states at the S_1 minimum geometry are ($n\pi^*$), ($\pi\pi^*$) and ($\pi\pi^*$), for S_1, S_2 and S_3, respectively. However, the S_3 state now corresponds to a local excitation on the *BP* subunit, rather than on the *G* subunit and no CT state can be observed.

Concentrating on $\mathbf{1G}^{\mathrm{C}}_{\mathrm{MeOH}}$, the situation is entirely different. During the optimisation on the S_1 PES, the character of S_1 switches from ($n\pi^*$) to CT. Optimisation of the ($n\pi^*$) state was not possible at all. The CT state minimum energy geometry

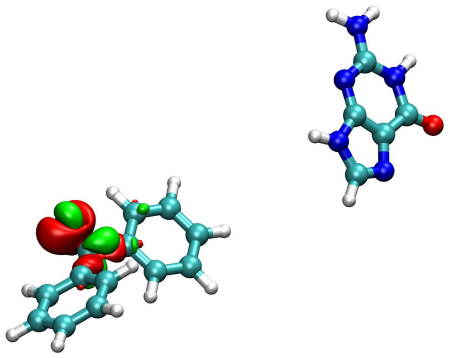

(a) S_1 ($n\pi^*$) state; $\Delta\mu$=1.45 D

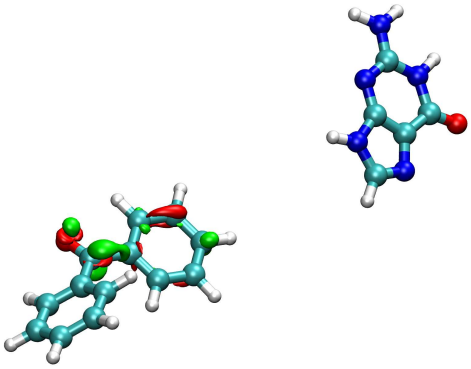

(b) S_2 ($\pi\pi^*$) state; $\Delta\mu$=2.94 D

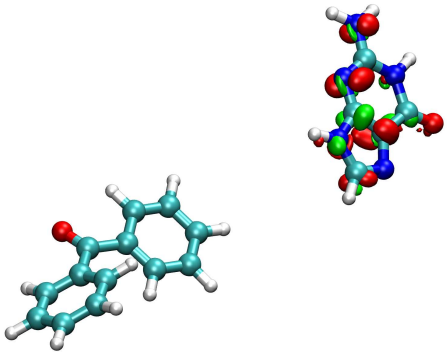

(c) S_3 ($\pi\pi^*$) state; $\Delta\mu$=3.36 D

Figure 3.12: Electron density difference plots for the first three excited singlet states of $\mathbf{1G}^{\mathrm{A}}_{\mathrm{MeOH}}$, calculated with TD-CC2/AMBER in aug-cc-pVDZ basis in the QM/MM framework at the DFT/ B3LYP FC-point. Isosurfaces are plotted for ±0.005 a.u., red refers to a decrease, green to an increase in the density upon excitation.

definitely constitutes the deepest minimum; the total energy drops about 0.8 eV, going from the FC-point to the CT state minimum (cf. Table 3.3). Interestingly, the d(C7-O39) distance decreases significantly from 3.1 to 2.85 Å . The dipole moment difference ($\Delta\mu$) for the CT state amounts to 20 D. The population transfer from the excited ($n\pi^*$) to the CT state thus appears to be rather efficient. The ($n\pi^*$) state for the optimised geometry now appears as S_2 with a similar dipole moment difference ($\Delta\mu$=2.04 D) compared to the FC-point. The S_3 state at the S_1 or CT state minimum corresponds to a local excitation at the *G* subunit with

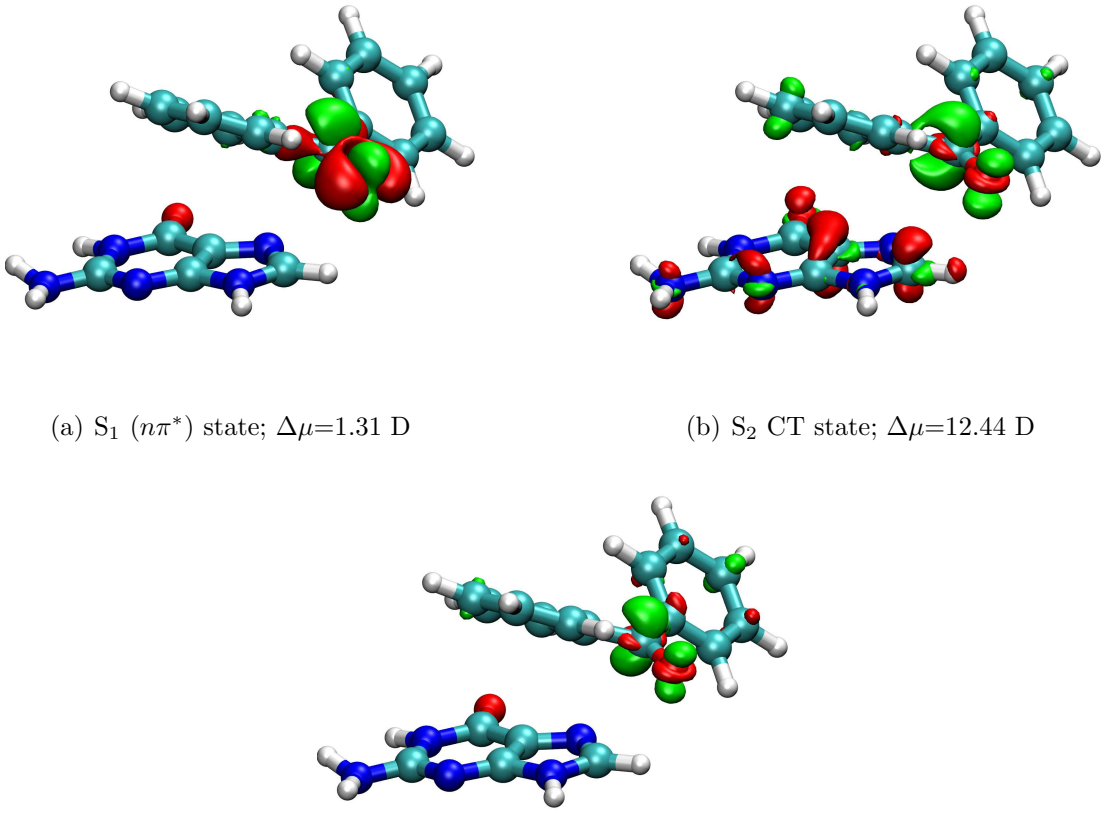

(a) S_1 ($n\pi^*$) state; $\Delta\mu$=1.31 D

(b) S_2 CT state; $\Delta\mu$=12.44 D

(c) S_3 ($\pi\pi^*$) state; $\Delta\mu$=1.96 D

Figure 3.13: Electron density difference plots for the first three excited singlet states of $\mathbf{1G}^{C}_{MeOH}$, calculated with TD-CC2/AMBER in aug-cc-pVDZ basis in the QM/MM framework at the DFT/ B3LYP FC-point. Isosurfaces are plotted for ±0.005 a.u., red refers to a decrease, green to an increase in the density upon excitation.

a ($\pi\pi^*$) character and a very high dipole moment difference of 11.11 D. This is quite similar to the folded snap shots in water environment at the optimised CT state (cf. Fig. 3.11). The density difference plots and dipole moment differences related to the S_1 (CT) state minimum of $\mathbf{1G}^{C}_{MeOH}$ are given in Fig. 3.14.

From the QM/MM results discussed in this section the following conclusions, independent of the solvent environment, can be drawn: (i) For **1G** in its unfolded form no low-lying CT state is found, which could quench the excited ($n\pi^*$) singlet

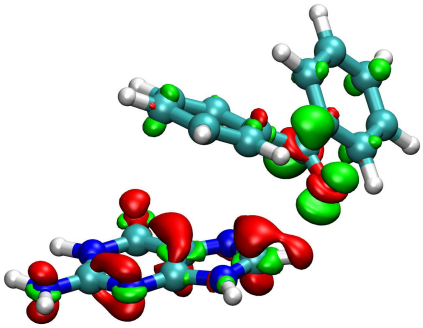

(a) S_1 CT state; $\Delta\mu$=19.75 D

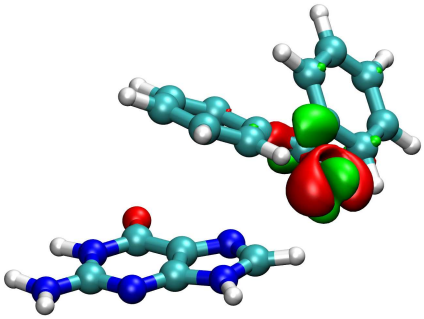

(b) S_2 ($n\pi^*$) state; $\Delta\mu$=2.04 D

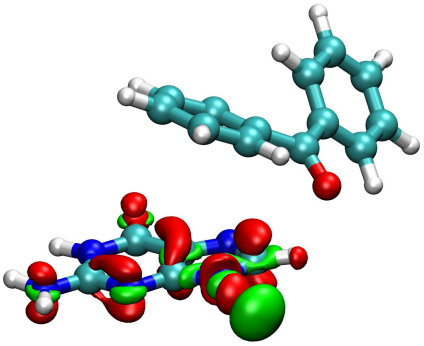

(c) S_3 ($\pi\pi^*$) state; $\Delta\mu$=11.11 D

Figure 3.14: Electron density difference plots for the first three excited singlet states of $\mathbf{1G}^{\mathrm{C}}_{\mathrm{MeOH}}$, calculated with TD-CC2/AMBER in aug-cc-pVDZ basis in the QM/MM framework, at the TD-DFT/ BHLYP CT minimum. Isosurfaces are plotted for ±0.005 a.u., red refers to a decrease, green to an increase in the density upon excitation.

state. Here, the life time of the excited ($n\pi^*$) state is primarily determined by inter-system crossing to the triplet state. (ii) For **1G** in its folded form, on the other hand, indeed a low-lying CT state exists in some regions of the configuration space, which could quench the excited ($n\pi^*$) singlet state. In methanol environment, provided that **1G** adopts the folded form, the transition from the ($n\pi^*$) to the CT state should be more efficient than in the water environment, where the conical intersection apparently does not cross the downhill path from the FC-point to the

S_1 state minimum point. However, in methanol environment **1G** predominantly exists in the unfolded form, hence transition from the $(n\pi^*)$ to the CT state is overall not very frequent. On the other hand, in water, **1G** predominantly exists in the folded form, but the state transition itself is less efficient. Therefore, in both environments quenching of the S_1 state due to population transfer to the dark CT state can occur, but with rather low efficiency. Nevertheless, the calculations predict that the life time of the $(n\pi^*)$ singlet state is not solely governed by ISC.

3.3 Discussion

In this study the photophysics of the benzophenone-substituted dinucleotides **1G** and **1T** have been investigated computationally. The results for isolated molecules of **1G** and **1T** showed that a folded geometry for **1G** is necessary to find a low-lying CT state. For **1T** a CT state cannot be observed, neither in unfolded nor in folded geometry.

The MD simulations showed that **1G** solvated in water predominantly exists in a folded form with the *G* ring system undergoing π-stacking with one of the rings of *BP*. **1G** solvated in methanol, on the other hand, predominantly exists in an unfolded form, with the *G* and *BP* subunits being separated by about 15 Å. For the dinucleotide **1T** a quite similar result can be seen. However, compared to the MD simulations of **1G**, **1T** in water is much more flexible.

Due to the experimental results, extensive hybrid quantum mechanics/molecular mechanics (QM/MM) calculations were carried out for **1G** solvated in methanol and water, with time-dependent coupled cluster (CC2) response theory on the QM side. It is observed that, indeed, a low-lying CT state exists, corresponding to the lowest-lying excited singlet state in some part of the configuration space for the folded form of **1G** solvated in both, water and methanol. No conical intersection seam between the CT and $(n\pi^*)$ state is found in the vicinity of the Franck-Condon point, neither on a path downhill on the potential energy surface towards the $(n\pi^*)$ state minimum. Consequently, for the unfolded **1G** solvated in methanol no decay channel to a CT state exists. This supports also the spectroscopic results

described in Section 3.2 and leads to a conformational control of charge transfer in the studied dinucleotide **1G**.

4 Photochemical decarboxylations

4.1 Introduction

Decarboxylations in chemical reactions are in general the removal of a carboxylic group by the release of carbon dioxide. Literally, it replaces the carboxylic group with a proton. Its one of the oldest organic reactions and needs heat in most protocols using decarboxylations for synthesis.[137] Yet, such decarboxylations are also used by nature using special enzymes, called dehydrogenases, avoiding the use of heat.[138]

Furthermore, it is also possible to make photochemical decarboxylations. Kachkovskyi *et. al.* showed in a recent publication[139] the visible light mediated decarboxylation using **1** (see Fig. 4.1) as the source for carbon centred radicals, which was successfully applied for the synthesis of spirobutenolides.

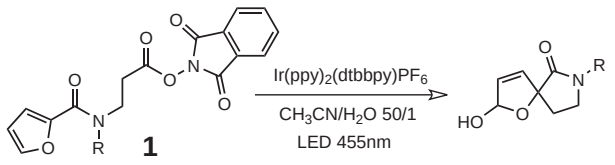

Figure 4.1: Reaction of N-acyloxyphthalamide **1** to a spirobutenolide after excitation and elimination of O-acyl- N-hydroxyphtalimides and CO_2 to the desired product.[139]

For this approach, they used a precursor to generate a reactive radical intermediate. The strategy was based on the usage of O-acyl-N-hydroxyphtalamides, which can undergo a cascade of reductive decomposition accompanied with N-O bond cleavage followed by decarboxylation. The resulting radicals can undergo a cyclization and rearrangement to form the desired product.

During the reaction, they used an iridium catalyst ($Ir(ppy)_2(dtbbpy)PF_6$) as sensitizer with an irradiation of the catalyst at 455 nm. Additionally, the reaction also proceeds without using the sensitizer via direct excitation with UV light.

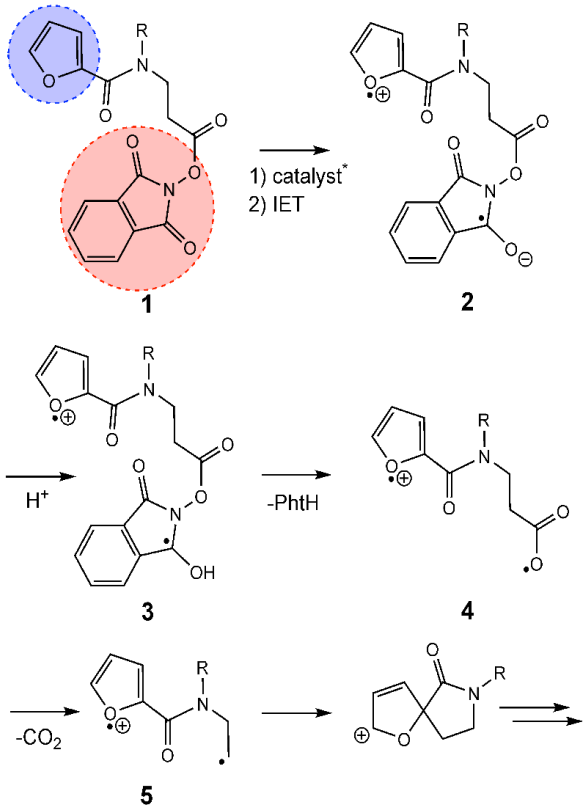

Figure 4.2: Proposed reaction mechanism according to Kachkovskyi *et. al.*[139] Electron donor depicted in blue and electron acceptor (phthalimide - *Pht*) in red.

The proposed mechanism (see Fig. 4.2) is starting with an energy transfer from the excited state of the catalyst to the phthalimide moiety (*Pht*) in **1**. The charge separated intermediate **2** is formed, if the electron donor (furan ring system) and acceptor (*Pht*) of **1** are close to each other. An intramolecular electron transfer (IET) via a CT state takes place. This is a crucial step for good yields in this protocol. After a protonation step at the *Pht* moiety, which leads to **3**, the molecule undergoes a homolytical bond cleavage of the N-O bond between *Pht* and the rest of the molecule and **4** is formed. After decarboxylation generating **5** and radical recombination, a spirocation is formed, which is converted to the desired product

by addition of water and deprotonation.

However, there are still some open questions for a full understanding of the reaction mechanism in every single detail.[139] These questions resulted in a new design for the starting material to study the mechanism more specified. The main idea was to reduce the influence of the special conformation needed for the IET by a new kind of structural design (see Fig. 4.3).

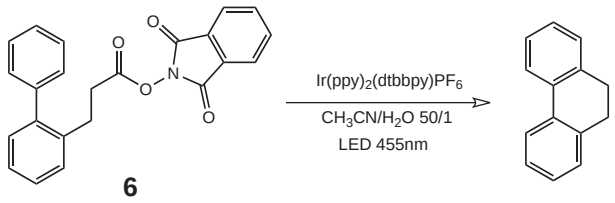

6

Figure 4.3: Synthesis of 9,10-dihydrophenanthrenes via photocatalytic decarboxylation. Red depicts the new formed bond during the reaction.

The new molecule has a more rigid fixation of both, the donor, a biphenyl ring system (*BiP*), and the acceptor (*Pht*). This was expected to provide the desired products to a higher amount and, indeed, this was achieved by using **6** as starting material. However, the proposed general reaction mechanism itself has not changed by replacing the starting material **1** with **6**. The former electron donor (furan ring system) is replaced by *BiP*, from which the electron is transferred to the acceptor *Pht* during the IET.

To understand the proposed reaction mechanism a theoretical study using **6** as starting point was carried out and its results are presented in the next section. Note that for the subsequent steps of the proposed reaction mechanism further theoretical investigations were employed. These preliminary results can be found in Appendix A.3.2.

4.2 Motivation and Results

The main motivation for this study was to understand the proposed reaction mechanism in detail and answer open questions related to it. For the reaction, a

small amount of water is necessary to get a protonated *Pht* otherwise the reaction does not occur at all. Because of this, the first protonation step of the *Pht* moiety has an important role for the IET. It may either take place after the IET, a post-IET according to Okada,[140–143] who proposed this for similar reactions before, or during the IET step itself assuming, proton coupled electron transfer. The two possibilities are shown in Fig. 4.4.

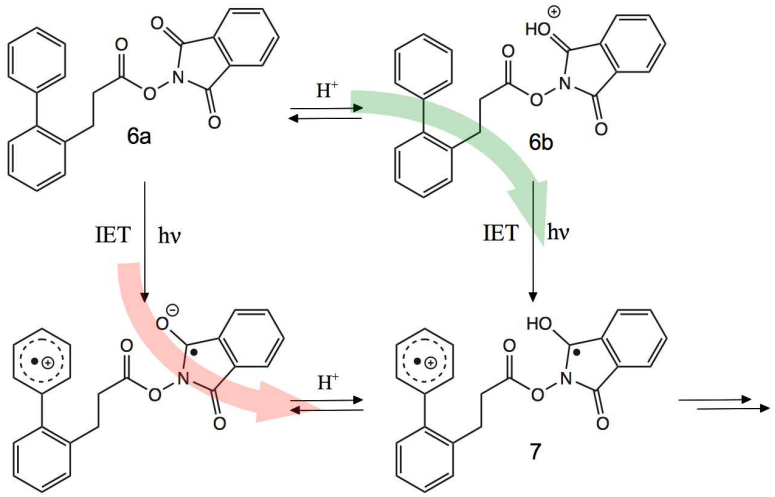

Figure 4.4: Possible pathways for IET: according to Okada (red) and proton coupled electron transfer (green)

In the subsequent theoretical study, this key step was investigated by applying the (TD-)CC2 method with a def2-SVP[144] basis. Throughout this investigation, all QM calculations were done using the TURBOMOLE program package.

As stated before, two possible reaction pathways were investigated, (i) the unprotonated **6a** as starting point for the subsequent IET step (red pathway Fig. 4.4), and (ii) the protonated species **6b** for subsequent proton coupled IET (green pathway in Fig. 4.4). Both possible pathways should finally lead to the charge separated intermediate **7**, which would be comparable to intermediate **3** shown in the proposed reaction mechanism in Fig. 4.2.

To investigate both reaction paths geometry optimisations of **6a** and **6b** in the electronic GS were carried out by employing the CC2 method in the def2-SVP basis. Subsequently, properties of the first four electronically excited singlet and triplet

states of **6a** and **6b** were calculated at their corresponding GS minima employing TD-CC2 linear response theory in the same basis set. Of interest are primarily energetically low lying excited states with distinct CT character, indicating an IET. The resulting excitation energies and the related electron density difference plots for the triplet states are shown in Table 4.1, Fig. 4.5 and Fig. 4.6, respectively, for the four lowest singlet and triplet states (the corresponding electron density difference plots for the singlet states are shown in Fig. A.3 and Fig. A.4, respectively, in the appendix).

Table 4.1: Excitation energies ω in eV, dipole moment changes $\Delta\mu$ relative to the GS in Debye and oscillator strengths in a.u. at the related optimised ground state geometry for **6a** and **6b**, respectively.

structure	state	ω [eV]	type	$\Delta\mu$ [D]	oscillator strength
6a	S_1	4.14	LE ($n\pi^*$)	3.40	0.000
	S_2	4.54	LE ($n\pi^*$)	2.84	0.008
	S_3	4.74	LE ($\pi\pi^*$)	1.19	0.017
	S_4	4.96	LE ($n\pi^*$)	2.46	0.000
	T_1	3.82	LE ($n\pi^*$)	0.56	-
	T_2	3.88	LE ($n\pi^*$)	3.20	-
	T_3	4.09	LE ($\pi\pi^*$)	0.13	-
	T_4	4.30	LE ($n\pi^*$)	0.51	-
6b	S_1	2.62	CT	22.07	0.002
	S_2	3.05	CT	20.75	0.001
	S_3	3.47	CT	25.70	0.000
	S_4	3.57	CT	23.06	0.000
	T_1	2.62	CT	21.92	-
	T_2	3.05	CT	20.19	-
	T_3	3.26	LE ($n\pi^*$)	1.30	-
	T_4	3.45	CT	24.10	-

As is evident from Table 4.1 and Fig. 4.5, for **6a** there is no low-lying singlet or triplet excited state with significant CT character. All excited states correspond to local excitations either on the *Pht* or the *BiP* subunit (LE states). The corre-

sponding dipole moment changes $\Delta\mu$ relative to the GS also have very low values. The S_1, S_2, S_3 and S_4 states are dominated by $(n\pi^*)$, $(n\pi^*)$, $(\pi\pi^*)$, and once again $(n\pi^*)$ singlet excitations, respectively. The oscillator strengths for the $(n\pi^*)$ states are very low, as expected. For the S_3, the local $(\pi\pi^*)$ state, located at the *BiP* subunit, refers to the highest among the first four singlet excitations. The triplet states T_1, T_2, T_3 and T_4 are of the same type as the corresponding singlet states. The $\Delta\mu$ values are quite low as well, which can also be seen in the tiny increase or decrease of the isosurfaces of the electron density difference plots (see Fig. 4.5).

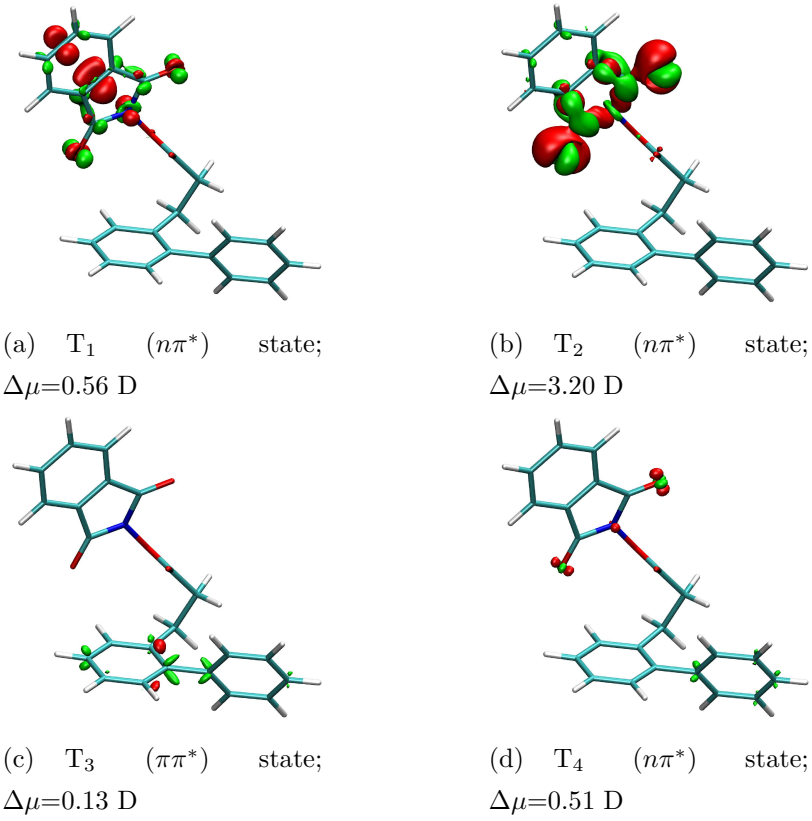

(a) T_1 $(n\pi^*)$ state; $\Delta\mu$=0.56 D

(b) T_2 $(n\pi^*)$ state; $\Delta\mu$=3.20 D

(c) T_3 $(\pi\pi^*)$ state; $\Delta\mu$=0.13 D

(d) T_4 $(n\pi^*)$ state; $\Delta\mu$=0.51 D

Figure 4.5: Electron density difference plots for the first four excited triplet states of **6a**, calculated with TD-CC2 in def2-SVP basis. Isosurfaces are plotted for ±0.004 a.u., red refers to a decrease, green to an increase in the density upon excitation. Additionally, the types and the dipole moment changes $\Delta\mu$ relative to the GS for the corresponding states are given.

A completely different picture emerges for **6b**. Virtually all states have CT char-

acter. The dipole moment changes relative to the GS ($\Delta\mu$) amount to around 20 D and very low oscillator strengths are obtained, which is typical for CT states. For all observed CT states one can see from the electron density difference plots, that the CT of **6b** features depletion of electron density on *BiP* and an increase of electron density on *Pht*, which is consistent with the proposed IET. For the triplet excitations there is one LE state with ($n\pi^*$) state character (T_3), which is comparable to a LE state of **6a** (T_1).

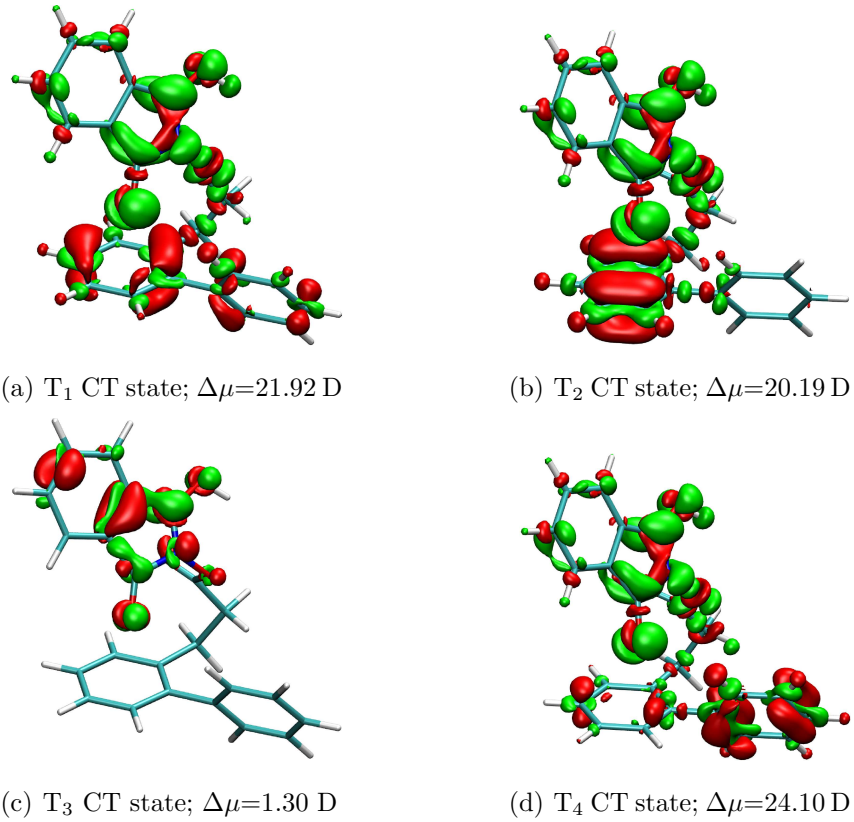

(a) T_1 CT state; $\Delta\mu$=21.92 D

(b) T_2 CT state; $\Delta\mu$=20.19 D

(c) T_3 CT state; $\Delta\mu$=1.30 D

(d) T_4 CT state; $\Delta\mu$=24.10 D

Figure 4.6: Electron density difference plots for the first four excited triplet states of **6b**, calculated with TD-CC2 in def2-SVP basis. Isosurfaces are plotted for ±0.004 a.u., red refers to a decrease, green to an increase in the density upon excitation. Additionally, the types and the dipole moment changes $\Delta\mu$ relative to the GS for the corresponding states are given.

The excitation energies of the singlet and triplet states decrease significantly with respect to those calculated for **6a** and are in the proper range for sensitisation of

the chromophore by the $Ir(ppy)_2(dtbbpy)PF_6$ catalyst.[139] This is a clear indication that the phthalimide moiety has to be protonated before the IET and confirming the proton coupled IET reaction mechanism.

Going on with the general procedure for investigations of such systems described in Chapter 1, it was also attempted to optimise the minimum energy geometry of the S_1 state of **6b** (with TD-CC2/def2-SVP), but this turned out not to be possible since a conical intersection with the ground state was encountered on the path downhill from the FC point. Here, the response theory breaks down. During the optimisation, one can observe that the bond between the *Pht* moiety and the rest of the chromophore increases considerably, which can be seen in Fig. 4.7.

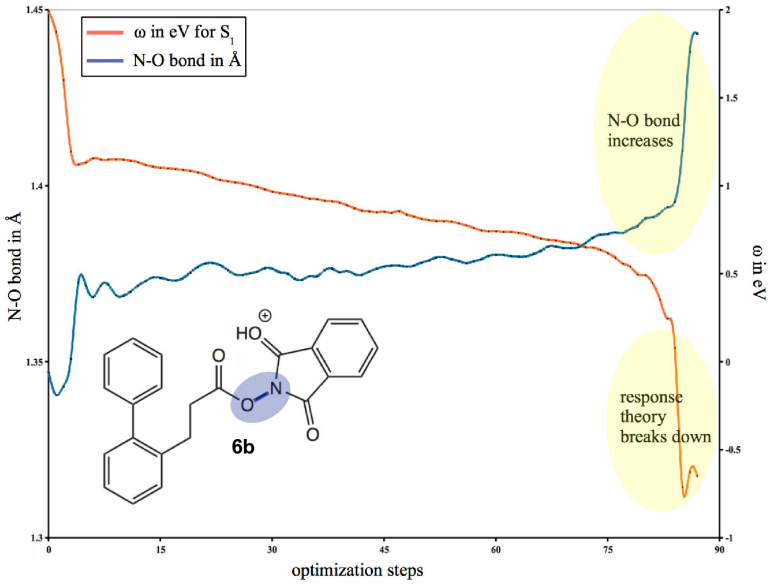

Figure 4.7: N-O bond distance in Å (blue and left y-axis) and corresponding excitation energy (red and right y-axis) plotted against the optimisation steps of TD-CC2/def-2SVP of the first singlet state of **6b**. Yellow areas depict regions, where the response theory breaks down and the N-O bond significantly increases

Optimisation of the T_1 state, on the other hand, was successful. The excitation energies, dipole moment changes relative to the GS, and the corresponding electron density difference plots are displayed in Fig. 4.8. As is evident from, the excitation energy for the T_1 state drops down to 0.96 eV at its minimum energy geometry,

keeping its CT character. At this geometry, the only remaining triplet LE state with ($n\pi^*$) state character now corresponds to T_4, whereas at the FC-point it was T_3. The aforementioned N-O bond connecting the phthalimide moiety with the rest of the chromophore increases from 1.36 Å to 1.39 Å . This may be a hint for the subsequent steps of the proposed reaction mechanism.

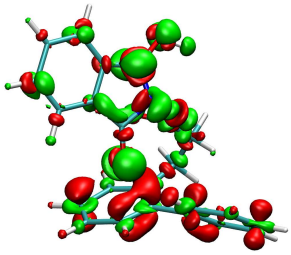

(a) T_1 CT state; ω=0.96 eV; $\Delta\mu$=20.84 D

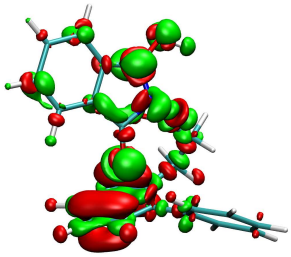

(b) T_2 CT state; ω=1.98 eV; $\Delta\mu$=19.94 D

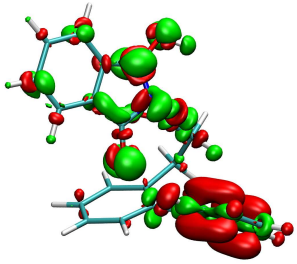

(c) T_3 CT state; ω=2.39 eV; $\Delta\mu$=23.27 D

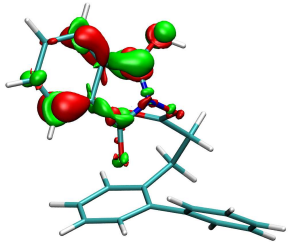

(d) T_4 ($n\pi^*$) state; ω=3.09 eV; $\Delta\mu$=3.21 D

Figure 4.8: Electron density difference plots of the first four excited states for the optimised T_1 state of **6b**, calculated with TD-CC2 in def2-SVP basis. Isosurfaces are plotted for ±0.004 a.u., red refers to a decrease, green to an increase in the density upon excitation. Additionally, the types, excitation energies ω and the dipole moment changes $\Delta\mu$ relative to the GS for the corresponding states are given.

4.3 Discussion

In conclusion, the theoretical results show a clear indication for a proton coupled electron transfer (green pathway Fig. 4.4), since for **6a** a CT state cannot be observed among the energetically low-lying excited states, whereas for **6b** the excitation energy of the first observed CT state is in the range of the sensitizer. The protonation of the starting material by water as the very first step thus, is quite important for the whole reaction. The subsequent steps in the proposed reaction mechanism involve elimination of *Pht*, for which the optimisations of the first singlet and triplet states of **6b** already revealed a significant increase of the N-O bond.

5 Summary

In this work the understanding of questions regarding to photocatalytic reactions were studied using TD-CC2 linear response and quantum mechanics/molecular mechanic (QM/MM) calculations.

The introduction gave a short overview about the concept of potential energy surfaces (PES), the employed theoretical methods on ab initio side and the concept of the combination of these with the molecular mechanic method, the QM/MM scheme. Applicability, weaknesses and limitations of the ab initio methods, (TD)-CC2 and (TD)-DFT, and the QM/MM scheme were discussed, which were used throughout this work. These drawbacks have to be considered adopting the different methods to studies of photochemical systems. Also, the general procedure, which was used for the description of the photophysics in the following examples, is presented therein. In subsequent chapters the application of this general procedure on issues arising from chemical photocatalysis is presented for different concrete examples.

The first project covered the photophysics of roseoflavin. Roseoflavin is a modification of flavin, which, first of all, could be used as photocatalyst in organic photochemical redox reactions and, secondly, could be incorporated as a photoreceptor in the well-known BLUF (blue light using flavin adenine dinucleotide FAD) proteins. Hence, photophysics of roseoflavin in three different environments were investigated by using ab initio, (TD)-CC2 and (TD)-DFT), and quantum mechanics/molecular mechanics methods with the CHARMM force field. On the one hand, intramolecular charge transfer is shown to be responsible for the quenching of the fluorescence in the gas phase, by a so-called ”PICT” mechanism. On the other hand, it was found that the fluorescence is quenched by a ”TICT” mecha-

nism in a water environment. Additionally, roseoflavin was incorporated into a BLUF protein environment, substituting the native flavin. Here, the main focus was the conical intersection between the locally excited state of the chromophore and the charge transfer state involving the tyrosine residue, which is responsible for initiating the photocycle in the native BLUF domain. This conical intersection is missing for the roseoflavin-substituted protein. These results explain the lack of any photocycle and the loss of the biological function of the BLUF photoreceptor in experiments.

The second project focused on the dynamics and electronic structure of dinucleotides. These consist of an artificial DNA nucleoside, in which benzophenone as chromophore is attached to the anomeric centre of 2'-desoxyribofuranoside as base alternative, and the two nucleosides guanosine (**1G**) and thymidine (**1T**), respectively. With ab initio methods ((TD)-CC2 and (TD)-DFT) two geometries, a folded and an unfolded structure were observed for the two dinucleotides in gas phase and the properties for the first four electronically excited singlet states were studied. It was shown that there is a low-lying CT state for the folded **1G**, which is absent for the unfolded one. In contrast to that, such a CT state cannot be observed for **1T** neither in the folded nor in the unfolded geometry. By using molecular dynamics simulations in two solvents, namely methanol and water, utilising the AMBER force field, the predominant conformations were obtained. In MeOH the two dinucleosides adopt mainly an open, unfolded geometry and in water primarily a stacked, folded conformation. However, folded form is observed for both dinucleotides in methanol as well. Since low-lying CT state in **1T** is absent, only for **1G** extensive QM/MM calculations were carried out to investigate a possible photo-induced intramolecular charge transfer in detail. Representative snapshots of the trajectories were taken for both solvents to study the influence of the environment on the singlet excitation. It is found that there is no low-lying CT state for the unfolded form of **1G**. The lifetime of the excited state is therefore primarily determined by inter-system crossing to the triplet state. On the other hand, for **1G** in its folded form, which can be found in both solvent environments, indeed a low-lying CT state exists, which could quench the excited singlet state. Thus the calculations predict, that the lifetime of the first excited singlet state in

both environments is not solely governed by ISC, which is supported by experimental results. So the CT state in the studied dinucleotide **1G** is controlled by its conformation.

In the third and last project presented in this work, a key step of a proposed reaction mechanism for a visible light mediated decarboxylation was studied. By using ab initio calculations employing the (TD)-CC2 linear response method, the first step of two possible reaction pathways was investigated. It may either take place after an intramolecular electron transfer (IET), a post-IET, or before the IET step itself, assuming proton coupled electron transfer. The theoretical results showed a clear indication for a proton coupled electron transfer. The protonation of the starting material by water as the very first step is therefore important for the whole reaction. By following the general procedure presented in the introduction, optimisation of the first triplet excitation for the relevant CT state of the proton coupled electron transfer reveals a significant hint for further steps of the proposed mechanism.

In all projects studied for this work, the general procedure using TD-CC2 linear response or TD-CC2 linear response embedded in the QM/MM scheme for describing photochemical systems in the framework of photocatalysis turns out to be robust and reliable and thus can be used for other investigations considering limitations and weaknesses of it.

6 Bibliography

[1] H. Trommsdorff, Annalen der Pharmacie **11**, 190 (1834).

[2] G. Ciamician, Science **36**, 385 (1912).

[3] B. König, editor, *Chemical Photocatalysis*, De Gruyter, Berlin, Boston, 2013.

[4] M. Born and R. Oppenheimer, Annalen der Physik **389**, 457 (1927).

[5] L. Serrano-Andrés and M. Merchán, Journal of Photochemistry and Photobiology C: Photochemistry Reviews **10**, 21 (2009).

[6] E. Teller, Journal of Chemical Physics **41**, 109 (1937).

[7] L. González, D. Escudero, and L. Serrano-Andrés, Chemphyschem. **13**, 28 (2012).

[8] W. Domcke and C. Woywod, Chemical Physical Letters **216**, 362 (1993).

[9] M. V. Berry and M. Wilkinson, Proceedings of the Royal Society A: Mathematical, Physical and Engineering Sciences **392**, 15 (1984).

[10] B. O. Roos, P. R. Taylor, and P. E. M. Siegbahn, Chemical Physics **48**, 157 (1980).

[11] J. B. Foresman, M. Head-Gordon, J. A. Pople, and M. J. Frisch, Journal of Chemical Physics **96**, 135 (1992).

[12] J. Oddershede, Propagator Methods, in *Advances in Chemical Physics*, pages 201–239, John Wiley & Sons, Inc., 2007.

[13] A. B. Trofimov, I. L. Krivdina, J. Weller, and J. Schirmer, Chemical Physics **329**, 1 (2006).

[14] R. Bartlett and M. Musiał, Reviews of Modern Physics **79**, 291 (2007).

[15] H. Sekino and R. J. Bartlett, International Journal of Quantum Chemistry **26**, 255 (1984).

[16] H. Koch and P. Jørgensen, Journal of Chemical Physics **93**, 3333 (1990).

[17] H. Koch, O. Christiansen, P. Jørgensen, and J. Olsen, Chemical Physical Letters **244**, 75 (1995).

[18] O. Christiansen, H. Koch, and P. Jørgensen, Chemical Physical Letters **243**, 409 (1995).

[19] O. Christiansen, H. Koch, and P. Jørgensen, Journal of Chemical Physics **103**, 7429 (1995).

[20] A. Köhn and A. Tajti, The Journal of Chemical Physics **127**, 044105 (2007).

[21] P. Hohenberg and W. Kohn, Physical Review B **136**, 864 (1964).

[22] A. D. Becke, The Journal of Chemical Physics **98**, 5648 (1993).

[23] M. E. Casida and M. Huix-Rotllant, Annual Review of Physical Chemistry **63**, 287 (2012).

[24] S. Grimme and M. Parac, Chemphyschem. **4**, 292 (2003).

[25] M. Parac and S. Grimme, The Journal of Physical Chemistry A **106**, 6844 (2002).

[26] D. J. Tozer, The Journal of Chemical Physics **119**, 12697 (2003).

[27] A. Dreuw, J. L. Weisman, and M. Head-Gordon, The Journal of Chemical Physics **119**, 2943 (2003).

[28] T. Yanai, D. P. Tew, and N. C. Handy, Chemical Physics Letters **393**, 51 (2004).

[29] M. J. G. Peach, P. Benfield, T. Helgaker, and D. J. Tozer, The Journal of Chemical Physics **128**, 044118 (2008).

[30] L. Kronik, T. Stein, S. Refaely-Abramson, and R. Baer, Journal of Chemical Theory and Computation **8**, 1515 (2012).

[31] A. Warshel and M. Levitt, Journal of Molecular Biology **103**, 227 (1976).

[32] M. J. Field, P. A. Bash, and M. Karplus, Journal of Computational Chemistry **11**, 700 (1990).

[33] A. R. Fersht, Proceedings of the National Academy of Sciences (2013).

[34] G. Groenhof, Angewandte Chemie International Edition **52**, 12489 (2013).

[35] W. L. Jorgensen, J. Chandrasekhar, J. D. Madura, R. W. Impey, and M. L. Klein, Journal of Chemical Physics **79**, 926 (1983).

[36] J. W. Ponder and D. A. Case, Advances in Protein Chemistry **66**, 27 (2003).

[37] D. A. Case et al., Journal of Computational Chemistry **26**, 1668 (2005).

[38] A. D. MacKerell et al., The Journal of Physical Chemistry B **102**, 3586 (1998).

[39] B. R. Brooks et al., Journal of Computational Chemistry **30**, 1545 (2009).

[40] J. Wang, R. M. Wolf, J. W. Caldwell, P. A. Kollman, and D. A. Case, Journal of Computational Chemistry **25**, 1157 (2004).

[41] C. I. Bayly, P. Cieplak, W. Cornell, and P. A. Kollman, Journal of Chemical Physics **97**, 10269 (1993).

[42] N. L. Allinger, R. A. Kok, and M. R. Imam, Journal of Computational Chemistry **9**, 591 (1988).

[43] N. L. Allinger, Y. H. Yuh, and J. H. Lii, Journal of the American Chemical Society **111**, 8551 (1989).

[44] N. L. Allinger, K. Chen, and J.-H. Lii, Journal of Computational Chemistry **17**, 642 (1996).

[45] A. K. Rappe, C. J. Casewit, K. S. Colwell, W. A. Goddard, and W. M. Skiff, Journal of the American Chemical Society **114**, 10024 (1992).

[46] B. Hess, C. Kutzner, D. van der Spoel, and E. Lindahl, Journal of Chemical Theory and Computation **4**, 435 (2008).

[47] T. Schmidt et al., QM/MM Investigations Of Organic Chemistry Oriented Questions, Topics in Current Chemistry, pages 1–77, Springer Berlin / Heidelberg, 2012.

[48] H. Senn and W. Thiel, QM/MM Methods for Biological Systems, in *Atomistic approaches in modern biology*, edited by M. Reiher, volume 268 of *Topics in Current Chemistry*, pages 173–290, Springer Berlin / Heidelberg, 2007.

[49] H. Hu and W. Yang, Journal of Molecular Structure: THEOCHEM **898**, 17 (2009).

[50] O. Acevedo and W. L. Jorgensen, Accounts of Chemical Research **43**, 142 (2010).

[51] K. P. Eurenius, D. C. Chatfield, B. R. Brooks, and M. Hodoscek, International Journal of Quantum Chemistry **60**, 1189 (1996).

[52] J. Gao, P. Amara, C. Alhambra, and M. J. Field, The Journal of Physical Chemistry A **102**, 4714 (1998).

[53] H. M. Senn and W. Thiel, Angewandte Chemie International Edition **48**, 1198 (2009).

[54] L. Hu, P. Söderhjelm, and U. Ryde, Journal of Chemical Theory and Computation **7**, 761 (2011).

[55] D. Bakowies and W. Thiel, The Journal of Physical Chemistry **100**, 10580 (1996).

[56] G. Mills and H. Jónsson, Physical Review Letters **72**, 1124 (1994).

[57] D. Sheppard, R. Terrell, and G. Henkelman, Journal of Chemical Physics **128**, 134106 (2008).

[58] T. Merz, K. Sadeghian, and M. Schütz, Physical Chemistry Chemical Physics **13**, 14775 (2011).

[59] M. Gomelsky and G. Klug, Trends in Biochemical Sciences **27**, 497 (2002).

[60] S. Masuda and C. E. Bauer, Cell **110**, 613 (2002).

[61] W. Laan, M. A. van der Horst, I. H. Van Stokkum, and K. J. Hellingwerf, Photochemistry and Photobiology **78**, 290 (2003).

[62] V. Dragnea, M. Waegele, S. Balascuta, C. Bauer, and B. Dragnea, Biochemistry **44**, 15978 (2005).

[63] S. Masuda, Y. Tomida, H. Ohta, and K. ichiro Takamiya, Journal of Molecular Biology **368**, 1223 (2007).

[64] P. Zirak et al., Chemical Physics **315**, 142 (2005).

[65] M. Gauden et al., Proceedings of the National Academy of Sciences **103**, 10895 (2006).

[66] A. Jung, J. Reinstein, T. Domratcheva, R. L. Shoeman, and I. Schlichting, Journal of Molecular Biology **362**, 717 (2006).

[67] J. T. M. Kennis and T. Mathes, Interface Focus **3** (2013).

[68] P. Zirak et al., Journal of Photochemistry and Photobiology B: Biology **83**, 180 (2006).

[69] A. Jung et al., Proceedings of the National Academy of Sciences **101**, 12306 (2005).

[70] K. Hasegawa, S. Masuda, and T. Ono, Biochemistry **43**, 14979 (2004).

[71] S. Masuda, K. Hasegawa, A. Ishii, and T. Ono, Biochemistry **43**, 5304 (2004).

[72] K. Hasegawa, S. Masuda, and T. Ono, Plant and Cell Physiology **46**, 136 (2005).

[73] P. Zirak, A. Penzkofer, C. Lehmpfuhl, T. Mathes, and P. Hegemann, Journal of Photochemistry and Photobiology B: Biology **86**, 22 (2007).

[74] H. Yuan et al., Biochemistry **45**, 12687 (2006).

[75] Y. Fukushima, K. Okajima, Y. Shibata, M. Ikeuchi, and S. Itoh, Biochemistry **44**, 5149 (2005).

[76] K. Okajima et al., Journal of Molecular Biology **363**, 10 (2006).

[77] A. Kita, K. Okajima, Y. Morimoto, M. Ikeuchi, and K. Miki, Journal of Molecular Biology **349**, 1 (2005).

[78] W. Laan et al., Biochemistry **45**, 51 (2006).

[79] M. Gauden et al., Proceedings of the National Academy of Sciences **103**, 10895 (2006).

[80] M. Gauden et al., Biochemistry **46**, 7405 (2007).

[81] A. L. Stelling, K. L. Ronayne, J. Nappa, P. J. Tonge, and S. R. Meech, Journal of the American Chemical Society **129**, 15556 (2007).

[82] T. Domratcheva, B. L. Grigorenko, I. Schlichting, and A. V. Nemukhin, Biophysical Journal **94**, 3872 (2008).

[83] J. Götze and P. Saalfrank, The Journal of Photochemistry and Photobiology B **94**, 87 (2009).

[84] K. Sadeghian, M. Bocola, and M. Schütz, Journal of the American Chemical Society **130**, 12501 (2008).

[85] K. Sadeghian, M. Bocola, and M. Schütz, Physical Chemistry Chemical Physics **12**, 8840 (2010).

[86] A. Udvarhelyi and T. Domratcheva, Photochemistry and Photobiology , doi:10.1111/j.1751 (2010).

[87] R. Lechner, S. Kümmel, and B. König, Photochemical & Photobiological Sciences **9**, 1367 (2010).

[88] U. Megerle et al., Physical Chemistry Chemical Physics **13**, 8869 (2011).

[89] T. Mathes, C. Vogl, J. Stolz, and P. Hegemann, Journal of Molecular Biology **385**, 1511 (2009).

[90] P. Zirak, A. Penzkofer, T. Mathes, and P. Hegemann, Journal of Photochemistry and Photobiology B **97**, 61 (2009).

[91] P. Zirak, A. Penzkofer, T. Mathes, and P. Hegeman, Chemical Physics **358**, 111 (2009).

[92] R. Ahlrichs, M. Bär, M. Häser, H. Horn, and C. Kölmel, Chemical Physical Letters **162**, 165 (1989).

[93] A. D. Becke, Journal of Chemical Physics **98**, 1372 (1993).

[94] A. Schäfer, H. Horn, and R. Ahlrichs, Journal of Chemical Physics **97**, 2571 (1992).

[95] A. D. Becke, Physical Reviews A **38**, 3098 (1988).

[96] C. Hättig and F. Weigend, Journal of Chemical Physics **113**, 5154 (2000).

[97] C. Hättig and A. Kohn, Journal of Chemical Physics **117**, 6939 (2002).

[98] F. Weigend, M. Häser, H. Patzelt, and R. Ahlrichs, Chemical Physical Letters **294**, 143 (1998).

[99] R. Ahlrichs, Physical Chemistry Chemical Physics **6**, 5119 (2004).

[100] D. E. Woon and T. H. Dunning Jr., Journal of Chemical Physics **98**, 1358 (1993).

[101] N. Foloppe and A. D. MacKerell, Jr., Journal of Computational Chemistry **21**, 86 (2000).

[102] P. Sherwood et al., Journal of Molecular Structure: THEOCHEM **632**, 1 (2003).

[103] W. Smith, C. Yong, and P. Rodger, Molecular Simulation **28**, 385 (2002).

[104] S. R. Billeter, A. J. Turner, and W. Thiel, Physical Chemistry Chemical Physics **2**, 2177 (2000).

[105] J.-P. Ryckaert, G. Ciccotti, and H. J. Berendsen, Journal of Computational Physics **23**, 327 (1977).

[106] T. Yoshihara, S. I. Druzhinin, and K. A. Zachariasse, Journal of the American Chemical Society **126**, 8535 (2004).

[107] Z. R. Grabowski, K. Rotkiewicz, and W. Rettig, Chemical Reviews **103**, 3899 (2003).

[108] T. Merz et al., Physical Chemistry Chemical Physics **15**, 18607 (2013).

[109] S. A. Fleming, Tetrahedron **51**, 12479 (1995).

[110] G. Dorman and G. D. Prestwich, Biochemistry **33**, 5661 (1994).

[111] R. E. Galardy, L. C. Craig, J. D. Jamieson, and M. P. Printz, Journal of Biological Chemistry **249**, 3510 (1974).

[112] M. Fagnoni, D. Dondi, D. Ravelli, and A. Albini, Chemical Reviews **107**, 2725 (2007).

[113] D. Ravelli, D. Dondi, M. Fagnoni, and A. Albini, Chemical Society Reviews **38**, 1999 (2009).

[114] J. Svoboda and B. König, Chemical reviews **106**, 5413 (2006).

[115] P. Wessig, Angewandte Chemie International Edition **45**, 2168 (2006).

[116] C. Müller, A. Bauer, and T. Bach, Angewandet Chemie International Edition **48**, 6640 (2009).

[117] C. Müller et al., Journal of the American Chemical Society **133**, 16689 (2011).

[118] D. F. Kauble, V. Lynch, and M. J. Krische, Journal of Organic Chemistry **68**, 15 (2003).

[119] A. Bauer, F. Westkamper, S. Grimme, and T. Bach, Nature **436**, 1139 (2005).

[120] T. E. Lehmann and A. Berkessel, Journal of Organic Chemistry **62**, 302 (1997).

[121] T. E. Lehmann, G. Müller, and A. Berkessel, Journal of Organic Chemistry **65**, 2508 (2000).

[122] C. Paris, S. Encinas, N. Belmadoui, M. J. Climent, and M. A. Miranda, Organic Letters **10**, 4409 (2008).

[123] K. Musier-Forsyth and P. Schimmel, Biochemistry **33**, 773 (1994).

[124] K. Nakatani, T. Yoshida, and I. Saito, Journal of the American Chemical Society **124**, 2118 (2002).

[125] K. Nakatani and I. Saito, Charge transport in duplex dna containing modified nucleotide bases, in *Longe-Range Charge Transfer in DNA I*, edited by G. Schuster, volume 236 of *Topics in Current Chemistry*, pages 163–186, Springer Berlin / Heidelberg, 2004.

[126] M. Weinberger and H.-A. Wagenknecht, Synthesis **4**, 648 (2012).

[127] S. Grimme and M. Waletzke, Journal of Chemical Physics **111**, 5645 (1999).

[128] T. Schwabe and S. Grimme, Physical Chemistry Chemical Physics **9**, 3397 (2007).

[129] D. Case et al., Amber 11, 2010.

[130] D. Case et al., Amber tools 1.5, 2010.

[131] P. Debye, Mathematische Annalen **67**, 535 (1909).

[132] M. R. Hestenes and E. Stiefel, Journal of Research of the National Bureau of Standards **49** (1952).

[133] B. P. Uberuaga, M. Anghel, and A. F. Voter, The Journal of Chemical Physics **120**, 6363 (2004).

[134] D. J. Sindhikara, S. Kim, A. F. Voter, and A. E. Roitberg, Journal of Chemical Theory and Computation **5**, 1624 (2009).

[135] R. J. Loncharich, B. R. Brooks, and R. W. Pastor, Biopolymers **32**, 523 (1992).

[136] J. Kästner et al., The Journal of Physical Chemistry A **113**, 11856 (2009).

[137] B. Brown, Quarterly Reviews, Chemical Society **5**, 131 (1951).

[138] R. Kluger, Chemical Reviews **87**, 863 (1987).

[139] G. Kachkovskyi, C. Faderl, and O. Reiser, Advanced Synthesis and Catalysis **355**, 2240 (2013).

[140] K. Okada, K. Okamoto, and M. Oda, Journal of the American Chemical Society **110**, 8736 (1988).

[141] K. Okada, K. Okamoto, and M. Oda, Journal of the Chemical Society, Chemical Communications , 1636 (1989).

[142] K. Okada, K. Okamoto, N. Morita, K. Okubo, and M. Oda, Journal of the American Chemical Society **113**, 9401 (1991).

[143] K. Okada, K. Okubo, N. Morita, and M. Oda, Chemistry Letters **22**, 2021 (1993).

[144] F. Weigend and R. Ahlrichs, Physical Chemistry Chemical Physics **7**, 3297 (2005).

A Appendix

A.1 Roseoflavin as photocatalyst?

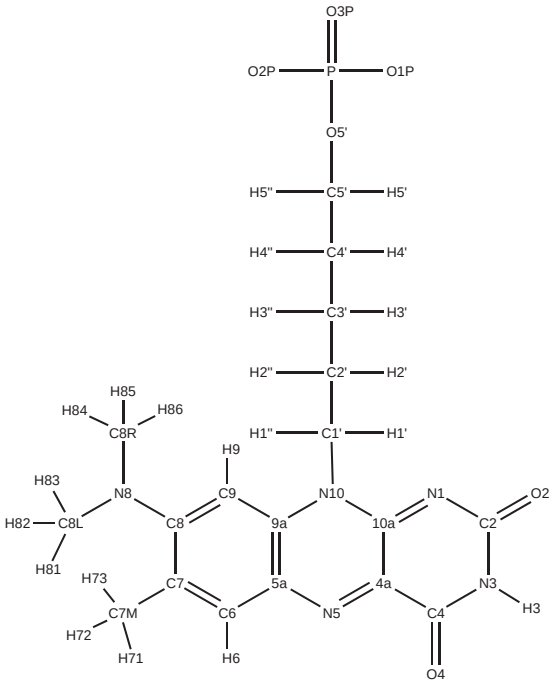

Figure A.1: Atom numbers of roseoflavin (RoF).

Table A.1: Chosen atom types and charges of roseoflavin for CHARMM27 force field; for corresponding atom numbers, see Fig. A.1.

atom	type	charge	atom	type	charge
N1	NN3	-0.660	9a	CN2	0.360
C2	CN1	0.520	N10	NN2	-0.050
O2	ON1	-0.490	10a	CN2	0.310
N3	NN2	-0.460	**ribityl-chain**		
H3	HN2	0.360	C1'	CN8	-0.180
C4	CN1	0.530	H1'	HN8	0.090
O4	ON1	-0.480	H1"	HN8	0.090
4a	CN2	0.360	C2'	CN7	0.140
N5	NN3	-0.660	H2'	HN7	0.090
5a	CN2	0.360	O2'	OH1	-0.660
C6	CN3	-0.115	HO2'	H	0.430
H6	HN3	0.115	C3'	CN7	0.140
C7	CN3	0.000	H3'	HN7	0.090
C7M	CN9	-0.270	O3'	OH1	-0.660
H71	HN9	0.090	HO3'	H	0.430
H72	HN9	0.090	C4'	CN7	0.140
H73	HN9	0.090	H4'	HN7	0.090
C8	CN9	0.050	O4'	OH1	-0.660
N8	NN2	-0.050	HO4'	H	0.430
C8L	CN9	-0.270	C5'	CN8	-0.080
H81	HN9	0.090	H5'	HN8	0.090
H82	HN9	0.090	H5"	HN8	0.090
H83	HN9	0.090	O5'	ON2	-0.620
C8R	CN9	-0.270	**phosphate**		
H84	HN9	0.090	P	P	1.500
H85	HN9	0.090	O1P	ON3	-0.680
H86	HN9	0.090	O2P	ON4	-0.820
C9	CN3	-0.115	O3P	ON3	-0.820
H9	HN3	0.115			

Table A.2: Chosen additional angles of roseoflavin for CHARMM27 force field.

types	force constant k_θ	θ_0
CN7 NN2 HN2	30.0	118.5
NN3 CN1 ON1	130.0	123.8
NN2 CN1 ON1	130.0	121.5
NN2 CN2 NN3	70.0	122.2
CN3 CN3 CN3	40.0	120.0
CN7 CN8 NN2	110.0	111.0
CN7 CN7 OH1	75.7	110.1
CN7 CN7 CN7	53.3	111.0
CN3 CN2 NN2	100.0	125.7
CN7 CN8 ON2	70.0	108.4
HN7 CN7 OH1	45.9	108.8
CN7 OH1 H	57.5	106.0
CN8 CN7 OH1	75.7	110.1
CN2 NN2 CN2	90.0	122.0
CN2 NN2 CN8	70.0	125.9
CN2 NN3 CN2	90.0	119.4
CN2 CN2 CN3	60.0	121.0
CN2 CN1 ON1	50.0	124.7
CN2 CN2 NN2	100.0	116.0
CN2 CN2 NN3	60.0	123.0
CN1 CN2 CN2	70.0	119.6
CN1 NN2 CN1	50.0	125.0
CN1 CN2 NN3	125.0	129.0
CN2 CN1 NN2	70.0	116.0
CN3 CN3 CN9	45.8	122.3
CN3 CN9 NN2	85.0	122.9
CN9 NN2 CN9	70.0	125.9
HN3 CN3 CN9	38.0	122.1
CN9 CN3 CN9	45.8	122.3
CN3 CN9 CN3	40.0	120.0
CN9 CN3 CN2	85.0	117.8

Table A.3: Chosen additional dihedral angles of roseoflavin for CHARMM27 force field.

types	force constant k_ϕ	n	δ
X CN9 CN3 X	0.00	6	0.0
X CN7 CN7 X	0.20	3	0.0
X CN1 CN2 X	12.00	2	180.0
CN7 CN8 ON2 P	2.50	1	180.0
H OH1 CN7 CN8	1.33	1	0.0
X CN7 OH1 X	0.14	3	0.0
X CN2 NN2 X	5.00	2	180.0
X CN2 CN2 X	6.00	2	180.0
X CN8 CN7 X	0.15	3	0.0
CN2 NN2 CN8 HN8	0.40	3	0.0
CN2 NN2 CN8 CN7	0.60	3	0.0
CN9 CN3 CN3 CN2	4.00	2	180.0
NN3 CN2 CN7 CN1	2.00	2	151.7
CN9 NN2 CN9 HN9	0.00	3	0.0
CN3 CN9 NN2 CN9	5.00	2	180.0
CN3 CN3 CN9 NN2	9.00	2	180.0
CN2 CN3 CN9 NN2	9.00	2	180.0

A.2 Benzophenone in dinucleotides as photocatalyst

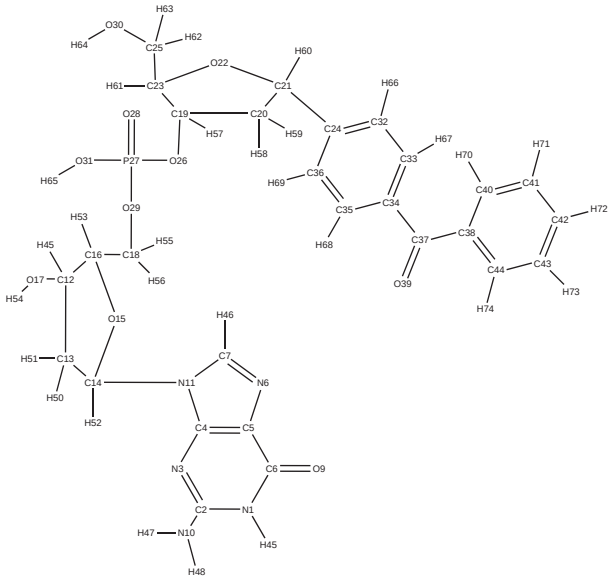

(a) **1G**

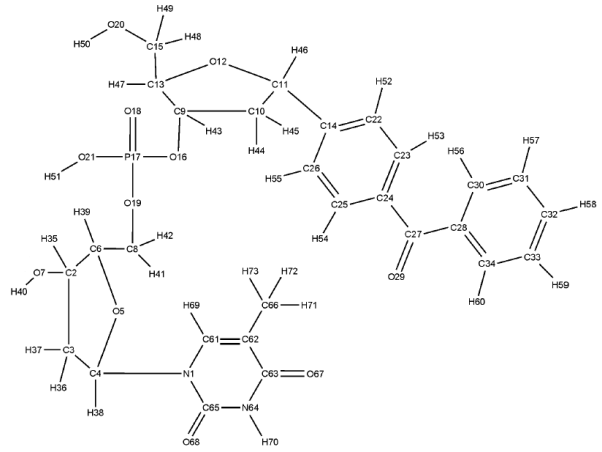

(b) **1T**

Figure A.2: Scheme of **1G** and **1T** dinucleotides and corresponding atom numbers used.

Table A.4: Types and charges for **1G** dinucleotide applied in the AMBER force field; for corresponding atom numbers, see Fig. A.2(a).

atom number	type	charge	atom number	type	charge
N1	NA	-0.666700	C38	ca	-0.008430
C2	CA	0.767410	O39	o	-0.534260
N3	NC	-0.688020	C40	ca	-0.054700
C4	CB	0.300820	C41	ca	-0.209040
C5	CB	0.282460	C42	ca	-0.124470
C6	C	0.528430	C43	ca	-0.166420
C7	CK	0.056260	C44	ca	-0.147130
N8	NB	-0.587410	H45	H	0.417700
O9	O	-0.571560	H46	H5	0.193450
N10	N2	-0.933060	H47	H	0.432150
N11	N*	-0.126000	H48	H	0.411720
C12	CT	0.269570	H49	H1	0.059050
C13	CT	-0.189890	H50	HC	0.098050
C14	CT	0.268530	H51	HC	0.082720
O15	OS	-0.500570	H52	H2	0.119340
C16	CT	0.263830	H53	H1	0.052470
O17	OH	-0.698290	H54	HO	0.402920
C18	CT	-0.128090	H55	H1	0.138760
C19	CT	0.209570	H56	H1	0.180610
C20	CT	-0.503530	H57	H1	0.137590
C21	CT	0.246090	H58	HC	0.166380
O22	OS	-0.533130	H59	HC	0.194410
C23	CT	0.361430	H60	H1	0.103950
C24	ca	-0.010880	H61	H1	0.094870
C25	CT	-0.186370	H62	H1	0.165940
O26	OS	-0.487470	H63	H1	0.097250
P27	P	1.227500	H64	HO	0.454020
O28	O2	-0.670720	H65	HO	0.488570
O29	OS	-0.474240	H66	ha	0.165100
O30	OH	-0.597390	H67	ha	0.109760
O31	OH	-0.700360	H68	ha	0.199300
C32	ca	-0.245970	H69	ha	0.150070
C33	ca	-0.074890	H70	ha	0.092850
C34	ca	0.035560	H71	ha	0.157660
C35	ca	-0.269360	H72	ha	0.156080
C36	ca	-0.059090	H73	ha	0.153900
C37	c	0.485100	H74	ha	0.168070

Table A.5: Types and charges for **1T** dinucleotide applied in the AMBER force field; for corresponding atom numbers, see Fig. A.2(b).

atom number	type	charge	atom number	type	charge
N1	N*	0.002450	H38	H2	0.145830
C2	CT	0.326270	H39	H1	0.111940
C3	CT	-0.338670	H40	HO	0.308050
C4	CT	0.108930	H41	H1	0.133860
O5	OS	-0.385510	H42	H1	0.116920
C6	CT	0.083870	H43	H1	0.125420
O7	OH	-0.662360	H44	HC	0.183280
C8	CT	0.036800	H45	HC	0.188490
C9	CT	0.136080	H46	H1	0.094000
C10	CT	-0.578800	H47	H1	0.055840
C11	CT	0.384290	H48	H1	0.105040
O12	OS	-0.607400	H49	H1	0.069310
C13	CT	0.310120	H50	HO	0.432560
C14	ca	0.051910	H51	HO	0.491330
C15	CT	0.078980	H52	ha	0.169100
O16	OS	-0.203580	H53	ha	0.174770
P17	P	1.138750	H54	ha	0.188690
O18	O2	-0.676280	H55	ha	0.234640
O19	OS	-0.457090	H56	ha	0.149430
O20	OH	-0.700340	H57	ha	0.168190
O21	OH	-0.706290	H58	ha	0.166640
C22	ca	-0.208800	H59	ha	0.175000
C23	ca	-0.127010	H60	ha	0.176290
C24	ca	-0.037850	C61	CM	-0.365710
C25	ca	-0.072930	C62	CM	0.206630
C26	ca	-0.382600	C63	C	0.579150
C27	c	0.359620	N64	NA	-0.599810
C28	ca	0.199670	C65	C	0.624020
O29	o	-0.555830	C66	CT	-0.582060
C30	ca	-0.169250	O67	O	-0.579470
C31	ca	-0.218140	O68	O	-0.608660
C32	ca	-0.118180	H69	H4	0.289330
C33	ca	-0.192340	H70	H	0.408470
C34	ca	-0.190300	H71	HC	0.171900
H35	H1	0.058270	H72	HC	0.174100
H36	HC	0.168230	H73	HC	0.155230
H37	HC	0.107570			

Table A.6: Modifications for parameters applied to AMBER force field;

MASS				
c	12.01	0.616		
ca	12.01	0.360		
ha	1.008	0.135		
o	16.00	0.434		
BOND				
CT-ca	323.5	1.513		
ca-ca	478.4	1.387		
ca-ha	344.3	1.087		
c -ca	349.7	1.487		
c -o	648.0	1.214		
ANGL				
CT-CT-ca	62.5	114.61		
CT-ca-ca	63.8	120.63		
ca-CT-OS	67.7	110.51		
ca-CT-H1	46.8	110.95		
ca-ca-ca	67.2	119.97		
ca-ca-ha	48.5	120.01		
c -ca-ca	64.6	120.14		
ca-c -ca	62.8	119.53		
ca-c -o	68.7	123.44		
O2-P -OH	150.0	108.23		
O2-P -OS	250.0	108.23		
OS-P -OS	250.000	102.46		
HO-OH-P	150.000	110.14		
P-OS-CT	250.000	118.00		
DIHEDRAL				
CT-CT-ca-ca	6	0.000	0.000	2.000
ca-ca-ca-CT	4	14.500	180.000	2.000
CT-ca-ca-ha	4	14.500	180.000	2.000
OS-CT-ca-ca	6	0.000	0.000	2.000
ca-ca-ca-ca	4	14.500	180.000	2.000
ca-ca-ca-ha	4	14.500	180.000	2.000
H1-CT-ca-ca	6	0.000	0.000	2.000
ca-ca-ca-c	4	14.500	180.000	2.000
ca-c -ca-ca	4	14.500	180.000	2.000
o -c -ca-ca	4	14.500	180.000	2.000
c -ca-ca-ha	4	14.500	180.000	2.000
ha-ca-ca-ha	4	14.500	180.000	2.000
IMPROPER				
ca-ca-ca-ha	1.1	180.0	2.0	
c -ca-ca-ca	1.1	180.0	2.0	
ca-ca-c -o	10.5	180.0	2.0	
NONBON				
o	1.6612	0.2100		
ca	1.9080	0.0860		
c	1.9080	0.0860		
ha	1.4590	0.0150		

A.3 Photochemical decarboxylations

A.3.1 IET and protonation

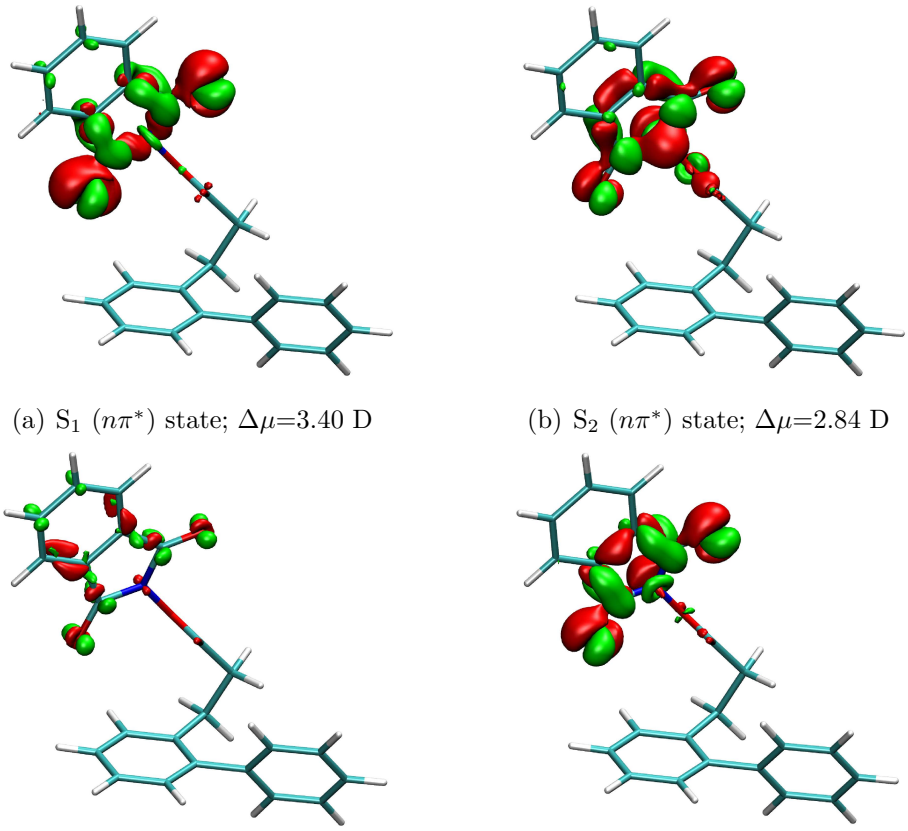

(a) S_1 ($n\pi^*$) state; $\Delta\mu$=3.40 D

(b) S_2 ($n\pi^*$) state; $\Delta\mu$=2.84 D

(c) S_3 ($\pi\pi^*$) state; $\Delta\mu$=1.19 D

(d) S_4 ($n\pi^*$) state; $\Delta\mu$=2.46 D

Figure A.3: Electron density difference plots for the first four excited singlet states of **6a** , calculated with TD-CC2 in def2-SVP basis. Isosurfaces are plotted for ±0.004 a.u., red refers to a decrease, green to an increase in the density upon excitation. Additionally, the types and the dipole moment changes $\Delta\mu$ relative to the GS for the corresponding states are given.

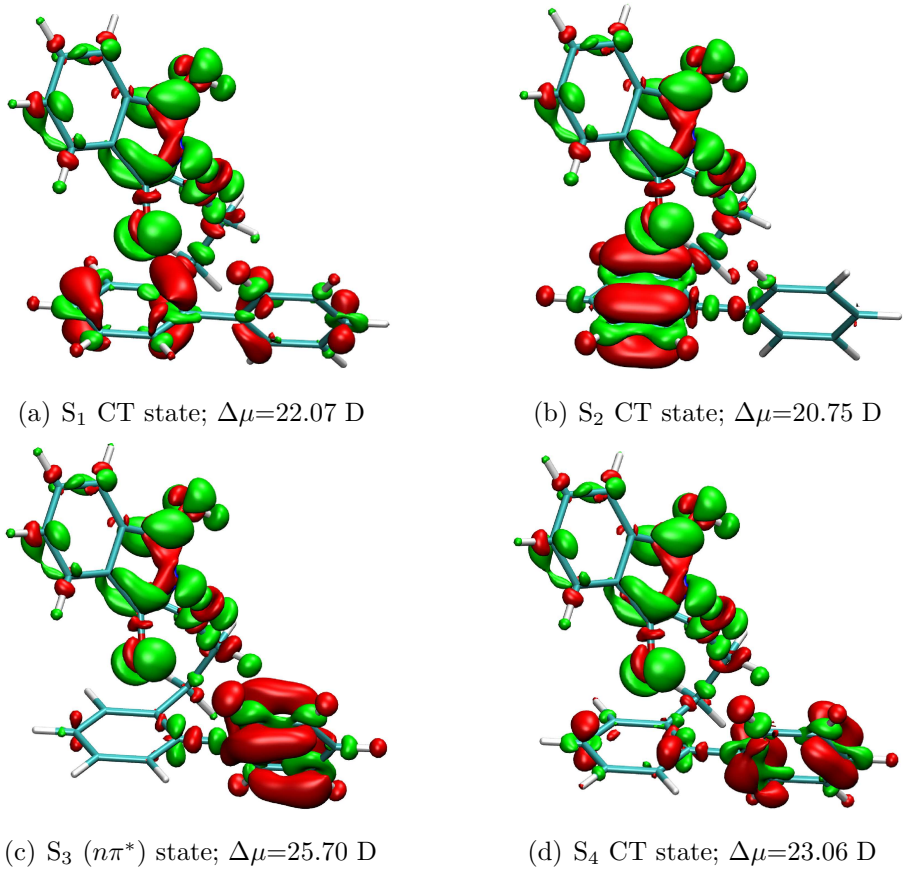

(a) S_1 CT state; $\Delta\mu$=22.07 D

(b) S_2 CT state; $\Delta\mu$=20.75 D

(c) S_3 ($n\pi^*$) state; $\Delta\mu$=25.70 D

(d) S_4 CT state; $\Delta\mu$=23.06 D

Figure A.4: Electron density difference plots for the first four excited singlet states of **6b** , calculated with TD-CC2 in def2-SVP basis. Isosurfaces are plotted for ±0.004 a.u., red refers to a decrease, green to an increase in the density upon excitation. Additionally, the types and the dipole moment changes $\Delta\mu$ relative to the GS for the corresponding states are given.

A.3.2 Modelsystem

As mentioned in the main text, for elucidation of the further steps of the proposed mechanism discussed in Chapter 4 a smaller model system (see also Fig. A.5) was additionally generated, in order to answer also the question of an unexpected by-product observed during the reaction using a similar starting material as **1**. For higher amounts of water, the reaction stops after the *Pht* elimination and an acid is generated (if occurring during this investigation, it is depicted as magenta cycle).

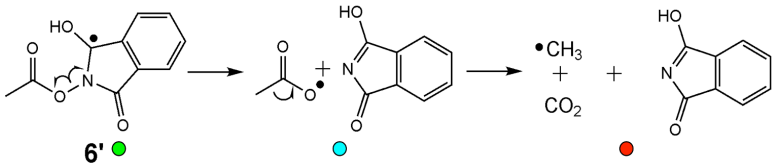

Figure A.5: Model system consisting of protonated *Pht* radical, carboxylic and methyl subgroups; **6'** or green cycle corresponds to the starting geometry, the magenta cycle to the *Pht* elimination and the red cycle to the decarboxylation.

By using U-DFT (B3LYP functional) and the def2-SVP basis set, the ground state PES for the further reaction steps (elimination of *Pht* and subsequent decarboxylation) were calculated for the isolated model system **6'** (plus one possible solvent molecule). Throughout this investigation, all QM calculations were done using the TURBOMOLE program package. The complete molecule of **6b** (Fig. 4.4) was reduced to the smaller model system. This was done to avoid the description of a biradical and get a rough estimate for the subsequent steps of the proposed reaction mechanism. The smaller subsystem **6'** was created by removing *BiP* and one CH_2 unit from the not converged geometry of the singlet state optimisation (last reasonable geometry of S_1 state optimisation with an elongated bond N-O distance, *vide infra*) of **6b**.

As reaction coordinates of interest, the N-O bond distance d(N-O), representing the elimination of the *Pht* unit, and the O-C-O bond angle a(O-C-O), representing the decarboxylation of CO_2, were chosen (see Fig. A.6). To get information about the topology of the PES related to these coordinates, geometry optimisations were done by fixing to certain values of either the a(O-C-O) bond angle (from 120° to

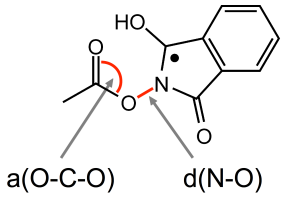

Figure A.6: N-O bond d(N-O) and O-C-O bond angle a(O-C-O) of model system **6'** used for the subsequent calculations.

180° in steps of 10°) , the N-O bond d(N-O) (from 2.6 Bohr to 8.0 Bohr in steps of 0.5 Bohr; note that Bohr was used because of technical reasons) or both by restraints in the subsequent calculations. For the optimisations the DL-FIND optimiser integrated in the ChemShell computational chemistry environment was employed.

In the first step, only the O-C-O bond angle a(O-C-O) was taken into account for the description of both occurring steps in the proposed reaction mechanism, since the instant decarboxylation of the molecule would automatically lead to the elimination of the *Pht* moiety. As one can see from Fig. A.7, this possibility is energetically not favourable. The barrier ΔE, which has to be overcome, amounts to more than 70 kcal/mol, using **6'** as a reference. However, one can also see that after passing this high barrier, the model system relaxes to the expected protonated *Pht*, CO_2 and methyl radical. This can also be seen from the related spin density difference plots shown in Fig. A.7, which correspond for the starting geometry to the *Pht* radical and to the methyl radical at a(O-C-O)=180°. The last geometry of the PES scan along the coordinate a(O-C-O) corresponds to the minimum in the PES, which is 15.4 kcal/mol below the reference structure **6'** at the beginning of the calculations.

Since this high barrier for the instant decarboxylation is hardly to overcome without any consideration of the N-O bond distance d(N-O), for which no modifications can be observed during the optimisations along the O-C-O angle increase, except for the very last step in this PES scan, it is quite probable, that for the desired and energetically favourable reaction the N-O bond also has to be taken into account. Therefore, this N-O bond elongation was investigated in a second step by a PES

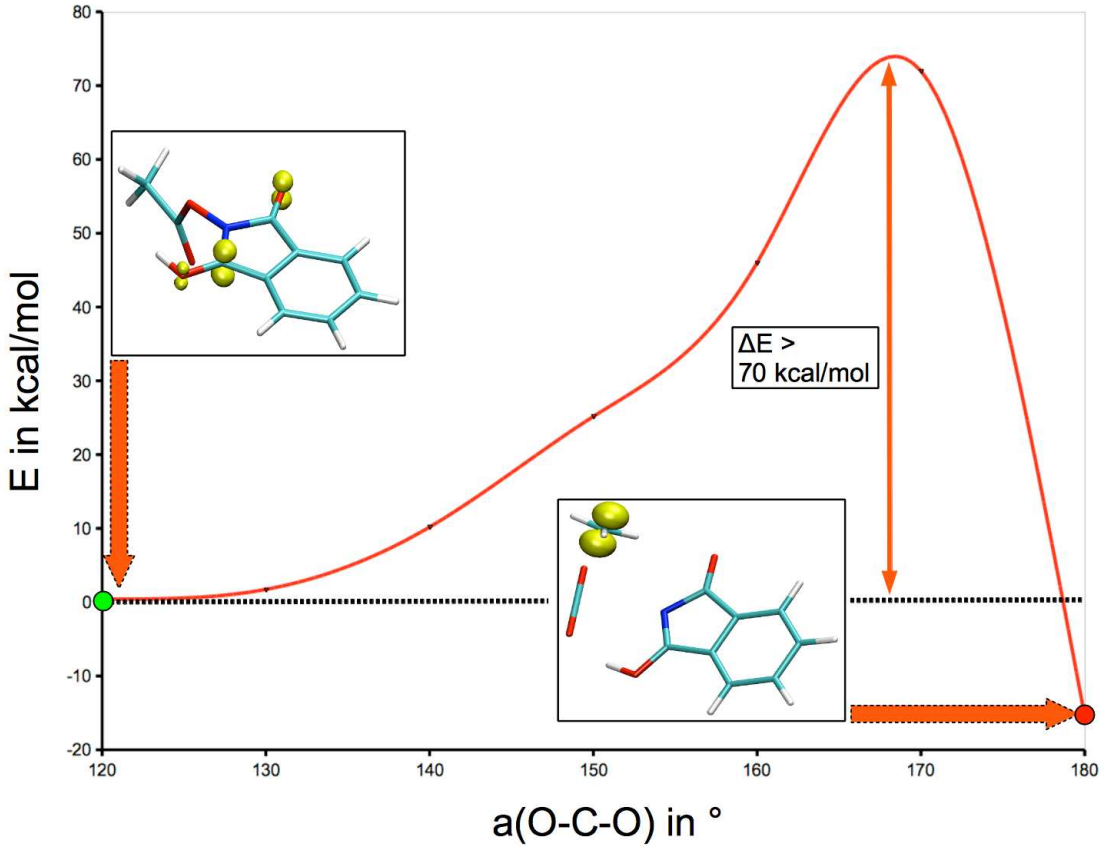

Figure A.7: PES along a(O-C-O) of model system **6'** calculated with U-DFT (B3LYP functional) and def2-SVP basis. The energy refers to the total energy of **6'** at the starting point of the PES. Related spin density differences are also given (isovalue corresponds to 0.03 a.u.).

scan along d(N-O), which is depicted in Fig. A.8.

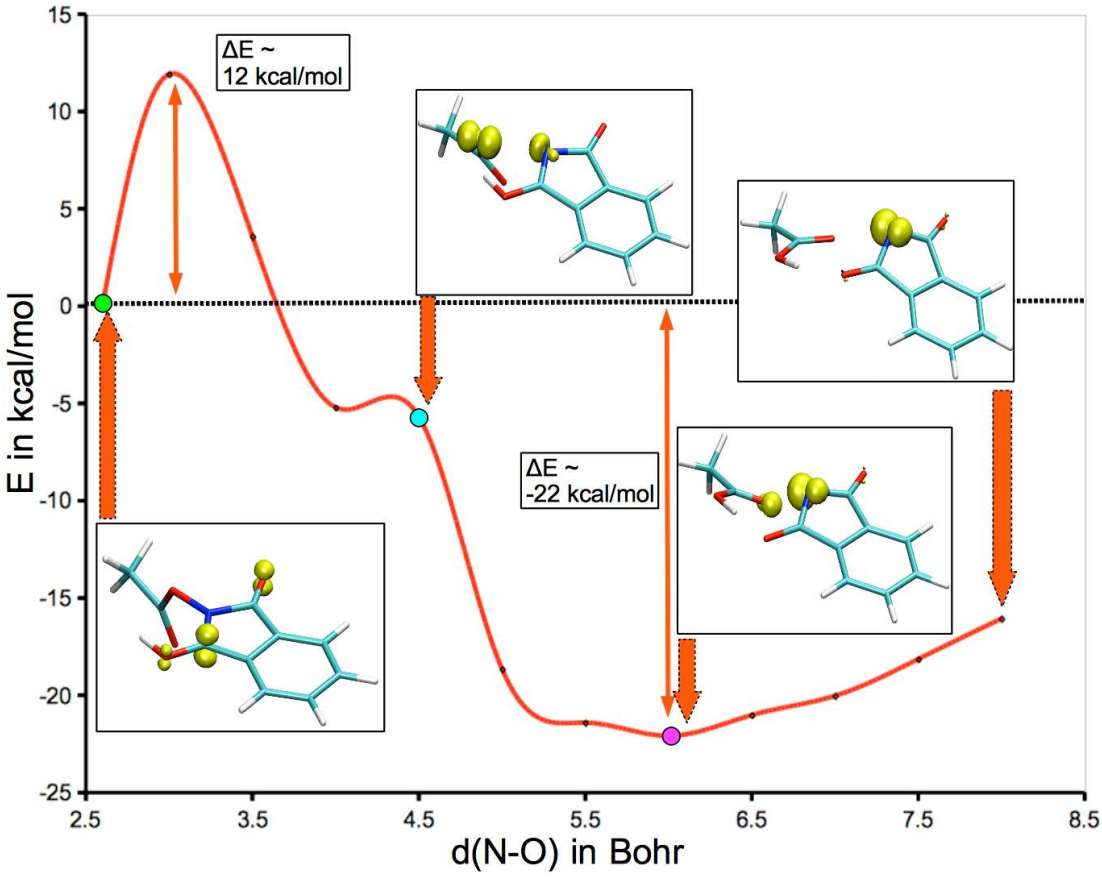

Figure A.8: PES along d(N-O) of model system **6'** calculated with U-DFT (B3LYP functional) and def2-SVP basis. The energy refers to the total energy of **6'** at the beginning of the PES scan. Related spin density differences for different geometries are also given (isovalue corresponds to 0.03 a.u.).

It can be seen, that there is a barrier ΔE of about 12 kcal/mol for the cleavage of the N-O bond. After this barrier, a plateau comes into play, which is due to some reorganisation of the hydroxyl group of the *Pht* with the carboxylic group of the rest of the system. The oxygen of the carboxylic group keeping the radical is moving towards the proton, located at *Pht*. After this plateau, a significant drop in the total energy can be observed which is finally leading to the global minimum for a N-O bond distance of 6.0 Bohr and a structure corresponding to formic acid

(with some spin density on its carboxyl oxygen, as can be seen in Fig. A.8) and a structure corresponding to a neutral *Pht* radical, depicted as magenta cycle in the 1-dim PES. Going further on the PES, the radical is located only on the *Pht*, which seems energetically not favourable. This may be the case due to its artificial appearance for the chosen model system. The minimum at d(N-O)=6.0 Bohr of this PES scan yields an energy gain of 22.1 kcal/mol compared to the starting geometry **6'**. Compared to the minimum of the PES scan along the O-C-O bond angle at a(O-C-O)=180°, which corresponds to an energy gain of 15.4 kcal/mol compared to **6'**, the minimum along d(N-O) corresponds to the energetically more favourable situation (6.7 kcal/mol).

Due to the occurring reorganisation step observed at the plateau described earlier, the geometry at d(N-O)=4.5 Bohr could be a starting point for a decarboxylation possibly taking place competing the acid formation. Hence a PES scan along a(O-C-O) starting from this geometry (depicted as cyan cycle in Fig. A.8) was done, to investigate this possibility. The result of this 1-dim PES scan is shown in Fig. A.9.

Based on the structure at the described plateau at 4.5 Bohr, no barrier for the occurring decarboxylation step can be observed. The minimum of the PES scan features an energy of 12 kcal/mol below the starting point, however, because the energy was referenced to the minimum of the PES scan calculated prior to this, it can easily be seen, that this minimum in the total energy only corresponds to an energetically unfavourable reaction product. It is 4.5 kcal/mol higher in energy, than the acid formation.

Since there are almost no barriers for both channels, formic acid formation and decarboxylation after eliminating the *Pht* moiety, there are two competing possible pathways for the model system investigated with 1-dim PES scans along d(N-O) and a(O-C-O). For the formation of the acid by-product, it seems to be crucial that the proton, attached to the *Pht* moiety, can be transferred to the carboxylic group and that the radical is able to get transferred back to *Pht*. Due to the artificial model system, a very unstable neutral *Pht* radical is formed, which cannot be observed in real nature.

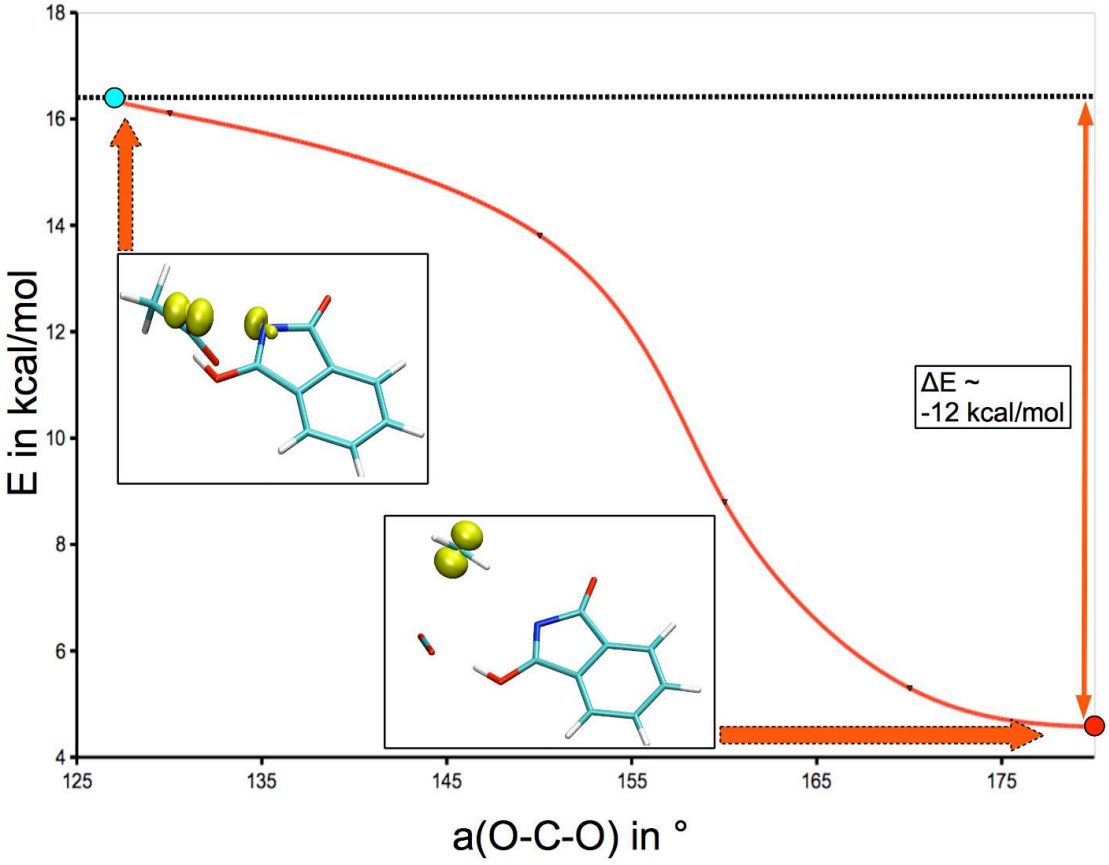

Figure A.9: PES along a(O-C-O) of model system starting from **6'** with d(N-O)=4.5 Bohr taken from the PES scan shown in Fig. A.8 (cyan cycle) calculated with U-DFT (B3LYP functional) and def2-SVP basis. The energy E references to geometry **6'** at d(N-O)=6.0 gained from the PES scan shown in Fig. A.8. Related spin density differences are also given (isovalue corresponds to 0.03 a.u.).

To include the solvent (CH_3CN/H_2O in a ratio of 9/1 or 50/1, respectively was used during the experiment described in Chapter 4) in the model to some extent, one CH_3CN or one water molecule was added at the hydroxyl group of *Pht*, respectively (note, that these solvent molecules would have enough space to fit in the complete system **6b**). Now, 2-dim PES scans for the two coordinates d(NO) and a(O-C-O) were done to see the influence of a protected hydroxyl group; no acid formation should be observed, since the H-transfer from *Pht* to the carboxylic group is not possible. In order to generate starting structures for these PES scans one CH_3CN or H_2O molecule was added artificially to **6'**. The gained geometries were optimised using U-DFT (B3LYP functional) and def2-SVP basis to generate the needed starting structures. The 2-dim PES are depicted in Fig. A.10 for the system containing one CH_3CN molecule and in Fig. A.11 for the system containing one water molecule.

First, the 2-dim PES for the model system and one CH_3CN will be discussed. As well as for the situation without any solvent molecule, one can see an activation barrier for the N-O bond break along d(N-O) coordinate, which is about 12.5 kcal/mol and therefore comparable to the barrier gained without a solvent molecule (ΔE around 12 kcal/mol, see Fig. A.8). The global minimum (shown as red cycle in Fig. A.10) of the gained PES corresponds to the *Pht* elimination followed by the decarboxylation. It is about 16 kcal/mol deeper in energy than the starting geometry (shown as green cycle in Fig. A.10) and therefore comparable to the model without solvent molecule. For the decarboxylation step, starting most probable at the cyan depicted position on the PES a small barrier of 1 kcal/mol has is observed. An acid formation cannot be seen during the PES scan. Evidently, the H-bond between the solvent molecule and the hydroxyl group of *Pht* is strong enough to protect the molecule.

The model system with one water molecule attached to it, on the other hand, shows a quite similar 2-dim PES corresponding to the situation described before. However, the barrier for the N-O bond cleavage is about 6.5 kcal/mol, which is only half of the barriers in all other cases studied so far. Once again, the global minimum (depicted as red cycle in Fig. A.11) corresponds to the decarboxylation

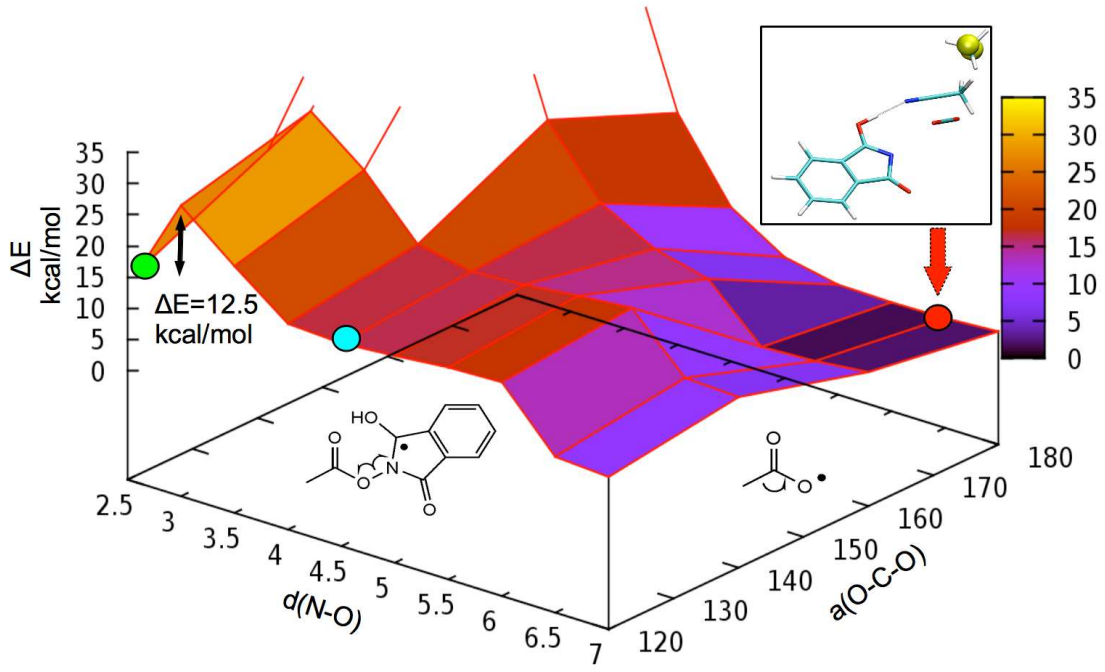

Figure A.10: 2-dim PES along d(N-O), representing *Pht* elimination, and a(O-C-O), representing decarboxylation, of **6'** and one CH_3CN molecule, calculated with U-DFT (B3LYP functional) and def2-SVP basis. The energy E references to the global minimum of PES. Related spin density differences are also given (isovalue corresponds to 0.03 a.u.). The green point corresponds to the optimised starting geometry.

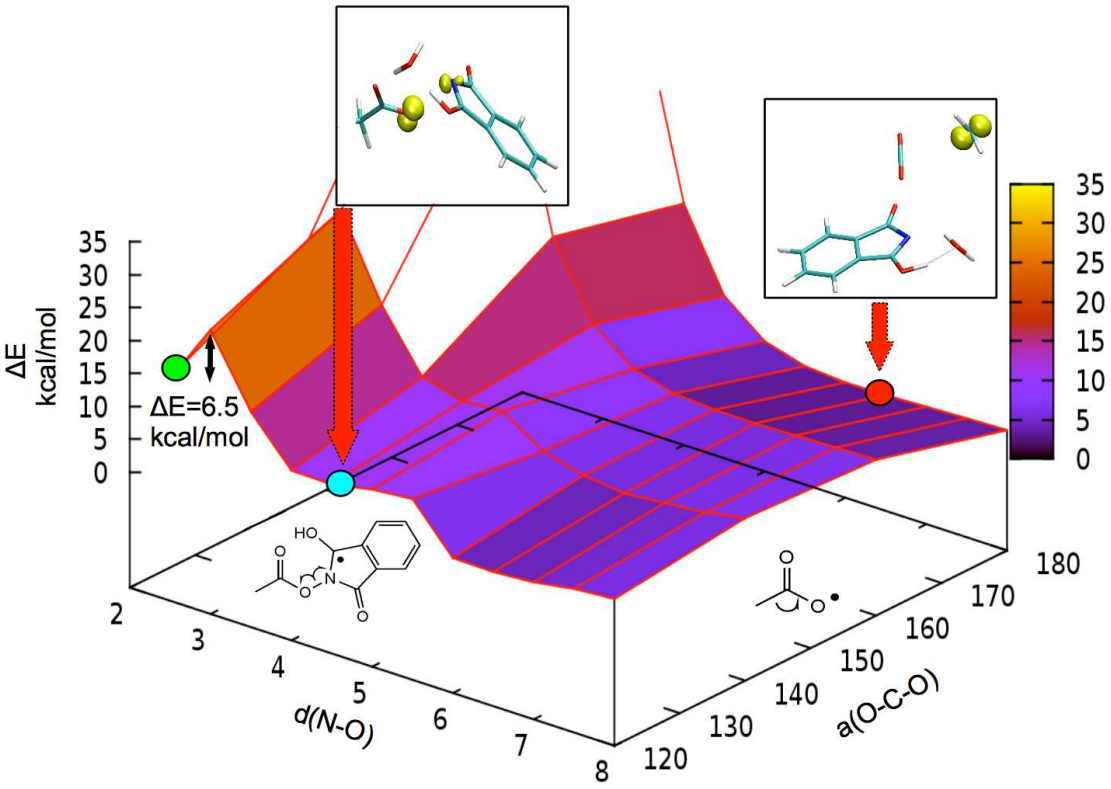

Figure A.11: 2-dim PES along d(N-O), representing *Pht* elimination, and a(O-C-O), representing decarboxylation, of **6'** and one H_2O molecule, calculated with U-DFT (B3LYP functional) and def2-SVP basis. The energy E references to the global minimum (red point) of PES. Related spin density differences are also given (isovalue corresponds to 0.03 a.u.). The green point corresponds to the optimised starting geometry.

after the N-O bond cleavage, which is about 18 kcal/mol deeper in energy than the starting configuration (green cycle). There is also a small barrier for the decarboxylation, starting once again from the cyan depicted point at the PES of about 1 kcal/mol. An acid formation cannot be observed during the optimisation of the PES, either.

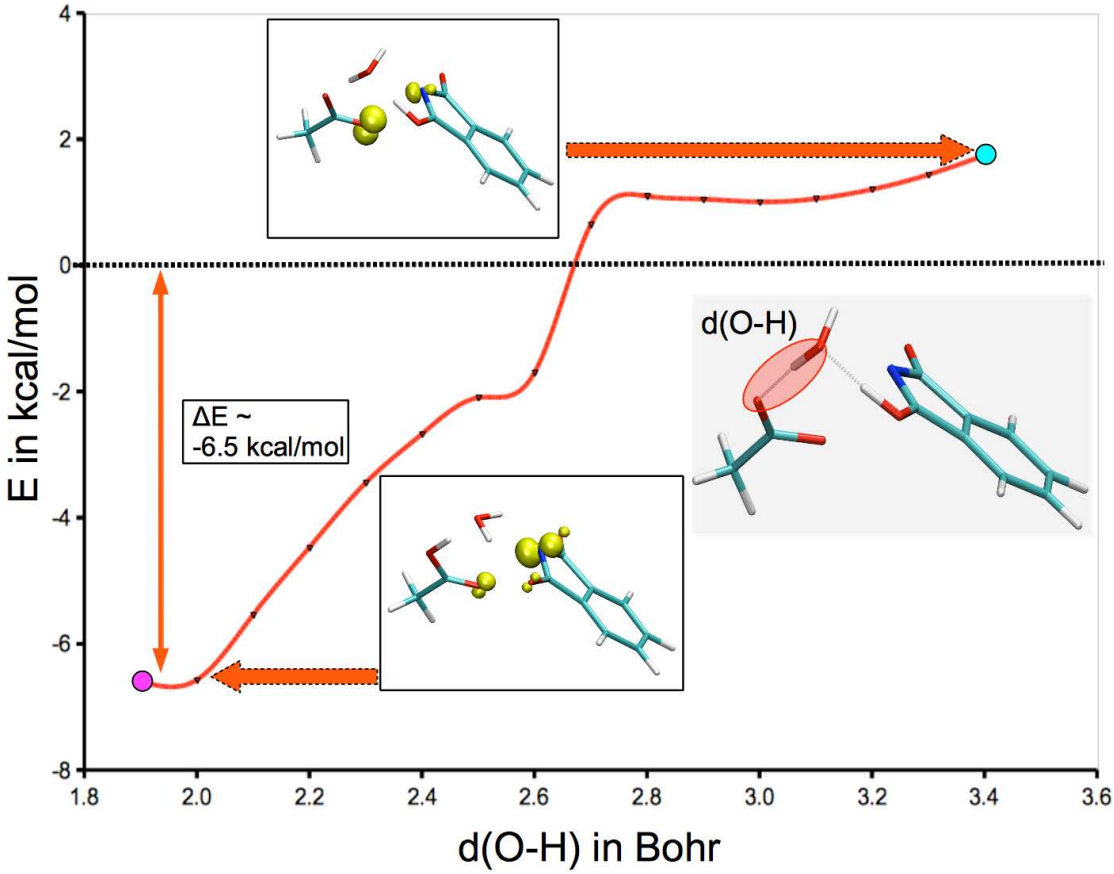

Figure A.12: PES along d(H-O) decrease (for definition see subfigure on the right hand side) of model system **6'** and one H_2O molecule, calculated with U-DFT (B3LYP functional) and def2-SVP basis. The energy E references to the total energy of **6'** and one H_2O molecule at the global minimum of 2-dim PES (red point), depicted in Fig. A.11. Related spin density differences are also given (isovalue corresponds to 0.03 a.u.) for **6'**.

However, due to the fact, that a rearrangement of the H-bonding network of the

existing molecules could occur, a 1-dim PES scan was done, in order to check, if an acid formation could take place by such a reorganisation. The H-bonding network consists of a H-bond of the hydroxyl group of *Pht* to the oxygen of the water and a H-bond from one proton of the water molecule to the carboxylic group of the rest of the system. As a starting geometry, the structure obtained at d(N-O)=6.5 Bohr and a(O-C-O)=120° (cyan cycle in Fig. A.11), was used, since this point corresponds to the comparable starting point of the acid formation seen in the 1-dim PES scan along d(N-O). This was done by decreasing the H-bond d(H-O), which is depicted in Fig. A.12 defined by the distance of the H-bond from the water molecule to the carboxylic group of the model system , in small steps (0.1 Bohr per step). Once again, U-DFT (B3LYP functional) and def2-SVP basis was employed.

As one can see in Fig. A.12, during this reorganisation of the H-bonding network, once again, an acid formation can occur, which is energetically more favourable (6.5 kcal/mol) compared to the decarboxylation minimum. The depicted spin densities are comparable to the model system containing no water molecule.

To sum these preliminary results up, the blocking of the proton of the *Pht* group of the model system with CH_3CN leads to the decarboxylation of the model system after the N-O bond break. The blocking with water keeps the channel for acid formation open, due to the fact, that a reorganisation process in the H-bonding network could take place.